The *NuSTAR* Hard X-Ray Survey of the Norma Arm Region

Francesca M. Fornasini[1,2], John A. Tomsick[2], JaeSub Hong[3], Eric V. Gotthelf[4], Franz Bauer[5,6,7], Farid Rahoui[8], Daniel Stern[9], Arash Bodaghee[10], Jeng-Lun Chiu[2], Maïca Clavel[2], Jesús Corral-Santana[5], Charles J. Hailey[4], Roman A. Krivonos[2,11], Kaya Mori[4], David M. Alexander[12], Didier Barret[13], Steven E. Boggs[2], Finn E. Christensen[14], William W. Craig[2,15], Karl Forster[16], Paolo Giommi[17], Brian W. Grefenstette[16], Fiona A. Harrison[16], Allan Hornstrup[14], Takao Kitaguchi[18], J. E. Koglin[19], Kristin K. Madsen[16], Peter H. Mao[16], Hiromasa Miyasaka[16], Matteo Perri[17,20], Michael J. Pivovaroff[15], Simonetta Puccetti[17,20], Vikram Rana[16], Niels J. Westergaard[14], and William W. Zhang[21]

[1] Astronomy Department, University of California, 601 Campbell Hall, Berkeley, CA 94720, USA; f.fornasini@berkeley.edu
[2] Space Sciences Laboratory, 7 Gauss Way, University of California, Berkeley, CA 94720, USA
[3] Harvard-Smithsonian Center for Astrophysics, 60 Garden Street, Cambridge, MA 02138, USA
[4] Columbia Astrophysics Laboratory, Columbia University, New York, NY 10027, USA
[5] Instituto de Astrofísica and Centro de Astroingeniería, Facultad de Física, Pontificia Universidad Católica de Chile, Casilla 306, Santiago 22, Chile
[6] Millennium Institute of Astrophysics (MAS), Nuncio Monseñor Sótero Sanz 100, Providencia, Santiago, Chile
[7] Space Science Institute, 4750 Walnut Street, Suite 205, Boulder, CO 80301, USA
[8] European Southern Observatory, K. Schwarzschild-Strasse 2, D-85748 Garching bei München, Germany
[9] Jet Propulsion Laboratory, California Institute of Technology, 4800 Oak Grove Drive, Pasadena, CA 91109, USA
[10] Georgia College, 231 W. Hancock Street, Milledgeville, GA 31061, USA
[11] Space Research Institute, Russian Academy of Sciences, Profsoyuznaya 84/32, 117997 Moscow, Russia
[12] Centre for Extragalactic Astronomy, Department of Physics, Durham University, Durham, DH1 3LE, UK
[13] Université de Toulouse; UPS-OMP; IRAP; Toulouse, France & CNRS; Institut de Recherche en Astrophysique et Planétologie; 9 Av. colonel Roche, BP 44346, F-31028 Toulouse cedex 4, France
[14] DTU Space—National Space Institute, Technical University of Denmark, Elektrovej 327, DK-2800 Lyngby, Denmark
[15] Lawrence Livermore National Laboratory, Livermore, CA 94550, USA
[16] Cahill Center for Astrophysics, 1216 E. California Boulevard, California Institute of Technology, Pasadena, CA 91125, USA
[17] ASI Science Data Center (ASDC), via del Politecnico, I-00133 Rome, Italy
[18] Department of Physical Science, Hiroshima University, 1-3-1 Kagamiyama, Higashi-Hiroshima, Hiroshima 739-8526, Japan
[19] Kavli Institute for Particle Astrophysics and Cosmology, SLAC National Accelerator Laboratory, Menlo Park, CA 94025, USA
[20] INAF—Astronomico di Roma, via di Frascati 33, I-00040 Monteporzio, Italy
[21] NASA Goddard Space Flight Center, Greenbelt, MD 20771, USA

Abstract

We present a catalog of hard X-ray sources in a square-degree region surveyed by the *Nuclear Spectroscopic Telescope Array* (*NuSTAR*) in the direction of the Norma spiral arm. This survey has a total exposure time of 1.7 Ms, and the typical and maximum exposure depths are 50 ks and 1 Ms, respectively. In the area of deepest coverage, sensitivity limits of 5×10^{-14} and 4×10^{-14} erg s^{-1} cm^{-2} in the 3–10 and 10–20 keV bands, respectively, are reached. Twenty-eight sources are firmly detected, and 10 are detected with low significance; 8 of the 38 sources are expected to be active galactic nuclei. The three brightest sources were previously identified as a low-mass X-ray binary, high-mass X-ray binary, and pulsar wind nebula. Based on their X-ray properties and multiwavelength counterparts, we identify the likely nature of the other sources as two colliding wind binaries, three pulsar wind nebulae, a black hole binary, and a plurality of cataclysmic variables (CVs). The CV candidates in the Norma region have plasma temperatures of $\approx$10–20 keV, consistent with the Galactic ridge X-ray emission spectrum but lower than the temperatures of CVs near the Galactic center. This temperature difference may indicate that the Norma region has a lower fraction of intermediate polars relative to other types of CVs compared to the Galactic center. The *NuSTAR* log*N*–log*S* distribution in the 10–20 keV band is consistent with the distribution measured by *Chandra* at 2–10 keV if the average source spectrum is assumed to be a thermal model with $kT \approx 15$ keV, as observed for the CV candidates.

Key words: binaries: general – Galaxy: disk – novae, cataclysmic variables – X-rays: binaries – X-rays: stars

1. Introduction

Hard X-ray observations of the Galaxy can be used to identify compact stellar remnants—white dwarfs (WDs), neutron stars(NSs), and black holes (BHs)—and probe stellar evolution in different environments. While a number of sensitive surveys of Galactic regions (e.g., Muno et al. 2009; Townsley et al. 2011; Fornasini et al. 2014) have been performed by the *Chandra X-ray Observatory*, its soft X-ray band (0.5–10 keV) is often insufficient for differentiating between different types of compact objects. The *Nuclear Spectroscopic Telescope Array* (*NuSTAR*; Harrison et al. 2013),

with its unprecedented sensitivity and angular resolution at hard X-ray energies above 10 keV, provides a unique opportunity to study the X-ray populations in the Galaxy. During the first two years of its science mission, *NuSTAR* performed surveys of the Galactic center (GC) and the Norma spiral arm in order to compare the X-ray populations in these regions of the Galaxy, which differ with regard to their star formation history and stellar density. The *NuSTAR* sources found among the old, high-density GC stellar population are described in Hong et al. (2016), and, in this paper, we present the results from the *NuSTAR* Norma arm survey.

In 2011, the Norma Arm Region *Chandra* Survey (NARCS) observed a $2° × 0°.8$ region in the direction of the Norma spiral arm (Fornasini et al. 2014, hereafter F14). The near side of the Norma arm is located at a distance of about 4 kpc, while the far Norma arm is at a distance of 10–11 kpc (Vallée 2008). The Norma region was targeted because its stellar populations are younger than those in the GC but older than those in the young Carina and Orion star-forming regions observed by *Chandra* (F14 and references therein). An additional goal of this survey was to identify low-luminosity high-mass X-ray binaries (HMXBs) falling below the sensitivity limits of previous surveys in order to constrain the faint end of the HMXB luminosity function; the evolutionary state of the Norma arm and the large number of OB associations along this line of sight (Bodaghee et al. 2012) make it an ideal place to search for HMXBs.

About 300 of the 1130 *Chandra* sources detected at $\geqslant 3\sigma$ confidence in the Norma region were found to be spectrally hard in the 0.5–10 keV band, with median energies >3 keV. The majority of these sources are expected to be magnetic cataclysmic variables (CVs) and active galactic nuclei (AGNs), although some could also be HMXBs, low-mass X-ray binaries (LMXBs), or colliding wind binaries (CWBs). Distinguishing between these types of sources is not possible based on *Chandra* data alone, especially since most of the Norma X-ray sources have low photon statistics.

Since *Chandra*'s resolution enables the identification of unique optical/infrared counterparts, spectral identification of the counterparts has helped shed light on the physical nature of some of the Norma X-ray sources (Rahoui et al. 2014). However, not even this information is necessarily sufficient; for example, HMXBs and CWBs both have massive stellar counterparts in the optical/infrared, and it can be difficult to differentiate them spectrally in the *Chandra* band with <100 photon counts, as is the case for most NARCS sources. *NuSTAR* observations, due to their superior sensitivity above 10 keV in the energy range of iron $K\alpha$ and $K\beta$, provide critical information for differentiating hard X-ray sources. For example, CWBs can be distinguished from HMXBs because they have thermal spectra that fall off steeply above 10 keV and strong 6.7 keV Fe emission (Mikles et al. 2006 and references therein), and magnetic CVs can be distinguished from nonmagnetic CVs by their harder spectra, lower equivalent widths of the 6.7 keV line, and higher line ratios of 7.0/6.7 keV Fe emission (e.g., Xu et al. 2016).

The first set of observations of the *NuSTAR* Norma arm survey were carried out in 2013 February and improved the identification of three NARCS sources (Bodaghee et al. 2014, hereafter B14), discovered one transient (Tomsick et al. 2014, hereafter T14), and permitted the study of the disk wind of the LMXB 4U 1630–472 (King et al. 2014). In this paper, we present a catalog of all point sources detected in the *NuSTAR* Norma arm survey. The *NuSTAR* observations and basic data processing are described in Sections 2 and 3. Descriptions of our source detection technique, aperture photometry, and spectral analysis are found in Sections 4, 5, and 5.7, respectively. In Section 6, we discuss the physical nature of the *NuSTAR* detected sources and compare the Norma X-ray populations to those seen in the GC region.

2. Observations

2.1. NuSTAR

NuSTAR observations of the Norma arm region began in 2013 February and were completed in 2015 June. During this period, *NuSTAR* performed 61 observations in the Norma region, shown in Figure 1. Every pointing consists of data from two co-aligned focal plane modules (FPMs), A and B, each of which has a field of view (FOV) of $13' × 13'$.

The *NuSTAR* observations were planned to minimize contamination from stray light and ghost rays. Stray light is the result of zero-bounce photons reaching the detector from bright sources within a few degrees of the FOV, while ghost rays are single-bounce photons from bright sources within about $1°$ of the FOV. The pattern of stray light contamination is well understood and can be carefully predicted,[22] while the patterns of ghost rays are more challenging to model (Koglin et al. 2011; Harrison et al. 2013; Wik et al. 2014; Madsen et al. 2015; Mori et al. 2015).

Therefore, rather than observing the whole region surveyed by *Chandra*, we performed simulations of stray light contamination and focused our observations on three areas of the sky that would be least affected by stray light. Even in these "cleaner" areas, at least one of the FPMs was often affected by stray light, so exposure times for more contaminated observations were lengthened to compensate for the fact that we would not be able to combine data from both modules. Seven additional pointings were specifically made at the locations of some of the brightest NARCS sources found to be hard in the *Chandra* band and for which optical or infrared spectra have been obtained (Rahoui et al. 2014; J. Corral-Santana et al. 2017, in preparation). Unfortunately, despite this adopted strategy, the first mini-survey of the Norma region was highly contaminated by ghost rays because a BH binary in the region, 4U 1630–472, serendipitously went into outburst while the *NuSTAR* observations were taking place (B14). Having learned about the spatial extent of ghost ray contamination, later observations in the proximity of 4U 1630–472 were timed to occur only when it was in quiescence.

Finally, in addition to the observations dedicated to the Norma survey as part of either the baseline *NuSTAR* science program or the *NuSTAR* legacy program, a series of observations were made to regularly monitor the pulsar associated with HESS J1640–465 (Gotthelf et al. 2014, hereafter G14), a very luminous TeV source that resides within the Norma survey area. Combining all such observations taken prior to 2015 March yields a total exposure of 1 Ms over a 100 arcmin² field, which we call the "deep HESS field." While the detailed analysis of the pulsar's braking index is discussed in Archibald et al. (2016), here we present the other *NuSTAR* sources detected in the deep HESS field.

Table 1 lists all the *NuSTAR* observations included in our analysis. Although the sources in the first mini-survey (King et al. 2014; B14; T14), HESS J1640–465 (G14), and IGR J16393–4643 (Bodaghee et al. 2016, hereafter B16) have been analyzed separately and in more detail by others, we include these sources in our analysis in order to measure the photometric properties of all sources in a consistent way, allowing us to calculate the number-flux ($\log N$–$\log S$) distribution of the *NuSTAR* Norma region (NNR) sources.

2.2. Chandra

In this study, we make extensive use of information from the NARCS catalog, as well as the soft (<10 keV) X-ray

---

[22] Stray light constraints for new observations can be checked with the stray light simulation tool at http://www.srl.caltech.edu/NuSTAR_Public/NuSTAROperationSite/CheckConstraint.php.
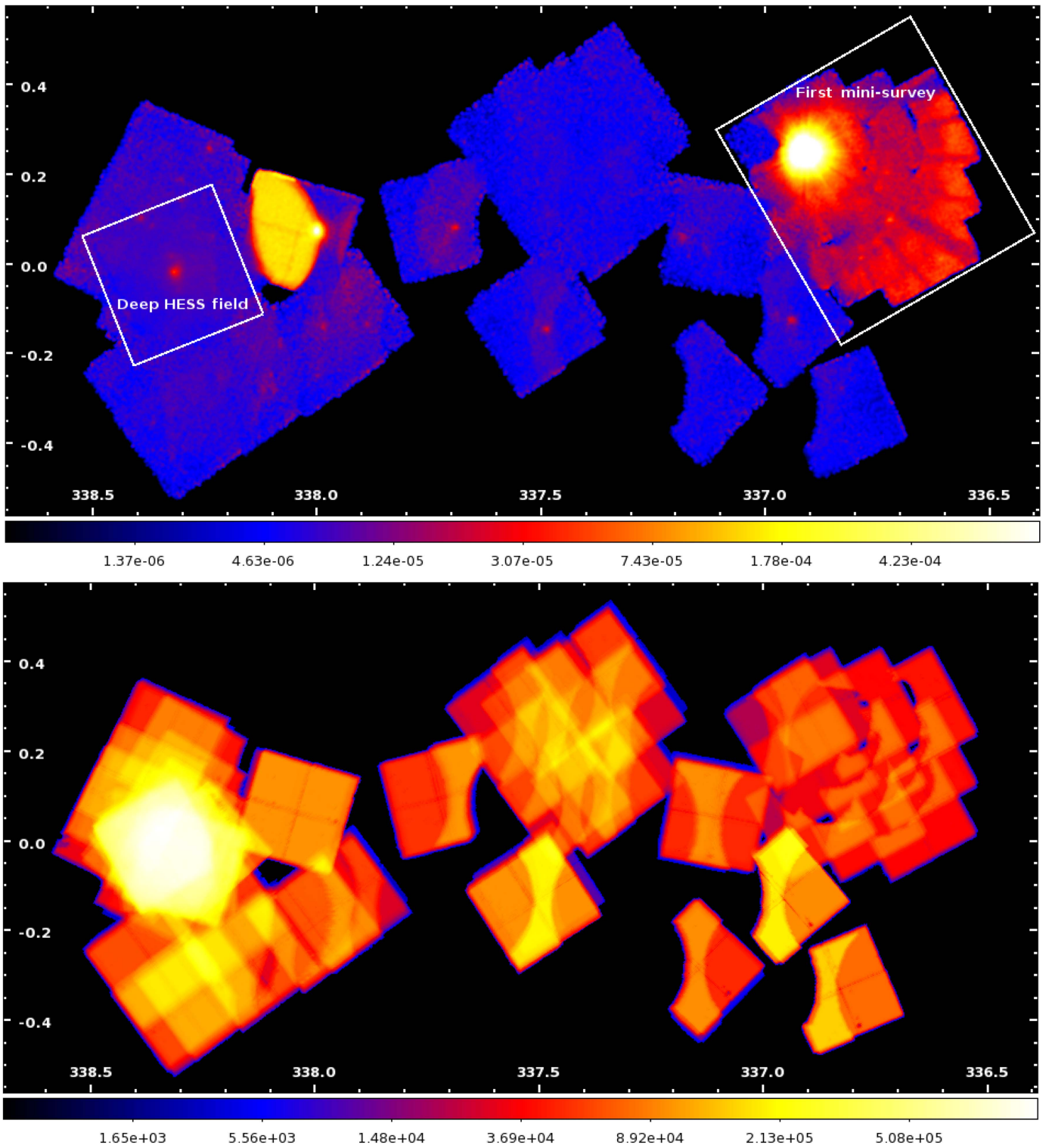
Figure 1. Top panel: smoothed 3–40 keV count rate mosaic (units of counts s^{-1}). Bottom panel: 3–40 keV exposure map without vignetting correction (units of s). The mosaics have been cleaned of most contamination from ghost rays and stray light; some residual ghost ray contamination can be seen in the first mini-survey (top panel, upper right), while one wedge of stray light around $(\ell, b) = (338°, 0°08)$, which is due to GX 340+0, is not removed because a bright source, IGR J16393–4643, is embedded in it.

spectra of some of the NARCS sources. The analysis of these *Chandra* observations and the details of the spectral extraction are provided in F14. We also use two other archival *Chandra* observations that cover part of the area surveyed by *NuSTAR*: ObsID 7591 provides an additional epoch for a transient source (NuSTAR J164116–4632.2,

discussed in Section 5.5), and ObsID 11008 provides spatially resolved observations of NARCS sources 1278 and 1279 (Rahoui et al. 2014), which are blended in the NARCS and *NuSTAR* Norma observations. For reference, we provide information about all of these relevant archival *Chandra* observations in Table 2.

Table 1
NuSTAR Observations of the Norma Arm Region

ObsID (1)	Pointing (J2000)			Start Time (UT) (5)	Exposure (ks) (6)	SL Removal (FPM) (7)	SL Source (8)	Other Contamination (9)
	R.A. (°) (2)	Decl. (°) (3)	PA (°) (4)					
Wide Shallow Survey								
First Mini-Survey								
40014001001	248.4829	−47.7204	160.1494	2013 Feb 24 01:46	18.4	⋯	⋯	Ghost rays from 4Ub in AB
40014002001	248.3623	−47.6444	160.1471	2013 Feb 24 11:31	19.5	⋯	⋯	Ghost rays from 4Ub in AB
40014003001	248.2407	−47.5669	160.1266	2013 Feb 21 20:31	20.8	⋯	⋯	Ghost rays from 4Ub in AB
40014004001	248.5977	−47.6374	160.1231	2013 Feb 22 07:46	19.5	⋯	⋯	Ghost rays from 4Ub in AB
40014005001	248.4775	−47.5622	160.1304	2013 Feb 22 17:31	21.3	⋯	⋯	Ghost rays from 4Ub in AB
40014006001	248.3529	−47.4868	160.1393	2013 Feb 23 04:46	18.9	⋯	⋯	Ghost rays from 4Ub in AB
40014007001	248.7099	−47.5554	160.1350	2013 Feb 23 14:31	22.7	⋯	⋯	Ghost rays from 4Ub in AB
40014008002	248.5845	−47.4826	160.1196	2013 Feb 20 23:31	16.6	⋯	⋯	Ghost rays from 4Ub in AB
40014009001	248.4670	−47.4038	160.1198	2013 Feb 21 10:46	14.7	⋯	⋯	Ghost rays from 4Ub in AB
Later Observations								
40014011002	250.0712	−46.4909	280.7063	2013 Jun 20 00:06	21.5	AB	4Ua	⋯
40014012001	250.0006	−46.4546	280.7266	2013 Jun 20 14:21	19.7	AB	4Ua	⋯
40014013001	249.9200	−46.4004	281.4251	2013 Jun 21 03:16	20.5	A	4Ua	⋯
40014014001	250.2358	−46.3989	285.7049	2013 Jun 21 17:46	16.4	⋯	⋯	1.′5 streak in AB
40014015001	250.0770	−46.3706	285.7091	2013 Jun 22 08:21	19.2	⋯	⋯	⋯
40014016001	250.2620	−46.5441	285.6937	2013 Jun 22 21:21	19.6	AB	4Ua	⋯
40014017001	250.1762	−46.5238	285.6774	2013 Jun 23 11:51	24.2	AB	4Ua	⋯
40014018001	249.9326	−46.3469	286.8740	2013 Jun 24 00:51	23.8	⋯	⋯	⋯
40014019001	250.1520	−46.3873	286.8743	2013 Jun 24 15:21	25.6	⋯	⋯	⋯
40014021002	249.1106	−47.1553	168.0928	2014 Mar 09 21:56	29.1	AB	GX, 4Ua	⋯
40014022001	249.0348	−46.9577	168.0985	2014 Mar 10 15:31	28.4	AB	GX, 4Ua	⋯
40014023001	249.2029	−47.1072	168.1000	2014 Mar 11 07:41	28.8	AB	GX, 4Ua	⋯
40014024001	248.8388	−46.9903	168.1169	2014 Mar 11 23:46	28.1	AB	GX, 4Ua	⋯
40014025001	248.8796	−47.0734	168.1144	2014 Mar 12 17:36	29.1	AB	GX, 4Ua	⋯
40014026001	249.1206	−46.9073	168.0941	2014 Mar 13 11:26	30.2	AB	GX, 4Ua	⋯
40014027001	249.1610	−47.0090	168.1171	2014 Mar 14 03:31	30.2	AB	GX, 4Ua	⋯
40014028002	249.0277	−47.1640	168.1544	2014 Mar 18 12:36	29.6	AB	GX, 4Ua	⋯
40014029001	249.9367	−46.8984	168.2590	2014 Mar 19 04:41	29.2	AB	GX, 4Ua	⋯
40014030001	250.2174	−46.7179	168.3050	2014 Mar 19 20:46	27.3	B	4Ua	⋯
40014031001	250.5222	−46.7773	168.3521	2014 Mar 20 13:01	30.0	B	4Ua	⋯
40014032001	250.4317	−46.7896	168.4181	2014 Mar 21 05:01	30.9	B	4Ua	⋯
40014033002	250.4849	−46.6649	168.2038	2014 Mar 24 10:41	31.5	B	4Ua	⋯
40014034001	250.2701	−46.8265	168.1849	2014 Mar 25 02:46	31.2	AB	GX, 4Ua	⋯
40014035001	250.0454	−46.8714	168.1523	2014 Mar 25 18:56	39.2	AB	GX, 4Ua	⋯
30001008002	249.8301	−46.6567	295.0558	2014 Jun 26 02:21	50.4	⋯	⋯	⋯
30001012002	248.6712	−47.6364	171.9830	2013 Mar 23 08:31	16.3	A	GX	Ghost rays from 4Ub in AB
30001016002	248.5333	−47.3795	164.6452	2014 Mar 06 22:56	21.3	AB	GX, 4Ua	⋯
30001017002	248.8967	−47.3836	210.3881	2014 May 12 21:31	49.0	AB	GX, 4Ua	⋯
30001033002	249.4897	−46.9015	145.8254	2015 Jan 28 05:16	51.8	AB	GX, 4Ua	⋯
30160001002	249.3137	−47.5723	267.7851	2015 Jun 11 14:46	49.4	AB	GX, 4Ua	⋯
30160002002	248.9436	−47.5918	261.9558	2015 Jun 07 23:46	97.1	AB	GX, 4Ua	⋯
30160003002	249.0412	−47.8404	244.4634	2015 May 31 11:11	76.7	AB	GX, 4Ua	⋯
40001022002	249.5341	−47.2183	164.5577	2014 Mar 07 11:51	100.6	AB	GX, 4Ua	⋯
Deep HESS Field								
30002021002	250.1049	−46.5763	353.7407	2013 Sep 29 06:56	62.8	AB	GX, 4Ua	SL of unknown origin in A
30002021003	250.1324	−46.5412	353.7551	2013 Sep 30 16:31	20.8	A	4Ua	SL of unknown origin in A
30002021005	250.2036	−46.5095	161.2653	2014 Feb 28 23:16	99.5	AB	4Ua	⋯
30002021007	250.2027	−46.5145	161.2702	2014 Mar 06 01:51	35.9	AB	4Ua	⋯
30002021009	250.2175	−46.5088	166.7254	2014 Mar 14 21:21	32.5	AB	4Ua	⋯
30002021011	250.2296	−46.5012	179.7925	2014 Apr 11 13:11	22.5	AB	4Ua	⋯
30002021013	250.1923	−46.5268	227.3736	2014 May 25 01:56	21.6	⋯	⋯	⋯
30002021015	250.1802	−46.5601	289.9801	2014 Jun 23 12:51	29.2	A	4Ua	⋯
30002021017	250.1814	−46.5644	295.1336	2014 Jun 25 13:31	22.0	⋯	⋯	⋯
30002021019	250.1913	−46.5447	295.1661	2014 Jun 27 05:41	19.5	⋯	⋯	⋯
30002021021	250.1762	−46.5687	295.1179	2014 Jun 30 01:41	19.8	⋯	⋯	⋯
30002021023	250.1892	−46.5586	311.5738	2014 Jul 11 02:21	22.1	⋯	⋯	⋯
30002021025	250.1569	−46.5398	330.9082	2014 Aug 10 05:36	21.9	A	IGR, 4Ua	6′ streak in B
30002021027	250.1477	−46.5524	344.3607	2014 Sep 11 10:56	20.0	AB	GX, 4Ua	⋯
30002021029	250.1247	−46.5392	356.5397	2014 Oct 11 01:01	22.1	AB	4Ua	⋯

Table 1
(Continued)

| ObsID | Pointing (J2000) | | | Start Time | Exposure | SL Removal | SL | Other |
| | R.A. (°) | Decl. (°) | PA (°) | (UT) | (ks) | (FPM) | Source | Contamination |
(1)	(2)	(3)	(4)	(5)	(6)	(7)	(8)	(9)
30002021031	250.1400	−46.5260	15.7729	2014 Nov 05 07:56	4.3	AB	4Ua	⋯
30002021033	250.2058	−46.4950	129.7677	2015 Jan 08 04:46	4.2	⋯	⋯	⋯
30002021034	250.2115	−46.4858	129.7237	2015 Jan 12 18:16	16.7	⋯	⋯	⋯
30002031036	250.2188	−46.5018	154.4146	2015 Feb 14 18:26	31.8	AB	4Ua, 4Ub	⋯

Notes. (4) Position angle (east of north). (7) FPMs from which stray light background photons from sources in column 8 were removed. (8) Stray light background sources: GX = GX 340+0, 4Ua = 4U 1624−49, 4Ub = 1630−472, IGR = IGR J16318−4848. Although additional stray light from IGR J16320−4751 was present in some of the first mini-survey observations and stray light from 4U 1624−49 and GX 340+0 was present in observation 30001008002, this stray light background was not removed because real sources could be seen in the raw data residing in the stray light–contaminated regions. The contamination in observations 30002021002A, 30002021003A, 30002021036B, and 30001012002 was so extensive that these observations were not included in our analysis.

Table 2
Archival *Chandra* Observations Used in This Study

| *Chandra* ObsID | Pointing (J2000) | | Start Time | Exposure | References |
| | R.A. (°) | Decl. (°) | (UT) | (ks) | |
(1)	(2)	(3)	(4)	(5)	(6)
7591	250.187126	−46.520108	2007 May 11 11:01	28.8	Lemiere et al. (2009)
11008	250.134287	−46.393394	2010 Jun 19 22:10	39.6	Rahoui et al. (2014)
Norma Arm Region Chandra Survey (NARCS)					Fornasini et al. (2014)
12507	250.373201	−46.662951	2011 Jun 06 10:15	18.8	"…"
12508	250.155011	−46.530604	2011 Jun 06 15:57	18.5	"…"
12509	249.937805	−46.397816	2011 Jun 06 21:22	19.4	"…"
12510	250.180190	−46.812896	2011 Jun 09 12:29	19.9	"…"
12511	249.961646	−46.681456	2011 Jun 17 11:15	19.3	"…"
12512	249.743370	−46.550407	2011 Jun 27 04:52	20.5	"…"
12513	249.984947	−46.965904	2011 Jun 27 11:00	20.2	"…"
12514	249.767582	−46.829470	2011 Jun 10 16:07	19.8	"…"
12515	249.550110	−46.695978	2011 Jun 10 22:04	19.5	"…"
12516	249.790838	−47.111874	2011 Jun 11 03:46	19.5	"…"
12517	249.572205	−46.978413	2011 Jun 11 09:28	19.5	"…"
12518	249.354673	−46.844540	2011 Jun 11 15:10	19.5	"…"
12519	249.594334	−47.262081	2011 Jun 13 04:25	19.3	"…"
12520	249.375577	−47.128273	2011 Jun 13 10:13	19.0	"…"
12521	249.157932	−46.994022	2011 Jun 13 15:46	19.0	"…"
12522	249.396933	−47.410725	2011 Jun 13 21:20	19.0	"…"
12523	249.178061	−47.276529	2011 Jun 14 02:53	19.0	"…"
12524	248.960334	−47.141940	2011 Jun 14 08:27	19.5	"…"
12525	249.198427	−47.559064	2011 Jun 14 14:08	19.5	"…"
12526	248.979417	−47.424468	2011 Jun 14 19:50	19.0	"…"
12527	248.761625	−47.289491	2011 Jun 15 19:36	19.3	"…"
12528	248.998831	−47.707016	2011 Jun 16 01:24	19.0	"…"
12529	248.779750	−47.572056	2011 Jun 16 06:58	19.0	"…"
12530	248.561776	−47.436667	2011 Jun 16 12:31	19.3	"…"
12531	248.798050	−47.854617	2011 Jun 16 18:09	19.5	"…"
12532	248.578823	−47.719259	2011 Jun 16 23:51	19.5	"…"
12533	248.360823	−47.583518	2011 Jun 17 05:32	19.5	

Note. (6) References in which archival observations were previously presented and analyzed.

Furthermore, in this study, we make use of *Chandra* observations that were triggered to follow up four transient sources discovered by *NuSTAR*. These *Chandra* observations were used to constrain their soft X-ray spectra and better localize their positions so as to be able to search for optical and infrared counterparts. The follow-up observations of one of these transients, NuSTAR J163433−4738.7, are discussed in T14, and the others are presented in Section 5.5 and listed in Table 3.

3. *NuSTAR* Data Processing and Mosaicking

The raw data of each observation were processed using CALDB v20150612 and the standard *NuSTAR* pipeline v1.3.1 provided under HEASOFT v6.15.1 to produce event files and exposure maps for both FPMs. We made exposure maps with and without vignetting corrections to be used in different parts of our analysis.

Table 3
Chandra Follow-up Observations of *NuSTAR* Transients

Chandra ObsID (1)	Source No. (2)	Pointing (J2000)		Start Time (UT) (5)	Exposure (ks) (6)	Delay between *NuSTAR* & *Chandra* Observations (days) (7)
		R.A. (°) (3)	Decl. (°) (4)			
16170	19	250.315079	−46.540562	2014 Mar 17 05:44	4.9	3
16171	20	250.591644	−46.716049	2014 Oct 20 06:31	4.9	210
17242	25	248.999542	−47.807671	2015 Jul 04 10:26	9.8	34

Notes. (2) NNR source that triggered the *Chandra* observation. (7) Time elapsed between the *NuSTAR* observation in which the source is detected and the *Chandra* follow-up observation. These times vary significantly because some of these sources were obvious in the raw images, while others required mosaicking and careful photometric analysis to determine that they were significant detections.

Next, we cleaned the event files of stray light contamination by filtering out X-ray events in stray light–affected regions. Table 1 indicates whether stray light removal occurred in either FPMA or FPMB, as well as the source responsible for the stray light. In one exceptional case, we did not remove the stray light seen in the FPMA and FPMB of observation 30001008002, since a bright source, IGR J16393–4643, is located within the stray light regions caused by GX 340+0 and 4U 1624–49. We also excised the most significant ghost rays from observations from the first mini-survey, defining the ghost ray pattern regions in the same way as B14. One observation, 30001012002, was performed to follow up NuSTAR J163433–4738.7, a transient source discovered in the first mini-survey. This observation helped to characterize the outburst duration of this transient (T14), but it was so extensively contaminated by ghost rays that it was not included in our analysis. Finally, a few observations show additional contamination features, such as sharp streaks (listed in Table 1), which were also removed.

To improve the astrometric accuracy of the *NuSTAR* observations, we calculated the shifts between the positions of bright *NuSTAR* sources and their *Chandra* counterparts in NARCS observations that were astrometrically registered using infrared counterparts in the VISTA Variables in the Via Lactea (VVV; Minniti et al. 2010) survey (Fornasini et al. 2014). The positions of bright sources, which could be easily identified in raw images, were determined using the IDL gcntrd tool, which makes use of the DAOPHOT "FIND" centroid algorithm. This source localization was done independently for each FPM of each observation and was used to apply translational shifts to event files and exposure maps. In performing astrometric corrections, we limited ourselves to using sources with >100 net counts in each individual observation and FPM and located on-axis. For on-axis sources with this number of counts, we expect the statistical error on the centroid to be <6″ based on simulations (B. Grefenstette 2014, personal communication). NARCS 999 is very bright, with > 10,000 net counts, and therefore the statistical uncertainties of the astrometric corrections derived from this source are <2″ at 90% confidence. The other sources used for astrometric corrections have 100–300 net counts, and their associated statistical uncertainties are expected to be 5–6″ at 90% confidence. Table 4 lists the applied boresight shifts and the bright sources used for astrometric correction. We were only able to apply these astrometric corrections to 23 out of 60 observations (43 out of 117 modules) due to the dearth of bright X-ray sources in our survey. Our inability to astrometrically correct all the observations does not significantly impact the results of our photometric and spectral analysis, since the radii of the source regions we use are significantly larger than the expected shifts. The boresight shifts range from 1″ to 14″; 20% of the shifts are larger than 8″, which is more than expected based on *NuSTAR*'s nominal accuracy of ±8″ at 90% confidence (Harrison et al. 2013) but is not unexpected given that the statistical errors on the source positions may be as high as 6″. Checking each shifted and unshifted image by eye and comparing the locations of *NuSTAR* sources with their *Chandra* counterparts in shifted and unshifted mosaic images, we confirm that these boresight shifts constitute an improvement over the original *NuSTAR* positions.

We reprojected the event files of each observation onto a common tangent point and merged all the observations and both FPMs together to maximize the photon statistics. We then generated mosaic images on the common sky grid in the 3–78, 3–10, 3–40, 10–20, 10–40, 20–40, and 40–78 keV bands. To create mosaic exposure maps, we combined the individual exposure maps by adding exposure values at the location of each sky pixel in the mosaic image; we made exposure maps both without vignetting corrections and with vignetting corrections evaluated at 8, 10, and 20 keV. We used the exposure maps without vignetting corrections when we calculated the source significance and net counts, since these calculations require comparing the exposure depth in the source and background region apertures and the background is dominated by nonfocused emission. Instead, when calculating sensitivity curves (Section 6.2), we used exposure maps with vignetting corrections, since the source emission is focused by the telescope mirrors. When calculating the source fluxes, vignetting corrections are taken into account through the ancillary response file (ARF). An exposure-corrected *NuSTAR* mosaic image in the 3–40 keV band and exposure map without vignetting correction are shown in Figure 1. As can be seen, the typical exposure depth of the Norma survey is 30–100 ks, while the exposure of the deep field is 1 Ms.

4. Source Detection

4.1. Generating Trial Maps

To identify sources in the *NuSTAR* Norma survey, we employed a technique that was specifically developed for the *NuSTAR* surveys. This technique, which we refer to as the "trial map" technique, is described in detail by Hong et al. (2016), so we only provide a brief explanation here. The *NuSTAR* GC region survey (Hong et al. 2016) and the *NuSTAR* extragalactic surveys (Civano et al. 2015; Mullaney et al. 2015) all use this technique as the basis for their detection method. As a result of

Table 4
Boresight Corrections

ObsID (1)	Total shift (″) (2)	R.A. Shift (″) (3)	Decl. Shift (″) (4)	Reference Source (NARCS ID) (5)
30001008002A	5.5	−6.5	3.25	999
30001008002B	6.9	−0.1	6.7	999
30001033002A	5.6	−1.9	−5.4	750
30001033002B	3.2	−2.1	−2.8	750
30002021002B	4.2	6.0	0.0	1321
30002021003B	10.8	13.7	−5.2	1321
30002021005A	4.5	5.0	−2.9	1321
30002021005B	3.7	−5.3	0.5	1321
30002021007A	4.2	3.1	−3.6	1321
30002021007B	3.7	−5.4	−0.8	1321
30002021009A	1.7	−0.3	−1.7	1321
30002021009B	4.4	−6.1	1.2	1321
30002021011A	4.3	−4.4	3.1	1321
30002021011B	4.7	−6.9	0.3	1321
30002021013A	7.9	8.2	5.5	1321
30002021013B	6.1	1.8	6.0	1321
30002021015A	4.5	3.7	3.7	1321
30002021015B	6.0	0.6	5.9	1321
30002021017A	2.2	2.1	1.6	1321
30002021017B	2.9	4.1	0.6	1321
30002021019A	7.1	10.0	−1.6	1321
30002021019B	10.0	11.2	6.4	1321
30002021021A	1.8	−0.6	−1.8	1321
30002021021B	7.2	9.4	3.2	1321
30002021023A	1.2	1.8	0.1	1321
30002021023B	7.9	−6.2	−6.6	1321
30002021025A	7.7	11.2	0.0	1321
30002021025B	9.3	13.3	1.0	1321
30002021027A	0.6	0.9	0.1	1321
30002021027B	8.7	11.7	−3.2	1321
30002021029A	10.2	12.1	−5.9	1321
30002021029B	5.9	5.9	−4.3	1321
30002021031A	9.3	10.9	5.5	1321
30002021031B	7.2	0.8	7.2	1321
30002021033A	7.2	1.3	−7.1	1321
30002021033B	14.4	−20.6	−2.6	1321
30002021034A	10.5	−8.7	−8.7	1321
30002021034B	9.8	10.8	6.3	1321
30002021036A	5.7	−8.4	−0.1	1321
40001022002A	4.9	−5.9	−2.9	786
40001022002B	6.4	−9.5	0.3	786
40014017001A	9.0	6.9	−7.7	1321
40014017001B	7.7	6.6	6.2	1321

Notes. The 90% confidence statistical uncertainties of the astrometric corrections are estimated to be $<2''$ for NARCS 999 and 5–6″ for all other NARCS sources. (2) Angular distance between original pointing and boresight-corrected pointing. (5) NARCS ID of source used to determine astrometric correction.

NuSTAR's point-spread function (PSF) being larger and its background being higher and more complex compared to other focusing X-ray telescopes, such as *Chandra* and *XMM-Newton*, the utility of typical detection algorithms, such as `wavdetect` (Freeman et al. 2002), is limited when applied to *NuSTAR* data. One way of dealing with this problem is to add an additional level of screening to the results of conventional algorithms, calculating the significance of detections by independent means and setting a significance detection threshold. The trial map

technique is more direct, skipping over the initial step of using a detection algorithm such as `wavdetect`.

To make a trial map, for each sky pixel, we calculate the probability of acquiring more than the total observed counts within a source region due to a random background fluctuation. For each pixel, the source and background regions are defined as a circle and an annulus, respectively, centered on that pixel. The mean background counts expected within the source region are estimated from the counts in the background region scaled by the ratio of the areas and exposure values of the source and background regions. Using background regions that are symmetric around the central pixel helps to account for spatial variations of the background. In making trial maps, we plot the inverse of the random chance probability, which is the number of random trials required to produce the observed counts simply by random background fluctuations, such that brighter sources with higher significance have higher values in the maps.

We generated trial maps using three different source region sizes with radii of $9''.5$, $12''$, and $17''$ (corresponding to 15%, 22%, and 30% enclosures of the PSF, respectively) and six different energy bands (3–78, 3–10, 10–40, 40–78, 10–20, and 20–40 keV). The source region sizes we used are slightly larger than those used in the analysis of the *NuSTAR* GC survey, since the smaller sizes are especially suited for picking out relatively bright sources in areas of diffuse emission, but in the Norma region there is no evident diffuse emission apart from stray light and ghost rays. The inner and outer radii of the background regions are $51''$ (corresponding to 70% of the PSF) and $85''$ (equal to 5/3 of the inner radius), respectively, in all cases. Figure 2 shows trial maps made using the 22% PSF enclosure and the 3–10, 10–20, and 20–40 keV bands; the three energy bands are combined into a three-color image so that spectral differences between sources can be seen.

4.2. Detection Thresholds and Source Selection

When considering how to set detection thresholds for our trial maps, we excluded the observations from the first mini-survey and observation 30001008002, since they have significantly higher levels of stray light and ghost ray contamination than the rest of the survey; in the remainder of this paper, we will refer to this subset of observations as the "clean" sample. Figure 3 shows the fractional distributions of the values from the clean trial maps using source region sizes of 22% PSF enclosures. As can be seen, the distribution for the 40–78 keV band is very close to that expected for a Poissonian distribution of random background fluctuations, and, in fact, no sources are clearly visible in the 40–78 keV clean trial maps.

Following the procedure described in Hong et al. (2016) to establish detection thresholds, we began by cross-correlating each trial map with the NARCS source catalog. Figure 4 shows the maximum trial map value within $10''$ of the locations of the NARCS sources detected at $>3\sigma$ in the 2–10 keV band as a function of *Chandra* photon flux. Above *Chandra* fluxes of 6×10^{-6} cm^{-2} s^{-1}, more than 1/3 of the NARCS sources have trial map values that are significantly higher than the bulk of the NARCS sources clustered between trial map values of $10^{0.3}$ and 10^3. For *Chandra* fluxes lower than 2×10^{-6} cm^{-2} s^{-1}, the distribution of trial map values is uncorrelated with source flux, having a linear Pearson correlation coefficient $|p| < 0.04$ for all trial maps.
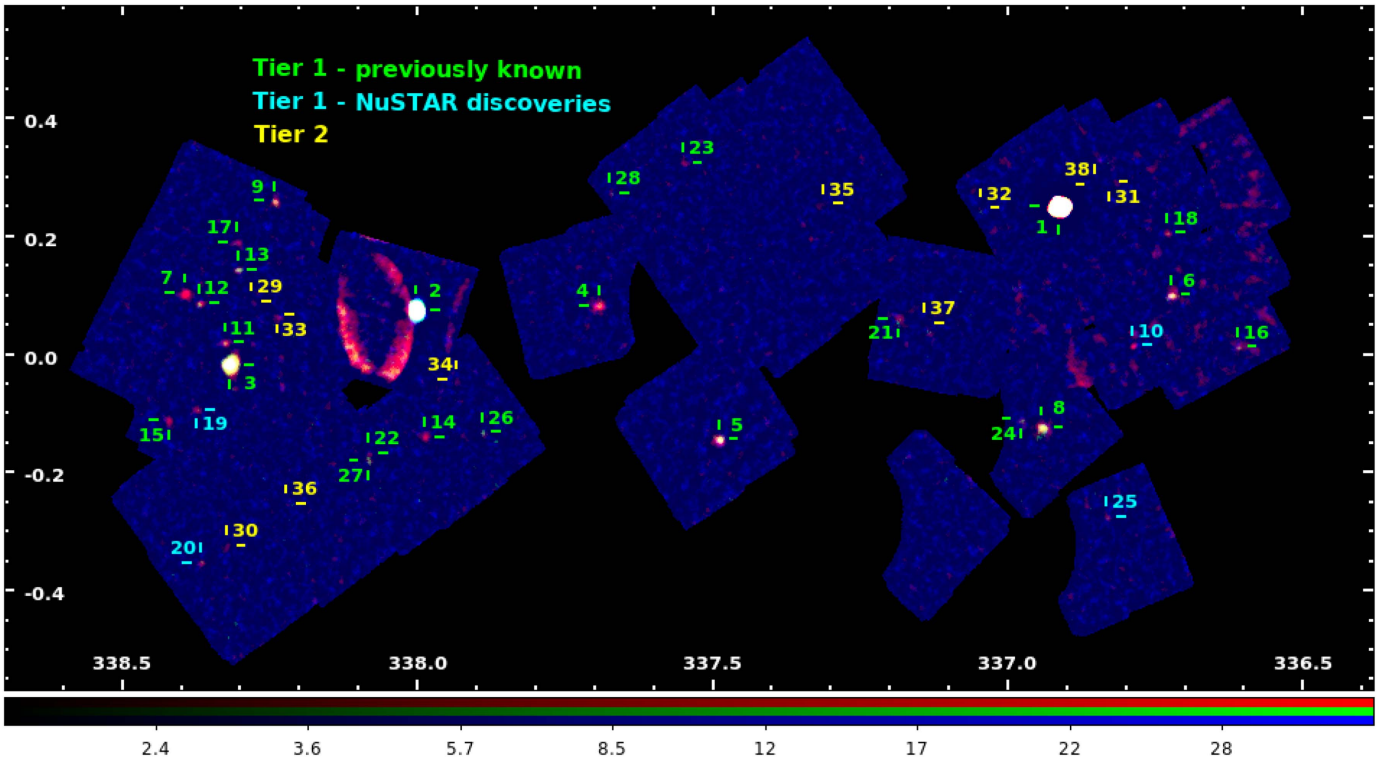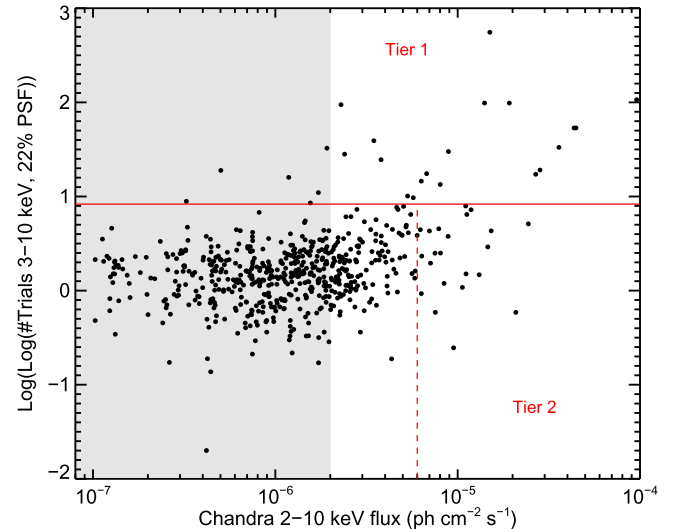
Figure 2. Composite trial map showing the 3–10 keV band in red, 10–20 keV band in green, and 20–40 keV band in blue. The colors are scaled by the logarithmic trial map values. Tier 1 sources are labeled in green, if they were observed by NARCS or were previously well-studied, or cyan, if they were discovered by the *NuSTAR* Norma survey. Tier 2 sources are labeled in yellow. The streaks in the vicinity of NNR 2 are due to stray light that has not been removed because NNR 2 is partially embedded in it. The small streaks seen in the area covered by the first mini-survey are due to ghost rays from NNR 1.
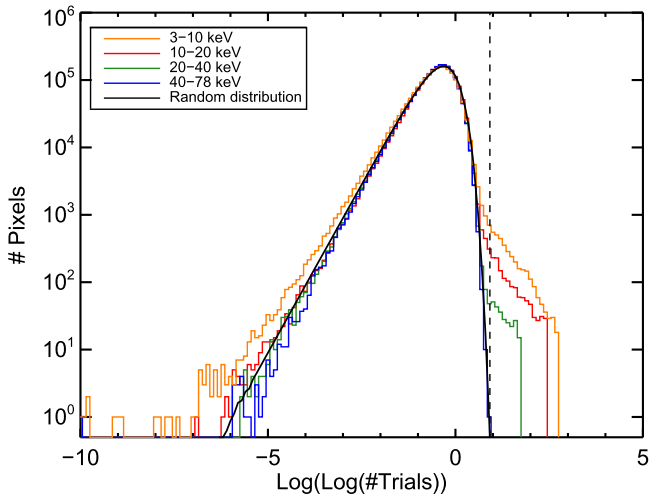
Figure 3. Distribution of trial map values in different energy bands for 22% PSF enclosures. The *x*-axis is shown in a double logarithmic scale. The 40–78 keV distribution closely matches the random distribution expected due to Poissonian fluctuations of the background; this is consistent with the fact that, among the clean observations included in creating this plot, only one source is detected in the 40–78 keV band. The vertical dashed line shows the detection threshold set for the 3–10 keV band trial map. The excess of high trial map values relative to the 40–78 keV band distribution is due to the presence of sources, stray light, and ghost rays; the excess of low trial map values results from the vicinity of bright sources, which effectively increase the local background.

Figure 4. Trial map value in the 3–10 keV band using 22% PSF enclosures vs. *Chandra* 2–10 keV photon flux for NARCS sources in the surveyed *NuSTAR* area. Fluxes of sources in the gray region are uncorrelated with the trial map values and used to set the detection threshold, which is shown by the red horizontal line. Sources above the horizontal line in at least two trial maps are tier 1 sources, while bright sources below that line but to the right of the vertical dashed line are tier 2 candidates.

For a source to be considered for the final catalog, we require that it exceed the detection threshold in at least two trial maps. If all 18 trial maps were independent of each other, the expected number of false sources (N_F) would be equal to $N_{can} C(18, 2) p^{16} (1 - p)^2$, where N_{can} is the number of NARCS

sources included in a *NuSTAR* counterpart search, $C(i, j)$ is a binomial coefficient, and p is the fraction of false sources to be rejected in each map (Hong et al. 2016). However, the trial maps are not completely independent, given that their energy ranges overlap. Thus, to at least partly account for the fact that some of the trial maps are correlated, we set a stringent limit on

the expected number of false sources, setting $N_F = 0.5$. Since the long-term variability of the NARCS sources is unknown, we search for *NuSTAR* detections among all NARCS sources. Thus, in the clean map regions, $N_{can} = 579$; limiting N_F to 0.5 requires a rejection percentage $p = 99.76\%$. Making a cumulative distribution function of the trial map values of uncorrelated NARCS sources lying in the gray area of Figure 4, we determine the corresponding trial value threshold for each trial map; the detection thresholds range from $10^{5.2}$ in the 20–40 keV band with 15% PSF enclosures to $10^{10.3}$ in the 3–10 keV band with 30% PSF enclosures.

Having established detection thresholds for each trial map, we first search for any *Chandra* sources detected by *NuSTAR*. We cross-correlate all NARCS sources detected at $>3\sigma$ in the 2–10 keV *Chandra* band with the trial maps of the full set of observations, including those with significant background contamination. We consider all NARCS sources that exceed the detection threshold in at least two trial maps as tier 1 candidate sources. All sources with 2–10 keV *Chandra* flux $>6 \times 10^{-6}$ cm^{-2} s^{-1} that are not tier 1 sources are considered tier 2 candidate sources, regardless of their trial map values. Although, for tier 2 sources, we do not expect to be able to retrieve significant spectral information, we can at least check for significant variability between the *Chandra* and *NuSTAR* observations and place upper limits on the flux above 10 keV. We also perform a blind search for *NuSTAR* sources that were not detected in NARCS; we consider any clusters of pixels that exceed the detection threshold in at least three trial maps as additional tier 1 candidate sources.

We then inspect all the candidate sources. First, we check whether *NuSTAR* sources matched to *Chandra* counterparts are unique matches. We find 13 cases in which multiple NARCS sources were associated with a single *NuSTAR* detection due to *NuSTAR*'s much larger PSF; however, in all these cases, one NARCS source was more clearly centered on the *NuSTAR* position and was also significantly brighter, demonstrating the more likely association. We then visually inspect all tier 1 candidate sources without NARCS associations to ensure they are not associated with artifacts due to stray light, ghost rays, or the edges of the FOVs. Based on this visual inspection, we exclude three candidate sources located at the edges of the FOVs, the stray light region near NNR 2, and 21 candidates without a clear point-like morphology that are located in the first mini-survey area contaminated by ghost rays. In addition, since tier 2 candidate sources do not exceed the trial map detection thresholds, in order for them to be included in our final catalog, we require that their aperture photometry have a signal-to-noise ratio (S/N) $> 3\sigma$ in at least one of the 3–10, 3–40, or 10–20 keV energy bands (see Section 5.2 for details). In total, after these different screenings, 28 tier 1 candidates and 10 tier 2 candidates are included in our final source list, shown in Table 5.

To determine the best position of the tier 1 *NuSTAR* sources, we applied the DAOPHOT "FIND" algorithm in the proximity of each source in the 3–10 keV trial map with 22% PSF enclosure; we found that using the centroid algorithm on the trial maps rather than the mosaic images yielded better results, allowing the algorithm to converge for all tier 1 sources with lower statistical errors. When applying the centroid algorithm, we used the 3–10 keV, 22% PSF trial map, since all the tier 1 sources are clearly discernible in it.

The tier 2 sources are not bright enough for the centroid algorithm to yield reliable results, so we simply adopted the *Chandra* positions for these sources. The offsets between the tier 1 sources and their *Chandra* counterparts vary from 0″.9 to 14″, excluding two extended sources (NNR 8 and 21) whose *Chandra* positions were determined subjectively by eye. The offsets of four *NuSTAR* point sources from their *Chandra* counterparts are larger than the 90% *NuSTAR* positional uncertainties. We estimated the *NuSTAR* positional uncertainty for each tier 1 source as the quadrature sum of the statistical and systematic uncertainties. We calculated the statistical error by performing Gaussian fits to histograms of the spatial count distributions in the x- and y-directions in a 25×25 pixel image cutout centered on the source position. These statistical errors are approximate, since the *NuSTAR* PSF has non-Gaussian wings, but comparison of the errors derived using the Gaussian approximation to those derived from the accurate PSF simulations performed for some of the brighter sources (see Section 3) indicates that this approximation is accurate to 10%. For the systematic uncertainty, we assumed the nominal 8″ astrometric accuracy (Harrison et al. 2013) for sources located in observations that were not astrometrically corrected and the uncertainties calculated in Section 3 for sources in astrometrically corrected observations. Looking carefully at the four sources with the largest offsets, the similarity between their fluxes and/or spectral properties in the 2–10 keV band between *Chandra* and *NuSTAR* suggests that they are true counterparts despite the large positional offsets. The fact that 17% of the *NuSTAR* offsets exceed the 90% positional uncertainties suggests that the *NuSTAR* positional uncertainty is slightly underestimated. Large offsets between *NuSTAR* positions and soft X-ray counterparts are also seen in the *NuSTAR* serendipitous survey, where Lansbury et al. (2017) find that the 90% positional accuracy of *NuSTAR* varies from 12″ for the most significant detections to 20″ for the least significant detections. The large *NuSTAR* offsets in the serendipitous survey suggest that the 90% *NuSTAR* systematic uncertainty is larger than 8″, which would help to explain some of the large offsets seen for sources in the Norma survey.

Table 5 provides information about the detection, position, and *Chandra* counterparts of all NNR sources. The tier 1 sources include five sources not detected in NARCS; one of them is the well-known LMXB 4U 1630–472 (Kuulkers et al. 1997), while the others are new transient sources discussed in Section 5.5.

5. Aperture Photometry

5.1. Defining Source and Background Regions

For photometry and spectral extraction, we used circular source regions and, whenever possible, annular background regions centered on the source positions provided in Table 5. At energies below 20 keV, the *NuSTAR* background is not uniform; it is dominated by nonfocused emission, which exhibits spatial variations due to shadowing of the focal plane (Harrison et al. 2013). Using aperture regions that are symmetric about the source position helps to compensate for this nonuniformity. We performed our photometric analysis with two different source extraction regions with 30″ and 40″ radii (corresponding to roughly 50% and 60% PSF enclosures, respectively) to assess possible systematic errors associated

Table 5
Source List

Src No. (1)	R.A. (J2000 °) (2)	Decl. (3)	ℓ (J2000 °) (4)	b (5)	Unc. (″) (6)	Source Name (7)	NARCS ID (8)	Offset (″) (9)	Exp. (ks) (10)	No. Trials (10^X) (11)	Band (keV) (12)	EEF (%) (13)	No. Det. (14)
Tier 1													
1	248.5070	−47.3923	336.9119	0.2506	8	4U 1630−472	⋯	⋯	63	1596934.6	3–78	30	18
2	249.7733	−46.7041	338.0014	0.0746	3[a]	IGR J16393−4643	999	2	101	15406.9	3–78	30	18
3	250.1813	−46.5272	338.3198	−0.0173	6[a]	CXOU J164043.5−463135	1321[b]	2	1039	1180.9	3–78	30	17
4	249.4627	−46.9299	337.6914	0.0821	6[a]	CXOU J163750.8−465545	750	3	96	141.2	3–10	30	10
5	249.5112	−47.2327	337.4885	−0.1451	6[a]	CXOU J163802.6−471358	786	1	200	132.6	3–10	30	14
6	248.4812	−47.6342	336.7224	0.0993	8	CXOU J163355.1−473804	78	4	43	92.3	3–78	30	13
7	250.1214	−46.3929	338.3930	0.1026	8	CXOU J164029.5−462329	1278/9[e]	7	215	77.6	3–10	30	6
8	248.9483	−47.6217	336.9445	−0.1241	9	CXOU J163547.0−473739	365[d]	22[a]	94	64.9	3–78	30	12
9	249.8060	−46.4027	338.2412	0.2586	8	CXOU J163912.9−462357	1024	13	87	45.4	3–10	30	12
10	248.6407	−47.6439	336.7881	0.0138	8	NuSTAR J163433−4738.7	⋯	⋯	45[e]	40.6	3–10	30	6
11	250.1467	−46.4991	338.3251	0.0191	9	CXOU J164035.5−462951	1301	7	1123	34.9	3–10	30	10
12	250.1143	−46.4226	338.3676	0.0865	9	CXOU J164027.8−462513	1276	9	654	31.1	3–10	30	10
13	249.9911	−46.4329	338.3035	0.1432	9	CXOU J163957.8−462549	1181	8	208	28.4	3–78	30	12
14	249.9943	−46.8584	337.9869	−0.1410	9	CXOU J163957.2−465126	1180	14	69	28.0	3–10	30	6
15	250.3823	−46.5145	338.4208	−0.1127	9	CXOU J164130.8−463048	1379	10	39	27.7	3–10	30	6
16	248.4639	−47.7762	336.6102	0.0115	10	CXOU J163350.9−474638	72	6	37	21.8	3–78	30	11
17	249.9421	−46.4023	338.3039	0.1888	9	CXOU J163946.1−462359	1137	8	161	19.4	3–10	30	6
18	248.3743	−47.5569	336.7301	0.2048	9	CXOU J163329.5−473332	38	9	37	18.4	3–78	30	6
19	250.3176	−46.5373	338.3743	−0.0943	9	NuSTAR J164116−4632.2	⋯	13	424[e]	15.7	3–10	30	5
20	250.5927	−46.7153	338.3652	−0.3538	9	NuSTAR J164222−4642.9	⋯	4	123	14.9	3–10	30	8
21	248.9882	−47.3188	337.1864	0.0601	12	CXOU J163555.4−471907	402/4[f]	18[a]	47	14.8	3–10	30	3
22	250.1156	−46.8060	338.0812	−0.1684	10	CXOU J164027.6−464814	1273	7	66	13.4	3–10	20	4
23	249.0619	−46.8736	337.5493	0.3228	11	CXOU J163614.2−465222	454	7	86	12.8	3–10	30	6
24	248.9650	−47.5894	336.9760	−0.1106	11	CXOU J163551.8−473523	391	3	187	12.8	3–78	30	4
25	249.0020	−47.8078	336.8313	−0.2763	10	NuSTAR J163600−4748.4	⋯	6	77	11.8	3–78	30	5
26	249.8911	−46.9254	337.8899	−0.1330	9	CXOU J163933.2−465530	1090	7	58	10.8	3–78	30	9
27	250.1304	−46.8142	338.0817	−0.1814	13	CXOU J164031.0−464845	1291	6	121	9.9	10–20	30	3
28	249.2382	−46.8161	337.6730	0.2722	11	CXOU J163657.1−464903	585	6	26	8.5	3–10	20	2
Tier 2													
29	250.0101	−46.5335	338.23700	0.0666	⋯	CXOU J164002.4−463200	1203	⋯	212	8.7	3–10	30	0
30	250.5191	−46.7281	338.32231	−0.3243	⋯	CXOU J164204.5−464341	1408	⋯	177	7.2	3–10	30	0
31	248.3784	−47.4266	336.82764	0.2912	⋯	CXOU J163330.8−472535	40	⋯	11	6.0	3–78	30	0
32	248.6447	−47.2967	337.04544	0.2468	⋯	CXOU J163434.7−471748	139	⋯	20	5.6	10–20	30	0
33	250.0287	−46.4872	338.28012	0.0878	⋯	CXOU J164006.8−462913	1216	⋯	434	5.3	3–10	30	0
34	249.8351	−46.8352	337.93184	−0.0443	⋯	CXOU J163920.4−465006	1039	⋯	29	5.1	3–10	30	0
35	248.9010	−47.0967	337.31056	0.2536	⋯	CXOU J163536.2−470548	325	⋯	115	4.6	10–20	20	0
36	250.3453	−46.7582	338.22112	−0.2546	⋯	CXOU J164122.8−464529	1374	⋯	178	4.4	3–10	30	0

Table 5
(Continued)

Src No. (1)	R.A. (J2000 °) (2)	Decl. (J2000 °) (3)	ℓ (J2000 °) (4)	b (5)	Unc. (″) (6)	Source Name (7)	NARCS ID (8)	Offset (″) (9)	Exp. (ks) (10)	No. Trials (10^X) (11)	Band (keV) (12)	EEF (%) (13)	No. Det. (14)
37	248.9518	−47.3590	337.14012	0.0512	⋯	CXOU J163548.4−472132	373	⋯	89	3.6	40–78	15	0
38	248.4062	−47.4119	336.85116	0.2874	⋯	CXOU J163337.4−472442	52	⋯	21	2.3	3–10	30	0

Notes. (1) NNR source ID. (2)–(5) R.A., decl., Galactic longitude, and Galactic latitude of source determined from centroid algorithm for tier 1 sources and adopting *Chandra* positions from Fornasini et al. (2014) for tier 2 sources. (6) 90% confidence positional uncertainty, including statistical and systematic uncertainties summed in quadrature. In most cases, the 90% confidence systematic uncertainty is 8″; however, for sources that were used to derive astrometric corrections (*), the 90% systematic uncertainty is estimated based on simulations (2″ for NARCS 999 and 6″ for all sources marked with *). Uncertainties for tier 2 sources are not provided, since the positions of these sources are simply set to the *Chandra* positions. (7) NARCS source name or other commonly used name for the source. For *NuSTAR* discoveries, a *NuSTAR* name is provided. (8) NARCS catalog ID number. (9) Angular distance between the source positions in *NuSTAR* and *Chandra* observations. For tier 2 sources, no offset is shown, since the *Chandra*-determined position is adopted for the *NuSTAR* analysis. (10) Total *NuSTAR* exposure, including both modules (FPMA and FPMB) and all observations used in measuring the photometric properties of the source (see Section 5 for details). (11) Maximum value from the trial maps at the location of the source. This value is the number of random trials required to produce the observed counts from a random background fluctuation. For extended sources, this is the maximum trial map value within 30″ of the listed source location. (12) Energy band of the trial map in which the maximum trial value for the source is measured. (13) PSF enclosed energy fraction of the trial map in which the maximum trial value for the source is measured. (14) Total number of trial maps in which the source exceeds the detection threshold. There are 18 trial maps using six different energy bands and three different PSF enclosure fractions. (15) Tier 1 sources are those detected in at least two trial maps. Tier 2 sources are NARCS sources with 2–10 keV fluxes $>6 \times 10^{-6}$ ph cm^{-2} s^{-1} that do not meet the *NuSTAR* detection threshold requirements but have S/N > 3 in the 3–10, 10–20, or 3–40 keV bands (S/N values can be found in Table 6).
[a] These large offsets are due to the fact that the positions for these extended sources were determined by eye in NARCS.
[b] Point source embedded in extended emission. We treat it as a point source and leave the detailed analysis of the extended emission to Gotthelf et al. (2014).
[c] Blend of two *Chandra* sources that are also blended in NARCS but resolved in *Chandra* ObsID 11008 (Rahoui et al. 2014).
[d] Extended source.
[e] For these transient sources, the exposure times listed only include observations in which the source was detected at a $>2\sigma$ level.
[f] In *Chandra*, point source 402 is resolved within extended emission (404), but, in *NuSTAR*, the two are not distinguishable, so we treat it as an extended source.

with aperture selection. The default background regions are annuli with 60″ inner radii and 90″ outer radii. For NNR 8 and 21, which appear extended and are not fully contained within the default source regions, we adopted radii of 45″ and 60″ for the small and large circular source regions, respectively, and annular background regions with 80″ inner radii and 110″ outer radii. We adjusted the centers of the aperture regions for NNR 8 and 21 by 8″ and 5″, respectively, so that they were more centered with respect to the full extended emission rather than the peak of the emission.[23]

For about 1/3 of sources, it was necessary to modify the background aperture regions. In order to prevent contamination to the background from other sources, it is preferable for background regions not to extend within 60″ of any tier 1 source. In addition, above 20 keV, as the relative contribution of the internal background becomes more significant, the background is fairly uniform across any given detector but differs between detectors (Harrison et al. 2013; Wik et al. 2014), so it is advantageous for the background region to be located on the same detector as the source region. Furthermore, when a source is located close to the edge of the FOV, using an annular background region may not sample a statistically large enough number of background counts. Finally, although we removed the most significant patches of stray light and ghost ray contamination from the NuSTAR observations, nonuniform low-level contamination remained. Thus, we modified the background region in situations where the default background region comes within 60″ of any tier 1 source, the low-level contamination from stray light or ghost rays appears to differ significantly between the source and default background regions, or >50% of the annular background region falls outside the observation area or on a detector different from the one where the source is located. In these cases, we adopted a circle with a 70″ radius for the background region and placed it in as ideal a location as possible following these criteria:

  i. Keeping the region as close to the source as possible to minimize variations due to background inhomogeneities but at least 60″ away from the source and any tier 1 sources.
 ii. Maximizing the fraction of the background region area that falls on the same detector as the source region.
iii. Placing the background region at a location that exhibits a level of low-level stray light or ghost ray contamination similar to that of the source region.

For a given source, background aperture regions were defined for each observation and FPM individually, since stray light and ghost ray contamination and the fraction of the default annular background that lies on a given detector vary depending on the observation and the module. Furthermore, if a source fell close to the edge of an observation, such that >50% of the area of a 40″ radius source region was outside the observation area, that observation was not used to extract photometric or spectral information for the source. Thus, the exposure value at the location of a source in the mosaicked exposure map may be higher than the effective exposure for the source based only on observations used for photometric analysis; the latter effective exposure is the value reported in Table 5. Table 6 provides the results of our aperture

photometry and includes flags that indicate which sources required modified background regions.

The only exceptions to this method of defining background regions are NNR 22 and 27. These sources are only separated by 47″ and thus contaminate each other's default background regions, although they do not suffer from any additional background problems. Therefore, since annular background regions are preferable for minimizing the vignetting effect, we simply redefined their background regions as an annulus with an 80″ inner radius and 110″ outer radius centered between the two sources. Due to their proximity, the photometric and spectral properties of these sources as derived from the 40″ radius circular apertures are less reliable than those from the 30″ radius apertures.

5.2. Net Counts and Source Significance

Having defined aperture regions, we extracted the source and background counts for each source in each observation. We then calculated the expected number of background counts ($\langle c_{\rm bkg} \rangle$) in each source region by multiplying the counts in the background region by the ratio $(A_{\rm src} E_{\rm src})/(A_{\rm bkg} E_{\rm bkg})$, where $A_{\rm src}$ and $A_{\rm bkg}$ are the areas in units of pixels and $E_{\rm src}$ and $E_{\rm bkg}$ are the exposures (without vignetting corrections) of the source and background regions, respectively. Then, for each source, we summed the source counts ($C_{\rm src}$), total background counts ($C_{\rm bkg}$), background counts expected in the source region ($\langle C_{\rm bkg} \rangle$), and exposures across all observations and modules in seven different energy bands: 3–78, 3–40, 40–78, 3–10, 10–40, 10–20, and 20–40 keV. The 1σ errors in the total counts were calculated using the recommended approximations for upper and lower limits in Gehrels (1986). Then, the net source counts ($C_{\rm net}$) were calculated by subtracting the total expected background counts in the source region from the total source counts.

In each energy band, we then calculated the S/N of the photometric measurements from the probability that the source could be generated by a noise fluctuation of the local background using the following equation from Weisskopf et al. (2007):

$$
\begin{aligned}
&P(\geqslant C_{\rm src} | C_{\rm bkg}; \ C_{\rm net} = 0) \\
&= \sum_{c = C_{\rm src}}^{C_{\rm bkg} + C_{\rm src}} \frac{(C_{\rm bkg} + C_{\rm src})!}{c!(C_{\rm bkg} + C_{\rm src} - c)!} \left(\frac{f}{1+f} \right)^{c} \\
&\quad \times \left(1 - \frac{f}{1+f} \right)^{C_{\rm bkg} + C_{\rm src} - c},
\end{aligned}
\tag{1}
$$

where $f = \langle C_{\rm bkg} \rangle / C_{\rm bkg}$. Using this probability, we defined the S/N as the equivalent Gaussian significance in units of the standard deviation (e.g., $P = 0.0013$ corresponds to S/N $= 3\sigma$). These S/N measurements were used to select which tier 2 sources to include in our catalog but not to set detection thresholds for tier 1 sources, which are determined by the trial maps. Only five sources have photometric measurements with S/N $\geqslant 3\sigma$ above 20 keV. Therefore, we focused the remainder of our analysis on the 3–40, 3–10, and 10–20 keV energy bands. Of the tier 2 source candidates, we only included those with S/N $\geqslant 3\sigma$ in at least one of these three energy bands, using either of the two source aperture regions, in our final source list. Table 6 provides the significance of each source in our final catalog in these three

---

[23] The adjusted locations of the aperture regions for NNR 8 and 21 are (α, δ) = (248.9468, −47.6238) and (248.9875, −47.3200), respectively.

Table 6
Photometry

Source No. (1)	S/N 3–40 keV (2)	S/N 3–10 keV (3)	S/N 10–20 keV (4)	Net Counts 3–40 keV (5)	Ph. Flux (10^{-6} cm^{-2} s^{-1}) 3–10 keV (6)	10–20 keV (7)	En. Flux (10^{-14} erg cm^{-2} s^{-1}) 3–10 keV (8)	10–20 keV (9)	Hardness Ratio (10)	E_{50} (keV) (11)	QR (12)	Var. Flag NuST. (13)	Var. Flag Chan. (14)	Aperture Flag (15)
Tier 1														
1	134534.5	142889.4	15742.0	3214900 ± 18000	598180 ± 340	19112 ± 55	473890 ± 270	38210 ± 110	−0.9246	5.3245	1.0334	l	—	pcm
	130019.1	138317.1	15422.4	4079200 ± 2000	603320 ± 300	19060 ± 49	477130 ± 240	38119 ± 100	± 0.0008	± 0.0006	± 0.0004			
2	616.4	350.0	648.6	37360 ± 200	1634 ± 14	1710 ± 14	1748 ± 14	3954 ± 32	−0.112	9.83	1.077	sp[a]	slp	pcm
	581.4	331.0	614.8	46720 ± 240	1623 ± 13	1694 ± 13	1737 ± 13	3914 ± 29	± 0.006	± 0.03	± +0.006			
3	144.2	128.5	84.4	9590 ± 120	50.1 ± 0.8	21.5 ± 0.5	46.4 ± 0.7	48.7 ± 1.2	−0.41 ± 0.01	8.0 ± 0.1	0.90 ± +0.02	sp[a]		pcm
	153.3	140.4	87.4	13550 ± 150	57.9 ± 0.8	23.3 ± 0.5	53.3 ± 0.7	52.7 ± 1.2						
4	21.3	24.6	6.5	556 ± 32	49.1 ± 2.7	7.6 ± 1.3	40.3 ± 2.2	18.8 ± 3.2	−0.72 ± 0.06	6.4 ± 0.1	0.92 ± +0.10	l	slp	pcm
	20.3	23.3	5.9	723 ± 40	50.8 ± 2.7	7.8 ± 1.4	41.8 ± 2.2	19.7 ± 3.4						
5	23.0	22.9	9.6	842 ± 42	23.6 ± 1.3	6.4 ± 0.8	21.6 ± 1.2	13.7 ± 2.0	−0.55 ± 0.06	7.8 ± 0.3	0.93 ± +0.06			p
	21.4	21.3	9.1	1087 ± 55	24.0 ± 1.4	6.9 ± 0.9	22.0 ± 1.2	14.7 ± 2.2						
6	14.3	12.8	6.9	359 ± 29	77.8 ± 7.7	18.0 ± 3.2	67.7 ± 6.2	40.0 ± 7.1	−0.63 ± 0.09	6.5 ± 0.2	0.91 ± +0.14			pc
	13.4	11.7	7.3	464 ± 38	76.0 ± 8.0	21.2 ± 3.3	67.6 ± 6.5	46.4 ± 7.5						
7	17.5	20.6	1.7	621 ± 40	37.4 ± 2.2	1.1 ± 0.8	29.6 ± 1.7	$1.7^{+2.0}_{-1.7}$	−0.92 ± 0.08	5.5 ± 0.2	0.90 ± +0.06			pc
	17.0	19.6	3.0	835 ± 53	38.1 ± 2.2	2.3 ± 1.0	30.6 ± 1.8	4.4 ± 2.2						
8	24.9	22.3	14.4	884 ± 41	40.5 ± 2.3	17.0 ± 1.4	37.6 ± 2.0	37.4 ± 3.3	−0.41 ± 0.05	8.0 ± 0.2	0.90 ± +0.06			e
	21.9	20.0	12.5	1083 ± 52	44.9 ± 2.5	17.6 ± 1.6	40.7 ± 2.2	38.3 ± 3.7						
9	13.4	13.3	7.1	303 ± 26	33.9 ± 3.2	14.1 ± 2.5	32.1 ± 3.0	30.8 ± 5.6	−0.47 ± 0.09	7.5 ± 0.4	1.02 ± +0.11			p
	11.9	12.5	5.8	371 ± 34	37.1 ± 3.4	12.9 ± 2.5	33.4 ± 3.0	28.5 ± 5.9						
10	9.7	10.6	1.7	240 ± 27	84.0 ± 9.1	$4.0^{+3.1}_{-2.8}$	67.3 ± 7.1	$8.0^{+7.0}_{-6.3}$	$-0.89^{+0.14}_{-0.11}$	5.6 ± 0.3	0.83 ± +0.11	l	—	p
	6.5	6.9	1.6	220 ± 35	56.2 ± 9.1	3.8 ± 3.1	46.5 ± 7.1	6.9 ± 6.9						
11	17.1	18.8	6.8	1310 ± 81	9.8 ± 0.6	1.9 ± 0.3	8.3 ± 0.5	4.1 ± 0.8	−0.64 ± 0.07	6.4 ± 0.1	0.92 ± +0.08	l		pcm
	17.1	19.0	6.6	1830 ± 110	10.9 ± 0.6	2.1 ± 0.4	9.4 ± 0.5	4.6 ± 0.8						
12	12.6	13.9	5.0	687 ± 58	11.1 ± 0.9	2.2 ± 0.5	9.7 ± 0.8	4.5 ± 1.2	−0.65 ± 0.09	6.6 ± 0.2	1.06 ± +0.15			pcm
	12.2	13.7	5.0	929 ± 79	12.1 ± 1.0	2.5 ± 0.6	10.5 ± 0.8	5.3 ± 1.4						
13	10.5	8.6	6.6	339 ± 35	10.1 ± 1.5	5.8 ± 1.0	9.7 ± 1.3	13.4 ± 2.4	−0.34 ± 0.11	8.9 ± 0.7	0.95 ± +0.11			p
	9.3	7.4	6.1	418 ± 47	9.5 ± 1.6	5.9 ± 1.0	9.2 ± 1.3	13.5 ± 2.5						
14	7.7	9.9	0.9	159 ± 23	20.9 ± 2.5	<3.6	17.2 ± 2.1	<8.8	>−1	5.7 ± 0.4	1.11 ± +0.19			p
	6.5	9.3	0.3	187 ± 30	21.6 ± 2.5	<3.2	17.7 ± 2.1	<7.8						
15	6.0	7.8	0.6	89 ± 16	28.6 ± 4.4	<3.9	23.5 ± 3.6	<8.5	>−1	5.6 ± 0.6	0.87 ± +0.13	s		p
	6.0	7.5	0.3	125 ± 22	31.2 ± 4.6	<3.9	24.7 ± 3.7	<9.0						
16	9.6	8.5	4.2	287 ± 32	60.8 ± 8.9	$10.2^{+3.0}_{-2.8}$	54.9 ± 7.1	$22.5^{+6.7}_{-6.1}$	−0.71 ± 0.14	6.4 ± 0.3	0.85 ± +0.10			p
	9.4	8.5	3.4	393 ± 44	65.7 ± 9.6	8.6 ± 2.8	60.2 ± 7.7	18.7 ± 6.3						
17	7.8	8.1	3.0	215 ± 30	9.0 ± 1.5	2.5 ± 1.0	9.2 ± 1.3	5.0 ± 2.3	−0.62 ± 0.15	7.3 ± 0.5	1.13 ± +0.22			p
	7.5	7.3	3.9	292 ± 40	9.2 ± 1.7	3.8 ± 1.1	9.3 ± 1.4	8.3 ± 2.6						
18	6.3	6.6	1.9	134 ± 23	47.7 ± 8.0	$3.7^{+3.1}_{-2.7}$	38.1 ± 6.2	$5.8^{+6.6}_{-5.8}$	$-0.78^{+0.21}_{-0.20}$	5.9 ± 0.7	0.54 ± +0.09		s	pc
	5.4	5.8	1.5	159 ± 30	47.8 ± 8.5	$3.3^{+3.3}_{-3.1}$	37.5 ± 6.6	$5.6^{+7.4}_{-5.6}$						
19	10.3	11.7	2.7	399 ± 41	11.0 ± 1.1	1.6 ± 0.6	9.5 ± 0.9	3.7 ± 1.5	−0.77 ± 0.12	6.6 ± 0.2	1.09 ± +0.18	l	—	p
	9.0	10.5	2.0	487 ± 56	11.1 ± 1.2	1.3 ± 0.7	9.4 ± 1.0	3.1 ± 1.6						
20	5.9	6.7	3.3	126 ± 23	10.0 ± 1.9	$4.5^{+1.5}_{-1.3}$	9.4 ± 1.6	$11.7^{+3.6}_{-3.3}$	−0.53 ± 0.17	6.8 ± 0.6	1.27 ± +0.39	l	—	p
	6.4	7.1	3.5	191 ± 31	11.8 ± 2.0	5.0 ± 1.4	11.1 ± 1.7	12.4 ± 3.3						
21	13.4	13.5	6.1	312 ± 26	46.4 ± 4.1	12.1 ± 2.4	39.9 ± 3.5	26.0 ± 5.4	−0.58 ± 0.09	6.7 ± 0.3	0.79 ± +0.11			e
	12.3	12.7	5.5	408 ± 35	52.3 ± 4.5	13.4 ± 2.7	45.4 ± 3.8	29.9 ± 6.3						
22	6.0	7.4	1.4	96 ± 18	17.5 ± 2.7	$2.1^{+2.2}_{-2.0}$	15.0 ± 2.3	$4.3^{+5.2}_{-4.3}$	$-0.75^{+0.22}_{-0.21}$	6.9 ± 0.5	1.30 ± +0.43			p
	5.9	7.6	1.4	132 ± 23	20.0 ± 2.9	2.3 ± 2.2	17.3 ± 2.4	$4.3^{+5.1}_{-4.3}$						
23	6.0	5.9	2.7	108 ± 20	8.4 ± 1.8	$2.6^{+1.2}_{-1.1}$	7.6 ± 1.5	$6.0^{+2.8}_{-2.5}$	−0.55 ± 0.20	7.4 ± 0.9	0.91 ± +0.30			p
	4.8	4.9	2.2	122 ± 26	7.5 ± 1.9	2.1 ± 1.1	7.1 ± 1.6	4.4 ± 2.6						
24	6.7	5.0	4.0	198 ± 31	6.8 ± 1.2	2.3 ± 0.6	5.3 ± 1.0	4.7 ± 1.5	−0.37 ± 0.18	9.0 ± 2.1	0.35 ± +0.10			pcm
	5.4	3.5	3.0	222 ± 42	5.9 ± 1.3	1.9 ± 0.7	4.6 ± 1.0	3.7 ± 1.6						
25	6.0	5.8	1.4	98 ± 18	6.4 ± 1.5	$1.4^{+0.9}_{-0.8}$	6.4 ± 1.3	$3.8^{+2.4}_{-2.1}$	$-0.74^{+0.25}_{-0.24}$	8.1 ± 0.9	0.60 ± +0.25	l	—	p
	6.2	5.5	2.0	144 ± 24	6.8 ± 1.6	$1.8^{+1.0}_{-0.9}$	6.7 ± 1.3	$4.6^{+2.4}_{-2.2}$						

Table 6
(Continued)

Source No. (1)	S/N 3–40 keV (2)	S/N 3–10 keV (3)	S/N 10–20 keV (4)	Net Counts 3–40 keV (5)	Ph. Flux (10^{-6} cm^{-2} s^{-1}) 3–10 keV (6)	Ph. Flux 10–20 keV (7)	En. Flux (10^{-14} erg cm^{-2} s^{-1}) 3–10 keV (8)	En. Flux 10–20 keV (9)	Hardness Ratio (10)	E_{50} (keV) (11)	QR (12)	Var. Flag NuST. (13)	Var. Flag Chan. (14)	Aperture Flag (15)
26	6.0	5.7	4.3	107 ± 19	11.5 ± 2.2	6.6 ± 1.7	9.5 ± 1.8	16.6 ± 4.1	-0.25 ± 0.16	8.3 ± 0.9	$0.55 \pm +0.16$			pcm
	6.1	6.1	4.1	152 ± 26	13.2 ± 2.3	6.4 ± 1.7	11.5 ± 2.0	14.8 ± 4.1						
27	7.3	6.0	5.3	179 ± 26	11.0 ± 2.1	8.5 ± 1.8	10.0 ± 1.8	20.3 ± 4.3	-0.20 ± 0.14	8.3 ± 1.1	$0.75 \pm +0.18$	1		p
	7.4	6.5	5.0	252 ± 35	13.9 ± 2.3	9.1 ± 1.9	12.4 ± 2.0	22.5 ± 4.6						
28	3.5	2.7	2.7	32^{+11}_{-10}	$15.3^{+7.0}_{-5.9}$	$11.6^{+6.1}_{-4.9}$	$11.9^{+5.7}_{-4.9}$	$28.7^{+15.3}_{-12.2}$	$-0.17^{+0.36}_{-0.30}$	10.3 ± 4.1	$0.42 \pm +0.26$	1		p
	3.0	2.1	2.2	37 ± 13	$11.5^{+6.6}_{-5.8}$	$10.4^{+5.9}_{-4.9}$	$9.4^{+5.6}_{-4.9}$	$25.7^{+14.8}_{-12.2}$						
Tier 2														
29	5.5	6.0	2.3	169 ± 32	9.1 ± 1.7	2.3 ± 1.1	8.1 ± 1.4	5.0 ± 2.7	-0.60 ± 0.20	7.5 ± 0.8	$0.94 \pm +0.30$	1		pcm
	4.7	5.5	3.0	201 ± 43	9.0 ± 1.8	3.5 ± 1.3	8.2 ± 1.5	7.5 ± 3.0						
30	4.7	6.1	0.9	128 ± 28	6.6 ± 1.3	<2.4	6.1 ± 1.1	<15.9	>-1	6.3 ± 0.6	$0.93 \pm +0.41$			pcm
	3.9	5.8	0.8	147 ± 39	7.9 ± 1.5	<2.5	6.6 ± 1.2	<6.2						
31	4.6	3.9	1.5	29^{+9}_{-8}	$37.7^{+15.8}_{-13.3}$	$10.4^{+10.2}_{-7.5}$	$35.3^{+13.7}_{-11.6}$	$23.7^{+23.5}_{-17.2}$	$-0.61^{+0.42}_{-0.34}$	7.0 ± 2.3	$0.67 \pm +0.44$			pc
	4.5	3.7	1.7	38^{+11}_{-10}	$29.9^{+13.9}_{-12.2}$	$12.3^{+9.7}_{-7.7}$	$33.1^{+12.6}_{-11.0}$	$28.1^{+22.4}_{-17.6}$						
32	2.5	1.9	1.9	18^{+9}_{-8}	$9.0^{+6.4}_{-5.3}$	$8.5^{+6.2}_{-4.9}$	$8.4^{+5.6}_{-4.6}$	$19.1^{+14.6}_{-11.5}$	$-0.11^{+0.49}_{-0.39}$	10.1 ± 3.8	$0.68^{+0.56}_{-0.68}$			p
	3.0	1.6	2.3	32^{+12}_{-11}	$10.0^{+6.8}_{-5.8}$	$11.7^{+6.5}_{-5.4}$	$8.1^{+5.7}_{-4.8}$	$26.4^{+15.3}_{-12.6}$						
33	2.5	3.4	0.5	113 ± 45	3.2 ± 1.3	<1.6	3.2 ± 1.0	<17.4	>-1	6.6 ± 0.4	$1.62 \pm +0.57$		1	p
	2.0	2.8	0.0	125 ± 63	2.9 ± 1.4	<1.3	3.0 ± 1.1	<3.1						
34	3.1	3.3	1.5	46 ± 15	14.6 ± 4.7	$5.1^{+4.2}_{-3.7}$	12.6 ± 4.1	$11.1^{+10.0}_{-8.9}$	$-0.49^{+0.34}_{-0.33}$	6.2 ± 1.4	$0.83 \pm +0.38$			p
	2.4	3.2	0.5	49 ± 21	17.4 ± 5.2	<7.9	13.9 ± 4.5	<18.7						
35	4.1	3.6	3.3	85 ± 22	5.4 ± 1.6	$3.4^{+1.2}_{-1.1}$	4.4 ± 1.3	$8.3^{+2.8}_{-2.5}$	-0.25 ± 0.23	7.4 ± 1.0	$0.82 \pm +0.37$	1		p
	3.6	4.2	1.5	104 ± 30	6.6 ± 1.8	1.6 ± 1.1	5.7 ± 1.5	3.8 ± 2.5						
36	3.5	1.7	3.2	101 ± 29	3.3 ± 1.5	3.5 ± 1.2	2.1 ± 1.2	8.4 ± 2.9	0.17 ± 0.31	11.8 ± 3.3	$0.48^{+0.42}_{-0.48}$	1	sl	p
	4.2	2.4	3.5	168 ± 41	4.7 ± 1.7	4.4 ± 1.3	3.1 ± 1.4	10.6 ± 3.2						
37	2.2	2.2	1.0	40 ± 18	3.4 ± 1.6	$1.2^{+1.1}_{-1.0}$	2.7 ± 1.3	$3.2^{+2.7}_{-2.4}$	$-0.56^{+0.51}_{-0.44}$	6.5 ± 2.0	$0.32^{+0.50}_{-0.32}$			p
	3.4	3.2	1.4	84 ± 25	6.7 ± 1.9	$1.8^{+1.2}_{-1.1}$	5.0 ± 1.6	$4.8^{+2.9}_{-2.7}$						
38	2.8	3.7	0.5	23^{+10}_{-9}	$11.4^{+4.3}_{-3.8}$	<4.4	$10.7^{+3.7}_{-3.2}$	<11.5	>-1	7.1 ± 1.6	$0.61^{+0.60}_{-0.61}$			pc
	3.2	3.3	1.6	37 ± 12	$11.4^{+4.3}_{-3.9}$	$3.6^{+2.6}_{-2.2}$	$10.0^{+3.6}_{-3.2}$	$8.9^{+6.2}_{-5.1}$						

Notes. (2)–(9) S/Ns, net counts, photon flux, and energy flux of the source in the specified energy bands. Values in the top (bottom) row for each entry are based on using source aperture regions with small (large) radii. All other table column values are based on using small aperture regions. (10) Hardness ratio is defined as (H–S)/(H+S), where H represents the net counts in the 10–20 keV band and S represents the net counts in the 3–10 keV band. (11)–(12) Median energy in the 3–40 keV band and the y-value of the quantile plot, defined as $3(E_{25}\text{-3 keV})/(E_{75}\text{-3 keV})$. (13) Flags indicating source variability: "s" = short timescale (< a few hours) variability, "l" = long timescale (weeks–years) variability, "p" = periodic modulations detected. See Section 5.4 for details. (14) Variability flags from Fornasini et al. (2014): "s" = short timescale (< a few hours) variability (within a single observation, the Kolmogorov–Smirnov test probability that the source is constant is <0.3%), "l" = long timescale (days–weeks) variability (the 0.5–10, 0.5–2, or 2–10 keV photon flux varies by >3σ between NARCS observations), "p" = periodic modulations detected by the Z_n^2 test, "–" = source not detected in NARCS. (15) "p" = point-source region aperture (circle with 30″/40″ radius), "e" = extended source aperture (circle with 45″/60″ radius), "c" = background region is a circle with 70″ radius offset from the source rather than an annulus centered on the source, "m" = stray light and background spatial variations require background regions to be modified for each observation.
[a] Periodic variability for NNR 2 detected by Bodaghee et al. (2016) and for NNR 3 by Gotthelf et al. (2014).

energy bands, the net counts in the 3–40 keV band, and additional photometric properties described in the following sections. We estimate that local spatial variations of the background could affect the S/N values reported in this table by $\pm0.4\sigma$ and change the measured net counts and fluxes by $\pm5\%$, variations that are smaller than the statistical uncertainties of the photometric measurements.

5.3. Photon and Energy Fluxes

In Section 5.7, we describe how we derived fluxes from spectral modeling. However, for all sources, we also derived fluxes in a model-independent way, since the spectral fitting of faint sources is prone to significant uncertainty. For each source and background region in each observation and module, we used `nuproducts` to extract a list of photon counts as a function of energy and generate both an ARF and a response matrix file (RMF); the ARFs are scaled by the PSF energy fraction enclosed by the aperture region. We first calculated the source photon flux within each observation and module in the 3–10 and 10–20 keV bands by dividing the counts in each channel by the corresponding ARF, summing all these values within the given energy band, and dividing by the source region exposure. The estimated background contribution, scaled from the photon flux measured in the background region, was subtracted. These photon flux measurements assume a quantum efficiency of 1; this is a decent approximation for the *NuSTAR* CdZnTe detectors, which have a quantum efficiency of 0.98 over the vast majority of the *NuSTAR* energy range (Bhalerao 2012). If the significance of a source in a particular observation was $<1\sigma$, then we calculated a 90% confidence upper limit to its photon flux by converting the probability distribution of true source counts (from Equation (A21) in Weisskopf et al. 2007) to a photon flux distribution using the source region effective area.

For the five transient sources that were detected by *NuSTAR* but not by NARCS, we looked at the light curves of the 3–10 keV photon fluxes to check whether they are detected at $>2\sigma$ confidence in individual *NuSTAR* observations. We found that NNR 1 is only detected in ObsIDs 40014008002 and 40014009001, NNR 10 is only detected in ObsID 40014007001 (which is consistent with T14), and NNR 19 is only detected in ObsIDs 30002021005, 30002021007, 30002021009, 30002021011, and 30002021013. Excluding the observations in which the transient sources are not detected, we reevaluated their 3–40 keV net counts and source significance as described in Section 5.2 and continued to exclude these observations for these sources when determining their other average photometric and spectral properties. Thus, the photometric and spectral properties derived for NNR 1, 10, 19, and 25 should be considered as their average properties during high flux states.

For each source, we then computed average 3–10 and 10–20 keV photon fluxes by combining the count lists and ARFs from different observations and modules. These measurements are presented in Table 6. We also calculated the average 3–10 and 10–20 keV energy flux for each source using the same model-independent method but with the additional step of multiplying the source counts in each channel by the channel energy. Fluxes derived using the two different source region sizes are in 1σ agreement with one another, except for three sources that are located in regions of diffuse emission or ghost rays and thus do not appear as exactly

point-like. Comparing the model-independent fluxes with those we derived from spectral modeling (see Section 5.7) for tier 1 sources, we find that they are in good agreement when using the smaller aperture regions but show a significant number of discrepancies at $>2\sigma$ confidence when using the larger aperture regions. In the larger aperture regions, while the net number of source counts is higher, so is the background/source count ratio, which is why in most cases the source significance derived from the larger aperture regions is slightly lower. As a result, accurate background subtraction is more important when using the larger aperture regions, and it is not surprising that our crude subtraction method, which assumes a spectrally flat background, for the model-independent fluxes leads to discrepancies with the spectral fluxes.

5.4. X-Ray Variability

NuSTAR's high time resolution allows us to characterize the timing properties of detected sources over a range of timescales. *NuSTAR*'s time resolution is good to ~2 ms rms after being corrected for thermal drift of the onboard clock, and the absolute accuracy is known to be better than <3 ms (Mori et al. 2014; Madsen et al. 2015). For our timing studies, all photon arrival times were converted to barycentric dynamical time (TDB) using the *NuSTAR* coordinates of each point source.

To characterize the source variability on $\sim$hourly timescales, we used the Kolmogorov–Smirnov (KS) statistic to compare the temporal distributions of X-ray events extracted from source and background apertures in the 3–20 keV energy band. The background light curve acts as a model for the count rate variations expected in the source region due to the background. The maximal difference between the two cumulative normalized light curves gives the probability that they are drawn from the same distribution, i.e., that the light curve in the source region is consistent with that expected from the background plus a source with constant flux. Any source with a KS statistic lower than 0.05% in any observation is flagged as short-term variable by an "s" in Table 6. For each source, we ran the KS test independently for each of the observations in which it was covered. Since the KS test was applied 160 times in total, the adopted threshold corresponds to $\lesssim1$ spurious detection. We identified two sources as variable using the KS test. An examination of the light curves of these sources, NNR 2 (presented in B16) and NNR 15 (Figure 5), shows clear variability on $\sim$hourly timescales.

We checked for variability of the NNR sources on week-to-year timescales by comparing the flux detected between repeated *NuSTAR* observations. Sources were flagged as long-term variable with an "l" in Table 6 if their 3–10 keV photon flux differed by $>3\sigma$ based on their flux measured uncertainties; given the number of flux comparisons performed, this 3σ threshold should result in $\lesssim1$ spurious detection. NNR 1, 10, 11, 19, and 29 were found to be variable using this criterion. In addition, we compared *Chandra* and *NuSTAR* fluxes to check for variability on year timescales. For all sources with sufficient photon statistics, we compared the joint spectral fits to *Chandra* and *NuSTAR* data (see Section 5.7 for details) and identified sources with normalizations that differed at the $>90\%$ confidence level. Since we performed these joint fits for 24 sources, we would expect as many as 2 spurious detections of variability. But we made the criterion more stringent by requiring that, for a source to be considered
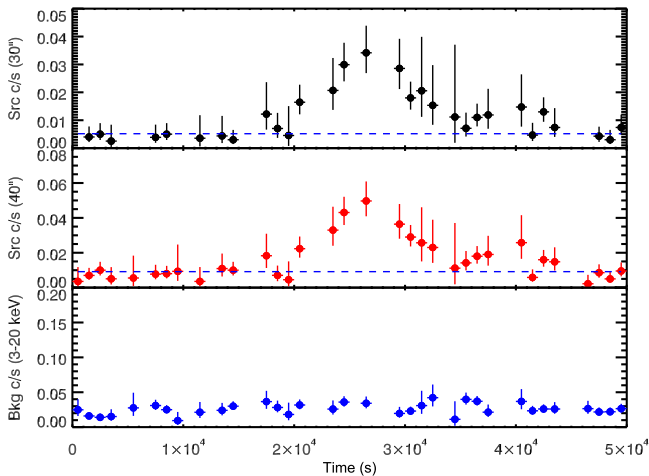
Figure 5. Light curve of NNR 15 in the *NuSTAR* 3–20 keV band from ObsID 40014016001, FPMA and FPMB combined, as measured from an aperture region with a 30″ radius (top) and a 40″ radius (middle). The light curve exhibits evident short-term variability. The bottom panel displays the light curve extracted from the background aperture region. The blue dashed lines in the top two panels show the mean background count rate scaled by the source region area. The light curves display the average count rate in each 1 ks time interval; note that during some of these time intervals, the effective exposure time is less than 1 ks due to Earth occultations or periods of poor data quality.

Table 7
X-Ray Variability

Source No. (1)	*NuSTAR* Var. Flag (2)	Maximum 3–10 keV Flux (10^{-6} ph cm^{-2} s^{-1}) (3)	Variability Amplitude 3–10 keV (4)	Criteria for Long-Term Var. Detection (5)
Tier 1				
1	l	641200 ± 700	>427500	T, N
2	sp	10100 ± 700	>34	⋯
4	l	71^{+2}_{-5}	$1.5^{+0.1}_{-0.2}$	CS
10	l	84 ± 9	>56	T, N
11	l	26 ± 4	>18	N, CS
15	s	220 ± 40	>6	⋯
19	l	11 ± 1	>7	T, N
20	l	10 ± 2	>2	CS
25	l	6 ± 1	>4	T
27	l	11 ± 2	$2.2^{+1.6}_{-0.9}$	CS
28	l	15^{+7}_{-6}	11^{+8}_{-6}	CQ
Tier 2				
29	l	40 ± 7	6.5 ± 1.3	N
35	l	13 ± 2	2.5 ± 0.6	CQ
36	l	9^{+2}_{-1}	2.8 ± 1.4	CQ

Notes. (2) *NuSTAR* variability flag: "s" = short timescale (< a few hours) variability, "l" = long timescale (weeks–years) variability, "p" = periodic modulations detected. See Section 5.4 for details. (3) Maximum 3–10 keV photon flux from either *Chandra* or *NuSTAR* photometry (based on 30″ radius aperture regions). (4) Ratio of maximum to minimum 3–10 keV photon fluxes. (5) Criteria by which long-term variability was determined for sources flagged with "l": T = transient source is detected by *NuSTAR* but falls below the survey sensitivity of NARCS, N = photon flux varies by $>3\sigma$ between different *NuSTAR* observations, CS = cross-normalization between *Chandra* and *NuSTAR* spectra is inconsistent at $>90\%$ confidence, CQ = *Chandra* 2–10 keV and *NuSTAR* 3–10 keV photon fluxes are inconsistent at $>90\%$ confidence when adopting a range of spectral models consistent with the quantile values of the source.

variable between the *Chandra* and *NuSTAR* observations, its *Chandra* and *NuSTAR* normalizations must be inconsistent regardless of which of three different spectral models is adopted. This more selective criterion is only met by NNR 4, 11, and 27. For fainter sources (NNR 29–38), we considered a range of spectral models that would be consistent with their quantile values and assessed whether their 2–10 keV *Chandra* flux was incompatible with their average 3–10 keV *NuSTAR* flux at $>90\%$ confidence, regardless of the spectral model assumed. NNR 28, 35, and 36 are found to be variable by this criterion. In Table 7, we provide maximum photon fluxes and the ratio of maximum and minimum fluxes for all *NuSTAR* sources that demonstrate X-ray variability; the transient sources, NNR 1, 10, 19, 20, and 25—which are detected by *NuSTAR* but not detected in NARCS—are flagged as long-term variable and included in this table as well.

We searched for a periodic signal from the *NuSTAR* sources with sufficient counts to detect a coherent timing signal, determined as follows. The ability to detect pulsations depends strongly on the source and background counts and the number of search trials. For a sinusoidal signal, the aperture counts (source plus background) necessary to detect a signal of pulsed fraction f_p is $N = 2S/f_p^2$, where S is the power associated with the single trial false detection probability of a test signal $\wp = e^{-S/2}$; S is distributed as χ^2 with two degrees of freedom (van der Klis 1989). In practice, for a blind search, we need to take into account the number of frequencies tested, $N_{\text{trials}} = T_{\text{span}}/f_{\text{Nyq}}$, when T_{span} is the data span and $f_{\text{Nyq}} = 250$ Hz, the effective *NuSTAR* Nyquist frequency. In computing N, we must allow for the reduced sensitivity of the search due to background contamination in the source aperture (N_b); the minimum detectable pulse fraction f_p (min) is then increased by $(N_s + N_b)/N_s$.

We computed the detectability in individual observations for each source in our sample and considered those suitable for a pulsar search, with f_p (min) $> 50\%$ at the 3σ level. For the three brightest sources in the Norma survey, the timing properties are already presented elsewhere: (i) the

quasi-periodic oscillations of the BH binary 4U 1630−472 (NNR 1), extensively studied using the *Rossi X-Ray Timing Explorer* (Dieters et al. 2000; Tomsick & Kaaret 2000; Seifina et al. 2014); (ii) the HMXB pulsar IGR J16393−4643 (NNR 2), with a period of 904 s, whose spin-up rate was determined from recent *NuSTAR* observations (B16); and (iii) the *NuSTAR*-discovered 206 ms pulsar PSR J1640−4631 (NNR 3), associated with the TeV source HESS J1640−465 (G14; Archibald et al. 2016).

For NNR 4, 5, 8, and 21, we extracted event lists in the 3–20 keV band from $r = 40''$ radius apertures and searched for periodic signals between 4 ms and 100 s. For each source, we evaluated the power at each frequency (oversampling by a factor of 2) using the unbinned Z_n^2 test statistic (Buccheri et al. 1983) summed over $n = 1, 2, 3, 5$ harmonics, to be sensitive to both broad and narrow pulse profiles. We repeated our search for an additional combination of energy ranges $3 < E < 25$ keV, $3 < E < 10$ keV, $10 < E < 25$ keV, and $10 < E < 40$ keV and aperture size $r < 20''$ and $r < 30''$. For all these searches, no significant signals were detected. For NNR 5 and 8, we can constrain the pulsed fraction of X-ray emission to be $<45\%$ and $<48\%$, respectively, at the 3σ confidence. We also performed periodic searches for longer periods, with special attention to NNR 4, for which *Chandra* detected a 7150 s period, but we were unable to pick out any

Table 8
Properties of *Chandra* Counterparts to *NuSTAR* Discoveries

Source No.	R.A.	Decl.	Position	Significance	Net Counts	E_{50}	QR
	J2000 (°)		Uncertainty ($''$)	0.5–10 keV	0.5–10 keV	(keV)	
(1)	(2)	(3)	(4)	(5)	(6)	(7)	(8)
19	250.315033	−46.540543	0.68	15	245^{+17}_{-16}	2.9 ± 0.2	0.92 ± 0.06
20	250.591644	−46.716049	0.87	2.9	3^{+3}_{-2}	$\ldots^{\text{a}}$	$\ldots$
25	248.999542	−47.807671	0.71	6	33^{+7}_{-6}	2.3 ± 0.4	0.9 ± 0.3

Note. (4) 90% statistical and systematic positional uncertainties summed in quadrature.

[a] The *Chandra* counterpart of NNR 20 has too few counts to perform quantile analysis. The energies of the three photons attributed to this source are 4.2, 5.7, and 7.0 keV. Since the *Chandra* effective area is higher at softer energies, the fact that no photons are detected with energies <4 keV suggests that this source is subject to high levels of absorption.

signals that could clearly be attributed to the *NuSTAR* sources due to the artifacts introduced by *NuSTAR*'s orbital occultations to the Fourier power spectrum.

5.5. Chandra Follow-Up of NuSTAR Discoveries

As discussed in Section 2, we triggered *Chandra* follow-up observations for the four sources discovered by *NuSTAR*: NNR 10, 19, 20, and 25. NNR 10, 19, and 25 were not detected by NARCS despite its much higher sensitivity compared to the *NuSTAR* Norma survey, indicating that these are transient sources. NNR 20 falls outside the area surveyed by *Chandra*, but our follow-up *Chandra* observations show that its flux is also highly variable.

The analysis of the *Chandra* follow-up of NNR 10 is presented in T14, while the analysis of the other three observations, which are listed in Table 3, is described here. The archival *Chandra* observation 7591 (see Table 2, which provides additional coverage of NNR 19) was also subjected to the same analysis. The *Chandra* observations were processed using CIAO version 4.7 adopting standard procedures. Then, we used `wavdetect` to determine the positions of the *Chandra* sources in the vicinity of the *NuSTAR* sources. The statistical uncertainties of the *Chandra* positions were calculated using the parameterization in Equation (5) of Hong et al. (2005); the 90% statistical uncertainty was then combined with *Chandra*'s $0\rlap{.}''64$ systematic uncertainty[24] in quadrature. Since NNR 19 was also detected in an archival *Chandra* observation, we averaged the positions determined from ObsIDs 7591 and 16170. The *Chandra* positions and uncertainties are reported in Table 8. The *Chandra* follow-up observations of NNR 19, 20, and 25 are shown in Figure 6, where green circles indicate the *NuSTAR* source positions and magenta circles show the locations of the nearest *Chandra* sources.

The closest *Chandra* source to NNR 19 is located at a distance of $13\rlap{.}''2$, which is outside of the 90% confidence *NuSTAR* error circle. However, as noted in Table 5, a few of the NARCS counterparts have similarly large offsets, suggesting that in some cases the systematic *NuSTAR* positional uncertainties may be underestimated. The fact that only 3 days elapsed between the *NuSTAR* and *Chandra* observations of NNR 19 strengthens the case that these sources are indeed associated. Furthermore, this *Chandra* source was detected in 2007 in *Chandra* ObsID 7591 but undetected in 2011 in ObsID 12508; the fact that this *Chandra* source is a transient boosts the probability that it is the counterpart of NNR 19.

The only *Chandra* source in the vicinity of NNR 20 lies within the *NuSTAR* error circle but is only detected at 2.9σ confidence. NNR 20 was not covered by previous *Chandra* observations, including NARCS; thus, before our follow-up observation (ObsID 16171), we did not know whether this source was a transient. Based on its *NuSTAR* 3–10 keV flux, we would have expected to detect at least 10 counts from its *Chandra* counterpart if it was persistent. Thus, even if it is not definite that the weak *Chandra* detection is truly the counterpart of NNR 20, the lack of any brighter *Chandra* sources proves that NNR 20 is a variable source.

Follow-up observations of NNR 25 were performed 34 days after the *NuSTAR* observations, and a *Chandra* source is clearly detected within the *NuSTAR* error circle. This *Chandra* source was not detected during the 2011 NARCS observations; its transient nature boosts the probability that it is the true counterpart of the transient NNR 25. As was done by F14 for all of the NARCS sources, we searched for infrared counterparts to the *NuSTAR*-discovered sources in the VVV survey. We did not find any infrared counterparts to NNR 19, 20, or 25 within the 95% uncertainty of the *Chandra*-derived positions.

In order to extract photometric and spectral information for each *Chandra* counterpart, we defined source aperture regions as circles with $2\rlap{.}''5$ radii and background regions as annuli with $15''$ inner radii and $44''$ outer radii. As the counterpart of NNR 19 was at a larger angular offset from the *Chandra* aimpoint in ObsID 7591, and the *Chandra* PSF increases in size with angular offset, the circular source region used for this observation had a $5''$ radius. For each source in each *Chandra* observation, we calculated the net 0.5–10 keV counts, detection significance, and quantile values (see Section 5.6), which are provided in Table 8.

5.6. Hardness Ratio and Quantile Analysis

Since spectral fitting can be unreliable or impractical for faint sources, we used hardness ratios and quantile values (Hong et al. 2004) to probe and compare the spectral properties of the *NuSTAR* sources. In order to reduce the level of background contamination and prevent the hardness ratios and quantile values from being skewed toward the values of the *NuSTAR* background, we opted to use the aperture regions with smaller radii to derive these spectral parameters. The hardness ratio for each source is calculated as $(H - S)/(H + S)$, where H is the counts in the hard (10–20 keV) band and S is the counts in the soft (3–10 keV) band. The *NuSTAR* hardness ratios are listed in Table 6.

---

[24] See http://cxc.harvard.edu/cal/ASPECT/celmon.
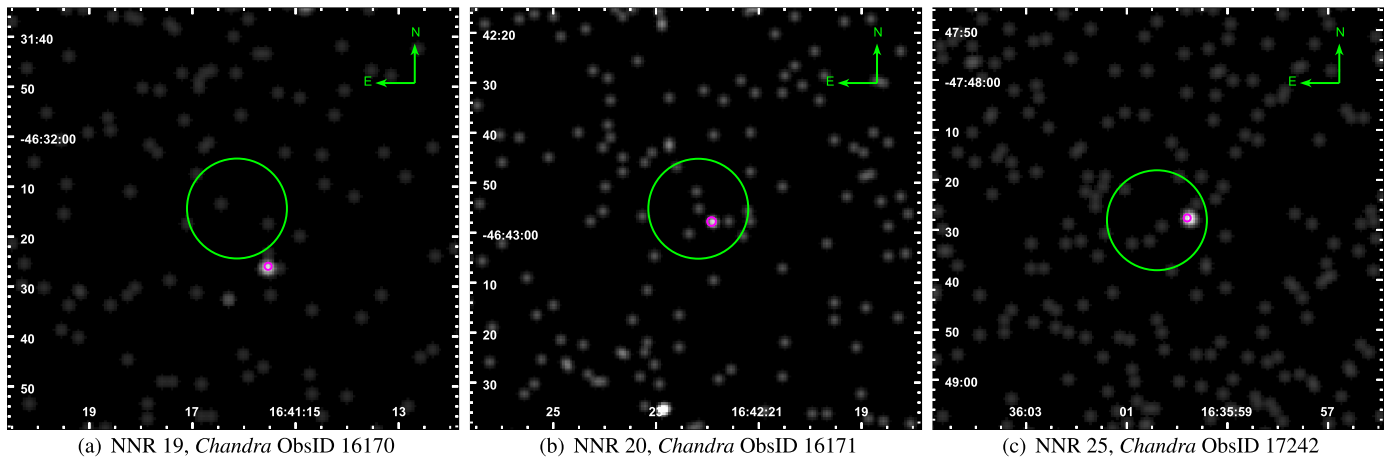
Figure 6. *Chandra* follow-up observations of *NuSTAR* transients in the 0.5–10 keV band (see Table 3). *NuSTAR* source positions are shown with 90% confidence error circles in green, and the locations of the nearest *Chandra* sources are indicated with 90% confidence error circles in magenta. The *NuSTAR* and *Chandra* positional uncertainties are provided in Tables 5 and 8 and are approximately $10''$ and $0.''7$, respectively, for all three sources.

While hardness ratios are the most widely used proxy for spectral hardness of faint X-ray sources, they are subject to selection effects associated with having to choose two particular energy bands, and they do not yield meaningful information for sources that have zero net counts in one of the two energy bands. Therefore, we also calculated quantile values for each source in the 3–40 keV band; these values are the median energy (E_{50}) and the energies below which 25% and 75% of the source counts reside (E_{25} and E_{75}, respectively). The latter energies were combined into a single quantile ratio (QR), which is a measure of how broad or peaked the spectrum is and is defined as $QR = 3(E_{25} - E_{\min})/(E_{75} - E_{\min})$, where $E_{\min}$ is the lower bound of the energy band: 3 keV for *NuSTAR* and 0.5 keV for *Chandra*. The *NuSTAR* median energy and QR value of each source are provided in Table 6 and shown in Figure 7(a). The gridlines in the figure indicate where a source with a particular blackbody, bremsstrahlung, or power-law spectrum would fall in the *NuSTAR* quantile space. Gridlines that are roughly vertical represent different temperatures (kT) or photon indices (Γ), while roughly horizontal gridlines represent different values of the absorbing column density along the line of sight to the source ($N_{\rm H}$).

Figure 7(b) shows the quantile values of the *Chandra* counterparts of the *NuSTAR* sources in the 0.5–10 keV band. Most of these values are taken from the NARCS catalog (F14). The quantile values for the *Chandra* counterparts of NNR 19 and 25 were derived using the aperture regions described in Section 5.5; the values for NNR 19 derived from ObsIDs 7591 and 16170 were combined in a weighted average. The *Chandra* counterpart of NNR 20 only has 3 counts, which are too few for quantile analysis; however, all three photons have energies >4 keV, indicating that this source is subject to significant absorption because *Chandra*'s effective area peaks below 2 keV. Finally, we did not adopt the NARCS catalog quantile values for the extended sources because they were derived using aperture regions whose position and extent were determined by eye and that removed embedded point sources not distinguishable with *NuSTAR*. Therefore, we recalculated the quantile values for the extended sources using circular aperture regions with $45''$ radii centered on the *NuSTAR*-determined positions of NNR 8 and 21. These *Chandra* quantiles are weighted averages of the values derived from

ObsIDs 12528 and 12529[25] for the counterpart of NNR 8 and ObsIDs 12523 and 12526 for the counterpart of NNR 21.

As can be seen in Figure 7, the *Chandra* quantiles can easily differentiate between foreground sources and those subject to high levels of absorption due to gas along the line of sight. The integrated column density of neutral and molecular hydrogen due to the interstellar medium along the line of sight in the Norma region varies from 4 to 9×10^{22} cm^{-2}, as derived from the sum of $N_{\rm HI}$ measured by the Leiden/Argentine/Bonn survey (Kalberla et al. 2005) and $N_{\rm H_2}$ estimated from the Millimeter-Wave Telescope CO survey (Bronfman et al. 1989) using the $N_{\rm H_2}/I_{\rm CO}$ factor from Dame et al. (2001). Since these surveys have $0.°5$ resolution, the interstellar $N_{\rm HI+H_2}$ values we derive are averages over 0.25 deg^2 regions, so it is possible that the interstellar absorption is actually higher or lower along particular lines of sight due to the clumpy nature of molecular clouds. Thus, the sources whose X-ray spectra show column densities in excess of these values may be located behind dense molecular clouds or suffer from additional absorption due to gas or dust local to the X-ray source. The *NuSTAR* quantiles are not particularly sensitive to $N_{\rm H}$ but instead are able to separate sources with intrinsically soft and hard spectra, regardless of their level of absorption. Thus, the combination of quantile values in the *Chandra* and *NuSTAR* bands allows us to learn a fair amount about the spectral properties of sources that are too faint for spectral fitting and provide a check on spectral fitting results that can depend on the choice of binning for low photon statistics.

5.7. Spectral Analysis

For all tier 1 sources with >100 net counts in the $40''$ radius aperture in the 3–40 keV band, we performed spectral analysis using XSPEC version 12.8.2 (Arnaud 1996), jointly fitting the *NuSTAR* and *Chandra* data when it was available. All spectral parameters were tied together for these joint fits, except for a

---

[25] The *Chandra* counterpart of NNR 8 is also observed in ObsID 12525. However, in this observation, a nearby transient point source that falls within the aperture region is visible. Comparing the 3–10 keV photon fluxes of NNR 8 in *Chandra* and *NuSTAR*, it does not appear that this nearby transient was present during the *NuSTAR* observation, and therefore we decided not to include ObsID 12525 in our *Chandra* analysis.

(a) *NuSTAR* quantile diagram.

(b) *Chandra* quantile diagram.
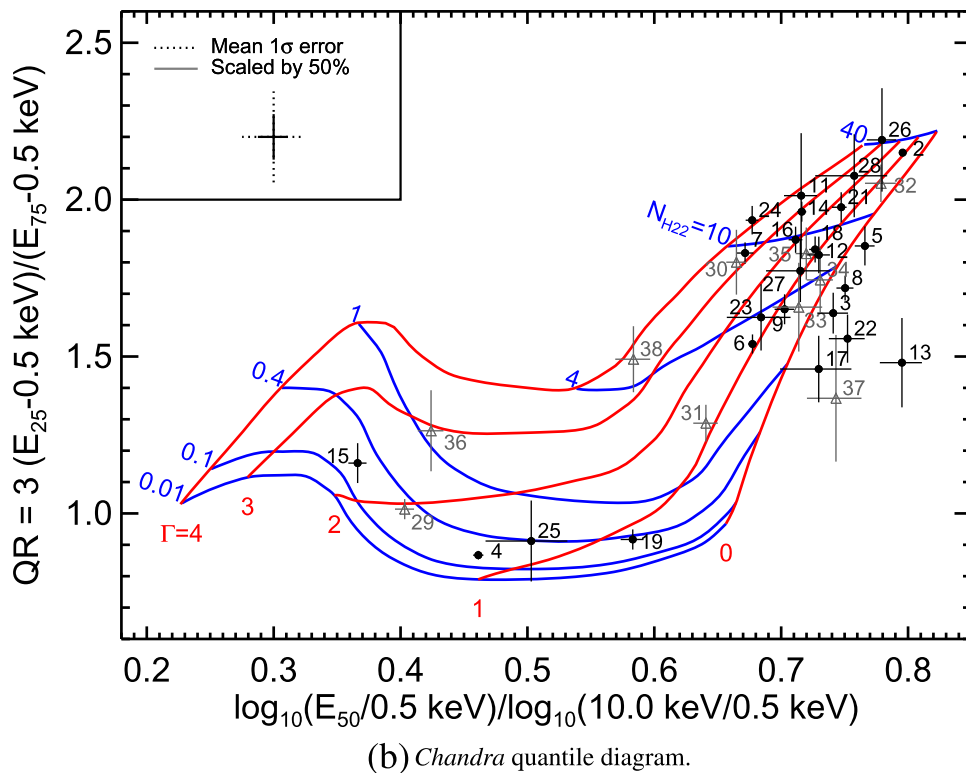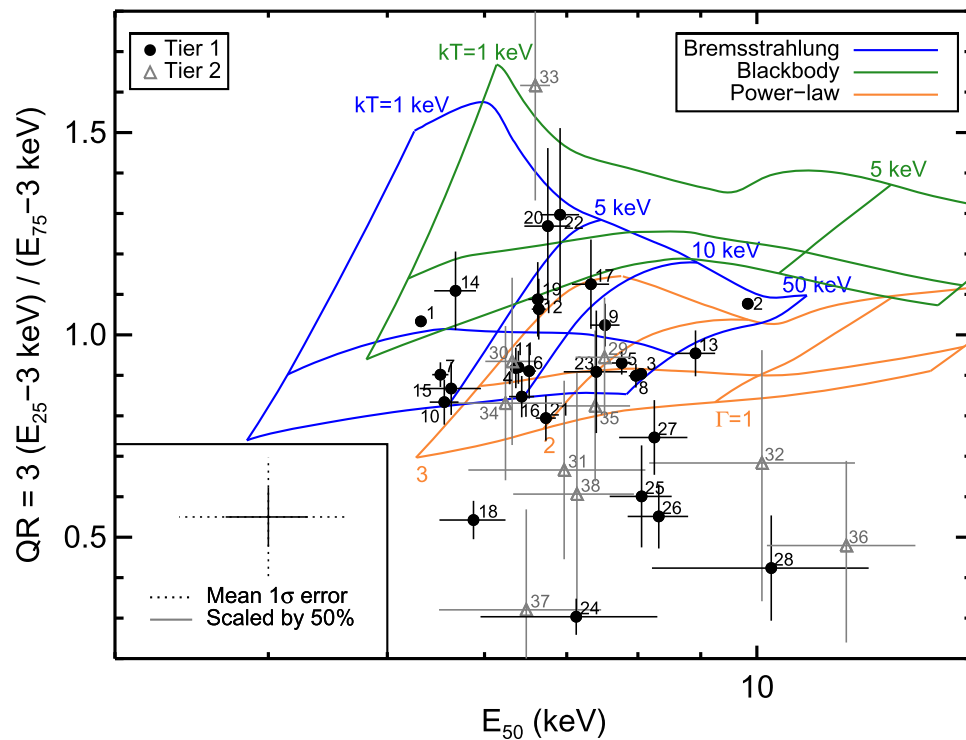
Figure 7. Quantile diagrams showing the quantile ratio on the *y*-axis and the median energy on the *x*-axis (or median energy "normalized" by the *Chandra* 0.5–10 keV band for panel (a)). Quantile values of tier 1 sources are shown with black circles, and those of tier 2 sources are shown with gray triangles. Comparing the positions of sources in the quantile diagrams to the spectral model gridlines provides a rough measurement of their spectral parameters. The *Chandra* quantiles are very sensitive to the amount of absorption suffered by a source, while the *NuSTAR* quantiles are more useful for separating sources with different spectral slopes. To improve the legibility of the plots, 1σ error bars have been scaled down by 50%. As a visual aide, the corner boxes in each plot show the mean 1σ uncertainty for the tier 1 sources and the same mean error scaled by 50%. (a) The *NuSTAR* 3–40 keV background has $E_{50} = 10$–15 keV and $QR = 0.4$–0.6, which is why several tier 2 sources, which are most affected by the background, are found near that position in the diagram. Grids representing absorbed bremsstrahlung, blackbody, and power-law models are shown in blue, green, and orange, respectively. Roughly vertical grid lines represent different values of the temperature (kT) or photon index (Γ). Primarily horizontal grid lines represent $N_H = 10^{22}$, 10^{23}, and 5×10^{23} cm^{-2} from bottom to top. (b) A grid of a power-law spectral model attenuated by interstellar absorption is overlaid. Red (primarily vertical) lines represent values of the photon index $\Gamma = 0, 1, 2, 3$, and 4 from right to left. Blue (primarily horizontal) lines represent values of the hydrogen column density $N_H = 0.01, 0.1, 0.4, 1, 4, 10$, and 40 in units of 10^{22} cm^{-2} from bottom to top.

cross-normalization factor between the *Chandra* and *NuSTAR* observations that was left as a free parameter to account for source variability and differences in instrumental calibrations (measured to be consistent to 10% precision; Madsen et al. 2015). We also included a cross-normalization constant between *NuSTAR* FPMA and FPMB in our models; for most sources, due to limited photon statistics, the errors on this normalization constant are large, and the constant is consistent with 1.0 to better than 90% confidence. Thus, for the *NuSTAR* sources detected with lowest significance (i.e., with trial map values $<10^{15}$), we fixed the FPMA/FPMB normalization constant to 1. To maximize the number of counts per spectral bin, we used the larger aperture source regions to extract information for spectral fitting; however, for NNR 22 and 27, which are only separated by $47''$, we extracted spectral information from $30''$ source regions to limit the blending of the two sources. The spectra of the *Chandra* counterparts were extracted as described in F14 for the NARCS sources and Section 5.5 for the counterparts of the *NuSTAR* discoveries; however, for the extended counterparts of NNR 8 and 21, we defined the aperture regions as $60''$ radius circles centered on the *NuSTAR*-derived position in order to match the *NuSTAR* extraction region.

The *Chandra* and *NuSTAR* spectra were grouped into bins of >2–10σ confidence, depending on the net counts of each source. For the three brightest sources, which have been carefully analyzed in other papers, we adopted simplified versions of the best-fitting models found in King et al. (2014), B16, and G14 in order to easily measure their observed and unabsorbed fluxes in the 3–10 and 10–20 keV bands, which we used to calculate the log$N$–log$S$ distribution of our survey (Section 6.3). For the other tier 1 sources, we fitted absorbed power-law, bremsstrahlung, and collisionally ionized models; we employed the `tbabs` absorption model with solar abundances from Wilms et al. (2000) and photoionization cross-sections from Verner et al. (1996). When Fe line emission was clearly visible between 6.4 and 7.1 keV, we also included a Gaussian line in the spectral models. Due to *NuSTAR*'s 0.4 keV resolution at 6–7 keV energies, multiple Fe lines would appear blended in our spectra, especially given the low photon statistics. Thus, measurements of the Fe line parameters should be interpreted as the average energy of the Fe line complex and the combined equivalent width of the Fe lines. If Fe line emission was not evident, the source spectrum was first fit without a Gaussian component. Then, having determined which of the three spectral models best fit the spectrum, a Gaussian component was added in order to place constraints on the strength of Fe line emission that may not be visible due to poor photon statistics. The central energy of this Gaussian component was constrained to be between 6.3 and 7.1 keV, and its width was fixed to zero; we tested the effect of fixing the width to values as high as 0.1 keV, but the impact on the results was negligible. Then, the 90% upper limit on the line normalization was used to calculate the 90% upper limit on the Fe line equivalent width. In addition, when significant residuals remained at soft energies, we introduced a partial covering model (`pcfabs`) to test whether it provided a significant improvement of the χ^2 statistic. Including this component substantially improved χ^2 for NNR 4 and 6;

however, for NNR 6, the N_H of the partial absorber could not be well constrained, and the covering fraction was found to be consistent with 1.0 to 90% confidence. Thus, since the spectral quality of NNR 6 was not good enough to constrain the additional `pcfabs` component, we did not include it in our final model fit for NNR 6.

The results of our spectral analysis can be found in Table 9, and the spectra and fit residuals are shown in Figure 8 and the Appendix. As can be seen, spectra with <300 *NuSTAR* counts cannot place strong constraints on the spectral parameters. However, we nonetheless include these results in order to be able to compare nonparametric fluxes with spectrally derived fluxes and as a reference to aid the design of future *NuSTAR* surveys.

We used the model fit with the best reduced χ^2 statistic to determine observed energy fluxes for each source in the 2–10, 3–10, and 10–20 keV bands and conversion factors from photon fluxes to unabsorbed energy fluxes, which are listed in Table 10. These conversion factors are used to calculate the log$N$–log$S$ distribution for unabsorbed fluxes (see Section 6.3). The faintest tier 1 source, NNR 28, does not have enough counts to permit spectral fitting; based on its quantile values, it has $N_H \approx 10^{23}\,\mathrm{cm}^{-2}$ and $\Gamma \approx 1.8$. Fixing the parameters of an absorbed power-law model to these values while allowing the *Chandra* and *NuSTAR* normalizations to vary independently, we fit the unbinned spectra of NNR 28 using the C-statistic (Cash 1979) and find a goodness of fit lower than 28%. The observed and unabsorbed fluxes of NNR 28 measured from these fits are included in Table 10.

To ensure that these results were not significantly dependent on the binning that was chosen, we compared the best-fitting parameters with those derived by fitting unbinned spectra using the C-statistic and the locations of sources in the quantile diagrams. No significant discrepancies were found except for sources with strong Fe lines, which is to be expected, since the quantile grids do not account for the presence of Fe lines. However, for NNR 17, our analysis yielded a harder spectrum than that found by B14. This source lies in the ghost ray pattern of 4U 1630–472, making background subtraction particularly challenging. The background region we selected contains higher ghost ray contamination than the background chosen by B14; we consider our selection more appropriate, given that this source resides in a region of high ghost ray contamination. Since the spectrum of 4U 1630–472 is dominated by a blackbody component with $kT \approx 1.4$ keV, the fact that B14 measured a softer spectrum for NNR 17 than we did, with $\Gamma = 3.7 \pm 0.5$ rather than $2.0^{+1.0}_{-0.8}$, suggests that the background contribution from ghost rays may have been underestimated by B14. The photon index we measured is also more consistent with the hard photon index indicated by the *Chandra* quantiles (see Figure 7(b)).

6. Discussion

6.1. Classification of NuSTAR Sources

The X-ray spectral and timing properties of the *NuSTAR* sources, as well as information about their optical and infrared counterparts, can help identify their physical nature. The three brightest sources in the *NuSTAR* Norma survey are well

Table 9
Spectral Fits

Src No. (1)	Model tbabs∗X (2)	N/C norm (3)	FPMA/B norm (4)	N_H (10^{22} cm^{-2}) (5)	Γ (6)	E_{cut} (keV) (7)	Power-law norm (8)	kT_{BB} (keV) (9)	Bbody norm (10)	χ^2_ν/dof (11)	Bin (σ) (12)	(13) Comments
1	*PL +diskbb*	⋯	$0.978^{+0.01}_{-0.02}$	12.47 ± 0.08	2.15 ± 0.03	⋯	0.22 ± 0.02	$1.425^{+0.002}_{-0.003}$	192 ± 2	2.68/806	10	See King et al. (2014) for fit including disk reflection and wind absorption.
2	*cutoffpl +bbodyrad*	$0.67^{+0.02}_{-0.01}$	$1.02^{+0.03}_{-0.02}$	46.0 ± 1.5	$-2.5^{+0.4}_{-0.5}$	$4.05^{+0.33}_{-0.06}$	$1.3^{+1.5}_{-0.1} \times 10^{-5}$	$1.56^{+0.06}_{-0.08}$	$0.75^{+0.12}_{-0.08}$	1.14/1096	5, 5	See Bodaghee et al. (2016) for fit including cyclotron absorption line.

Src No.	Model tbabs∗X	N/C norm	FPMA/B norm	N_H (10^{22} cm^{-2})	Γ or kT(keV) (14)	Norm (10^{-5}) (15)	Line En. (keV) (16)	Line Equation (keV) (17)	Line norm (10^{-6}) (18)	χ^2_ν/dof	Bin (σ)	Comments
3	*PL*	$3.4^{+1.0}_{-0.7}$	$1.04^{+0.04}_{-0.03}$	12 ± 2	1.71 ± 0.06	$6.7^{+1.0}_{-0.6}$	⋯	⋯	⋯	1.02/263	3, 5	*Chandra* only includes the point source, while *NuSTAR* includes extended emission. See Gotthelf et al. (2014) for detailed analysis.
4	*PCA∗(PL+G)*	$0.59^{+0.10}_{-0.09}$	$0.92^{+0.15}_{-0.13}$	$0.35^{+0.11}_{-0.10}$	2.34 ± 0.22	56^{+26}_{-17}	$6.65^{+0.10}_{-0.06}$	$0.9^{+0.2}_{-0.1}$	$6.2^{+2.4}_{-1.9}$	1.19/154	3, 3	pcfabs reduces χ^2_ν by ≈ 0.2. For PL, $N_{H,cvr} = 6^{+2}_{-1} \times 10^{22}$ cm^{-2}, cvrf = $0.77^{+0.06}_{-0.08}$. For BR and AP, $N_{H,cvr} = 5 \pm 2 \times 10^{22}$ cm^{-2}, cvrf = 0.5 ± 0.1.
	PCA∗(BR+G)	$0.57^{+0.09}_{-0.08}$	$0.90^{+0.15}_{-0.12}$	0.14 ± 0.08	$7.9^{+2.4}_{-1.7}$	24^{+4}_{-3}	$6.65^{+0.09}_{-0.06}$	0.8 ± 0.2	$5.6^{+2.1}_{-1.8}$	1.20/154	3, 3	⋯
	PCA∗(AP+G)	$0.56^{+0.04}_{-0.08}$	$0.90^{+0.16}_{-0.12}$	$0.13^{+0.09}_{-0.08}$	$7.4^{+2.1}_{-1.5}$	68^{+11}_{-9}	$6.56^{+0.12}_{-0.17}$	0.2 ± 0.1	$2.1^{+2.2}_{-1.6}$	1.19/154	3, 3	⋯
5	*PL*	$1.3^{+0.5}_{-0.3}$	$0.9^{+0.3}_{-0.2}$	27^{+10}_{-8}	2.3 ± 0.3	28^{+40}_{-16}	6.3–7.1	<0.36	<1.3	1.07/47	3, 3	⋯
	BR	$1.3^{+0.5}_{-0.3}$	$0.9^{+0.3}_{-0.2}$	21^{+8}_{-6}	10^{+5}_{-3}	9^{+5}_{-3}	⋯	⋯	⋯	1.07/47	3, 3	⋯
	AP	$1.2^{+0.5}_{-0.3}$	$0.9^{+0.3}_{-0.2}$	17^{+6}_{-5}	13^{+5}_{-3}	21^{+8}_{-7}	⋯	⋯	⋯	1.15/47	3, 3	⋯
6	PL+G	1.0 ± 0.2	$0.9^{+0.3}_{-0.2}$	5 ± 1	1.5 ± 0.3	13^{+7}_{-4}	$6.5^{+0.3}_{-1.7}$	1.5 ± 0.5	11^{+62}_{-5}	1.79/27	5, 3	⋯
	BR+G	$1.0^{+0.3}_{-0.2}$	0.98 ± 0.25	$4.3^{+0.9}_{-1.5}$	>15	18^{+3}_{-2}	$6.5^{+0.4}_{-0.3}$	1.3 ± 0.4	10^{+7}_{-5}	1.72/27	5, 3	⋯
	AP+G	1.0 ± 0.2	$1.0^{+0.3}_{-0.2}$	$4.3^{+0.9}_{-0.7}$	>15	51^{+9}_{-3}	6.4 ± 0.4	1.2 ± 0.5	9^{+6}_{-5}	1.69/27	5, 3	⋯
7	PL+G	1.0 ± 0.2	$0.8^{+0.2}_{-0.1}$	15^{+3}_{-2}	$3.4^{+0.4}_{-0.3}$	220^{+80}_{-90}	6.76 ± 0.12	0.65 ± 0.20	$2.1^{+1.1}_{-0.9}$	0.92/75	2.5, 2.5	apec abundance = 0.5 ± 0.3. NARCS 1278 flux is 30% of total (Rahoui et al. 2014).
	BR+G	1.0 ± 0.2	$0.9^{+0.2}_{-0.1}$	11^{+2}_{-1}	$3.4^{+0.7}_{-0.6}$	32^{+6}_{-7}	6.76 ± 0.12	0.5 ± 0.2	$1.8^{+1.1}_{-0.9}$	0.93/75	2.5, 2.5	⋯
	AP	1.0 ± 0.2	$0.9^{+0.2}_{-0.1}$	11 ± 2	$3.2^{+0.8}_{-0.5}$	100^{+30}_{-25}	⋯	⋯	⋯	0.89/77	2.5, 2.5	⋯
8	*PL*	1.0 ± 0.2	⋯	14^{+7}_{-8}	1.8 ± 0.2	18^{+15}_{-8}	6.3–7.1	<0.26	<1.9	1.01/27	3, 5	Only FPMA used.
	BR	1.0 ± 0.2	⋯	12^{+5}_{-4}	25^{+22}_{-9}	15^{+5}_{-4}	⋯	⋯	⋯	1.03/27	3, 5	⋯
	AP	1.0 ± 0.2	⋯	10^{+4}_{-3}	>21	44^{+11}_{-10}	⋯	⋯	⋯	1.14/27	3, 5	⋯
9	PL+G	$0.9^{+0.3}_{-0.2}$	$0.9^{+0.3}_{-0.2}$	7^{+3}_{-2}	1.5 ± 0.3	9^{+7}_{-4}	6.5 ± 1.2	0.6 ± 0.4	3^{+25}_{-2}	0.84/29	3, 2.5	⋯
	BR+G	$0.9^{+0.3}_{-0.2}$	$0.9^{+0.3}_{-0.2}$	7^{+2}_{-1}	>15	11^{+6}_{-2}	$6.4^{+0.7}_{-0.3}$	0.5 ± 0.3	3^{+8}_{-2}	0.83/29	3, 2.5	⋯
	AP+G	$0.8^{+0.3}_{-0.2}$	0.9 ± 0.2	7^{+2}_{-1}	>15	33^{+8}_{-3}	$6.4^{+0.5}_{-0.4}$	0.4 ± 0.2	$2.2^{+2.7}_{-1.7}$	0.82/29	3, 2.5	⋯
10	*PL*	⋯	$0.9^{+0.6}_{-0.3}$	28	$4.1^{+0.9}_{-0.8}$	1800^{+6400}_{-1400}	6.3–7.1	<0.61	<4.2	1.09/10	2	N_H set to values from Jakobsen et al. (2014).
	BR	⋯	$0.9^{+0.6}_{-0.3}$	17	3^{+2}_{-1}	70^{+100}_{-40}	⋯	⋯	⋯	1.14/10	2	⋯
	AP	⋯	$0.9^{+0.6}_{-0.4}$	17	$1.9^{+5.0}_{-0.7}$	330^{+800}_{-290}	⋯	⋯	⋯	1.77/10	2	⋯
11	*PL*	5^{+7}_{-2}	$1.3^{+0.9}_{-0.8}$	11^{+11}_{-9}	2.3 ± 0.4	$2.4^{+6.1}_{-2.0}$	⋯	⋯	⋯	1.32/42	3, 3	⋯
	BR	6^{+21}_{-3}	$1.3^{+1.1}_{-1.0}$	<14	10^{+6}_{-3}	$0.7^{+0.9}_{-0.6}$	6.3–7.1	<0.35	<0.1	1.27/42	3, 3	⋯
	AP	17^{+15}_{-12}	$1.4^{+3.4}_{-0.6}$	<5	14^{+5}_{-3}	$0.6^{+1.6}_{-0.3}$	⋯	⋯	⋯	1.33/42	3, 3	⋯

Table 9
(Continued)

Src No.	Model tbabs*X	N/C norm	FPMA/B norm	N_H $(10^{22}\,cm^{-2})$	Γ or kT(keV) (14)	Norm (10^{-5}) (15)	Line En. (keV) (16)	Line Equation (keV) (17)	Line norm (10^{-6}) (18)	χ^2_ν/dof	Bin (σ)	Comments
12	PL+G	$1.1^{+0.5}_{-0.3}$	$1.0^{+0.4}_{-0.3}$	20^{+9}_{-6}	2.4 ± 0.5	14^{+26}_{-9}	$6.78^{+0.14}_{-0.12}$	1.2 ± 0.4	$1.7^{+1.2}_{-0.8}$	1.14/33	2.5, 2.5	...
	BR+G	$1.0^{+0.5}_{-0.3}$	$1.0^{+0.4}_{-0.3}$	16^{+7}_{-5}	9^{+8}_{-3}	5 ± 2	$6.77^{+0.13}_{-0.12}$	$1.2^{+0.5}_{-0.3}$	$1.6^{+1.2}_{-0.8}$	1.17/33	2.5, 2.5	...
	AP	$1.1^{+0.5}_{-0.3}$	$1.0^{+0.4}_{-0.3}$	19^{+7}_{-5}	6^{+3}_{-1}	17^{+8}_{-6}	...	...	...	1.21/36	2.5, 2.5	...
13	PL	$1.5^{+1.1}_{-0.6}$	$1.0^{+0.7}_{-0.4}$	9^{+17}_{-6}	1.0 ± 0.5	$0.7^{+1.8}_{-0.5}$	6.3–7.1	<2.7	<3.4	1.22/23	2, 2	...
	BR	$1.6^{+1.1}_{-0.6}$	$1.0^{+0.7}_{-0.4}$	11^{+11}_{-6}	>31	$2.9^{+2.2}_{-0.4}$	...	...	...	1.25/23	2, 2	...
	AP	1.6 ± 0.7	$1.0^{+0.7}_{-0.4}$	13^{+24}_{-7}	>21	7^{+1}_{-3}	...	...	...	1.28/23	2, 2	...
14	PL+G	$0.7^{+0.2}_{-0.1}$	...	29^{+9}_{-7}	$4.1^{+1.2}_{-0.9}$	760^{+5700}_{-610}	$6.59^{+0.08}_{-0.06}$	1.8 ± 0.5	6^{+3}_{-2}	1.07/28	3, 2.5	Only FPMB used.
	BR+G	$0.7^{+0.2}_{-0.1}$	...	22^{+7}_{-5}	$2.4^{+1.4}_{-0.9}$	60^{+130}_{-30}	$6.59^{+0.10}_{-0.06}$	$1.7^{+0.6}_{-0.4}$	5^{+3}_{-2}	1.08/28	3, 2.5	...
	AP	0.8 ± 0.2	...	25^{+7}_{-5}	$2.1^{+0.9}_{-0.5}$	190^{+240}_{-90}	...	...	...	1.11/31	3, 2.5	...
15	PL	$1.9^{+1.4}_{-0.8}$	$0.7^{+0.4}_{-0.3}$	<0.4	2.6 ± 0.4	13^{+6}_{-4}	6.3–7.1	<1.7	<2.1	0.75/20	3, 2	...
	BR	$1.8^{+1.1}_{-0.8}$	$0.6^{+0.3}_{-0.2}$	<0.08	$2.9^{+1.0}_{-0.7}$	11 ± 2	...	...	...	0.90/20	3, 2	...
	AP	$1.8^{+1.1}_{-0.8}$	$0.6^{+0.3}_{-0.2}$	<0.10	$2.9^{+0.8}_{-0.7}$	28^{+9}_{-7}	...	...	...	0.82/19	3, 2	...
16	PL	$1.6^{+0.7}_{-0.5}$	$0.7^{+0.3}_{-0.2}$	19^{+6}_{-5}	$2.9^{+0.6}_{-0.5}$	130^{+240}_{-80}	...	...	...	1.05/24	3, 2.5	Harder spectrum than that found by Bodaghee et al. (2014) due to different background regions.
	BR	$1.6^{+0.6}_{-0.5}$	$0.7^{+0.3}_{-0.2}$	14^{+4}_{-3}	5^{+3}_{-1}	25^{+14}_{-8}	6.3–7.1	<0.8	<4.8	0.95/24	3, 2.5	...
	AP	$1.2^{+0.5}_{-0.4}$	0.7 ± 0.2	13 ± 3	6^{+4}_{-2}	58^{+27}_{-15}	...	...	...	1.06/24	3, 2.5	...
17	PL	$1.1^{+1.2}_{-0.5}$	$0.8^{+0.6}_{-0.4}$	21^{+32}_{-16}	$2.0^{+1.0}_{-0.8}$	6^{+65}_{-5}	6.3–7.1	<1.0	<1.3	0.94/13	2, 2	...
	BR	$1.1^{+1.3}_{-0.5}$	$0.8^{+0.6}_{-0.4}$	16^{+24}_{-12}	>6	3^{+6}_{-2}	...	...	...	0.95/13	2, 2	...
	AP	$1.1^{+1.3}_{-0.5}$	$0.8^{+0.6}_{-0.4}$	14^{+17}_{-10}	>8	9^{+9}_{-5}	...	...	...	0.94/13	2, 2	...
18	PL	$1.1^{+0.6}_{-0.5}$	$0.8^{+0.7}_{-0.4}$	19^{+9}_{-6}	$2.6^{+1.0}_{-0.8}$	50^{+260}_{-40}	...	...	...	1.87/13	3, 2	...
	BR	$1.1^{+0.6}_{-0.4}$	$0.8^{+0.7}_{-0.4}$	16^{+7}_{-3}	6^{+11}_{-3}	16^{+19}_{-8}	6.3–7.1	<0.9	<3	1.81/13	3, 2	...
	AP	$1.0^{+0.5}_{-0.4}$	$0.8^{+0.8}_{-0.4}$	13^{+7}_{-3}	9^{+24}_{-6}	33^{+51}_{-8}	...	...	...	1.97/13	3, 2	...
19	PL	1.0 ± 0.3	$1.2^{+0.6}_{-0.4}$	$1.7^{+0.8}_{-0.6}$	$1.7^{+0.3}_{-0.4}$	4 ± 2	...	...	...	1.66/25	3, 3	$N/C = 0.8^{+0.3}_{-0.2}$ for *Chandra* ObsID 7591.
	BR	$1.0^{+0.4}_{-0.2}$	$1.1^{+0.6}_{-0.3}$	$1.4^{+0.5}_{-0.4}$	13^{+18}_{-5}	$4.0^{+0.8}_{-0.6}$	...	...	...	1.44/25	3, 3	...
	AP	1.0 ± 0.3	$1.1^{+0.6}_{-0.3}$	$1.4^{+0.5}_{-0.4}$	11^{+18}_{-4}	12 ± 2	6.3–7.1	<1.3	<2.4	1.44/25	3, 3	...
20	PL	1	1	70^{+130}_{-50}	$2.6^{+2.1}_{-1.4}$	52^{+15000}_{-50}	6.3–7.1	<0.6	<6.4	1.26/11	2, 2	If the cross-normalization constant between *Chandra* and *NuSTAR* is left as a free parameter, $N/C > 2$ at 90% confidence.
	BR	1	1	60^{+90}_{-40}	>3	8^{+80}_{-5}	...	...	...	1.31/11	2, 2	...
	AP	1	1	50^{+50}_{-30}	>6	18^{+27}_{-8}	...	...	...	1.30/11	2, 2	...
21	PL	0.9 ± 0.2	...	26^{+9}_{-7}	$2.6^{+0.5}_{-0.4}$	120^{+200}_{-70}	6.3–7.1	<0.5	<4.6	1.01/47	3, 3	Only FPMB used. Point-source (NARCS 402) flux is 20% ± 5% of total.
	BR	0.9 ± 0.2	...	20^{+7}_{-5}	8^{+5}_{-2}	31^{+15}_{-9}	...	...	...	1.04/47	3, 3	...
	AP	0.8 ± 0.2	...	17^{+5}_{-4}	10^{+7}_{-3}	71^{+22}_{-16}	...	...	...	1.13/47	3, 3	...
22	PL	$1.7^{+1.5}_{-0.8}$	1	13^{+12}_{-7}	$2.0^{+1.3}_{-1.2}$	$5.1^{+41}_{-4.4}$	...	...	...	1.92/10	2, 2	...
	BR	$1.6^{+1.4}_{-0.8}$	1	11^{+10}_{-5}	>4	3^{+6}_{-1}	...	...	...	1.91/10	2, 2	...
	AP	$1.8^{+1.3}_{-0.7}$	1	13^{+13}_{-5}	5^{+23}_{-3}	12^{+24}_{-6}	6.3–7.1	<3.8	<4.4	1.67/10	2, 2	...
23	PL	$1.7^{+2.1}_{-0.9}$	1	7^{+65}_{-5}	$1.8^{+2.0}_{-0.8}$	$1.6^{+340}_{-1.3}$	...	...	...	0.83/6	2, 2	...

Table 9
(Continued)

Src No.	Model tbabs*X	N/C norm	FPMA/B norm	N_H (10^{22} cm^{-2})	Γ or kT(keV) (14)	Norm (10^{-5}) (15)	Line En. (keV) (16)	Line Equation (keV) (17)	Line norm (10^{-6}) (18)	χ^2_ν/dof	Bin (σ)	Comments
	BR	$1.7^{+2.0}_{-0.9}$	1	6^{+49}_{-4}	>4	$1.5^{+14.5}_{-0.9}$	...	...	...	0.75/6	2, 2	...
	AP	$1.7^{+2.0}_{-0.9}$	1	7^{+29}_{-5}	>5	$4.6^{+13}_{-2.6}$	6.3–7.1	<3.9	<2.9	0.64/6	2, 2	...
24	PL	0.7 ± 0.3	1	28^{+12}_{-8}	$5.0^{+2.2}_{-1.4}$	1180^{+41220}_{-1070}	6.3–7.1	<16	<6.2	1.25/23	2, 2	...
	BR	0.7 ± 0.3	1	20^{+8}_{-6}	$1.7^{+1.3}_{-0.7}$	50^{+290}_{-30}	...	...	...	1.33/23	2, 2	...
	AP	0.7 ± 0.3	1	24^{+7}_{-6}	$1.4^{+0.8}_{-0.4}$	160^{+500}_{-110}	...	...	...	1.32/23	2, 2	...
25	PL	$1.3^{+1.3}_{-0.6}$	...	$3.1^{+3.8}_{-2.8}$	1.8 ± 0.7	$1.9^{+4.2}_{-1.5}$	...	...	...	1.14/8	2, 2	Only FPMA used.
	BR	$1.3^{+1.7}_{-0.6}$	...	$2.3^{+3.0}_{-2.2}$	>6	$1.7^{+1.1}_{-1.0}$	...	...	...	1.05/8	2, 2	...
	AP	$1.3^{+1.7}_{-0.6}$	...	$2.3^{+2.9}_{-2.1}$	>6	5 ± 3	6.3–7.1	<2.1	<1.8	1.02/8	2, 2	...
26	PL	$1.3^{+2.8}_{-0.7}$	1	30^{+35}_{-23}	$1.5^{+1.0}_{-0.9}$	$2.8^{+30}_{-2.5}$	6.3–7.1	<1.2	<1.9	1.57/10	2, 2	...
	BR	$1.3^{+2.6}_{-0.6}$	1	28^{+31}_{-21}	>9	$3.5^{+5.5}_{-2.5}$	...	...	...	1.58/10	2, 2	...
	AP	$1.3^{+2.5}_{-0.6}$	1	28^{+28}_{-19}	>13	11^{+12}_{-8}	...	...	...	1.59/10	2, 2	...
27	PL	$4.4^{+5.9}_{-3.5}$	1	<23	$0.9^{+0.8}_{-0.4}$	$0.18^{+2.68}_{-0.09}$	6.3–7.1	<1.1	<0.5	0.85/8	2, 2	...
	BR	$6.3^{+6.2}_{-5.2}$	1	<27	>23	$0.7^{+6.0}_{-0.3}$	...	...	...	0.95/8	2, 2	...
	AP	$7.4^{+10.2}_{-2.7}$	1	<34	>20	$1.4^{+13.8}_{-0.7}$	...	...	...	1.08/8	2, 2	...

Notes. Errors provided are 90% confidence intervals, except for errors on the line equivalent widths, which are 1σ confidence intervals. (2) For sources NNR 1–3, which have been analyzed in more detail in other papers, we present the results of simplified models used to derive the fluxes and conversion factors in Table 10. For all other sources, we present fits using power-law (PL), bremsstrahlung (BR), and collisionally ionized apec models (AP). Some models include a Gaussian line (G) or partial covering absorption (PCA). The best-fitting model for each source is written in italics. (3) Multiplicative constant included in all spectral models. The constant is set to 1.0 for *Chandra*, and, if enough spectral bins are available, it is allowed to vary independently for *NuSTAR* FPMA and FPMB. Here N/C provides the ratio of the *NuSTAR* FPMA constant relative to *Chandra*. (4) Ratio of the FPMA to FPMB fitting constants, providing the cross-calibration of the two *NuSTAR* modules. For sources with insufficient photon statistics, this ratio is set to 1.0. (11) Reduced χ^2 statistic and degrees of freedom for the best-fitting model. (12) Minimum significance of bins for *Chandra* and *NuSTAR* spectra. (16)–(18) Central energy, equivalent width, and normalization of a Gaussian model accounting for Fe line emission. In cases where a Fe line is clearly visible in the spectrum, a Gaussian line (G) is included in the model; otherwise, we provide the results of the best-fit models without a Gaussian line and an upper limit to the Fe line equivalent width derived by adding a Gaussian component as described in Section 5.7.
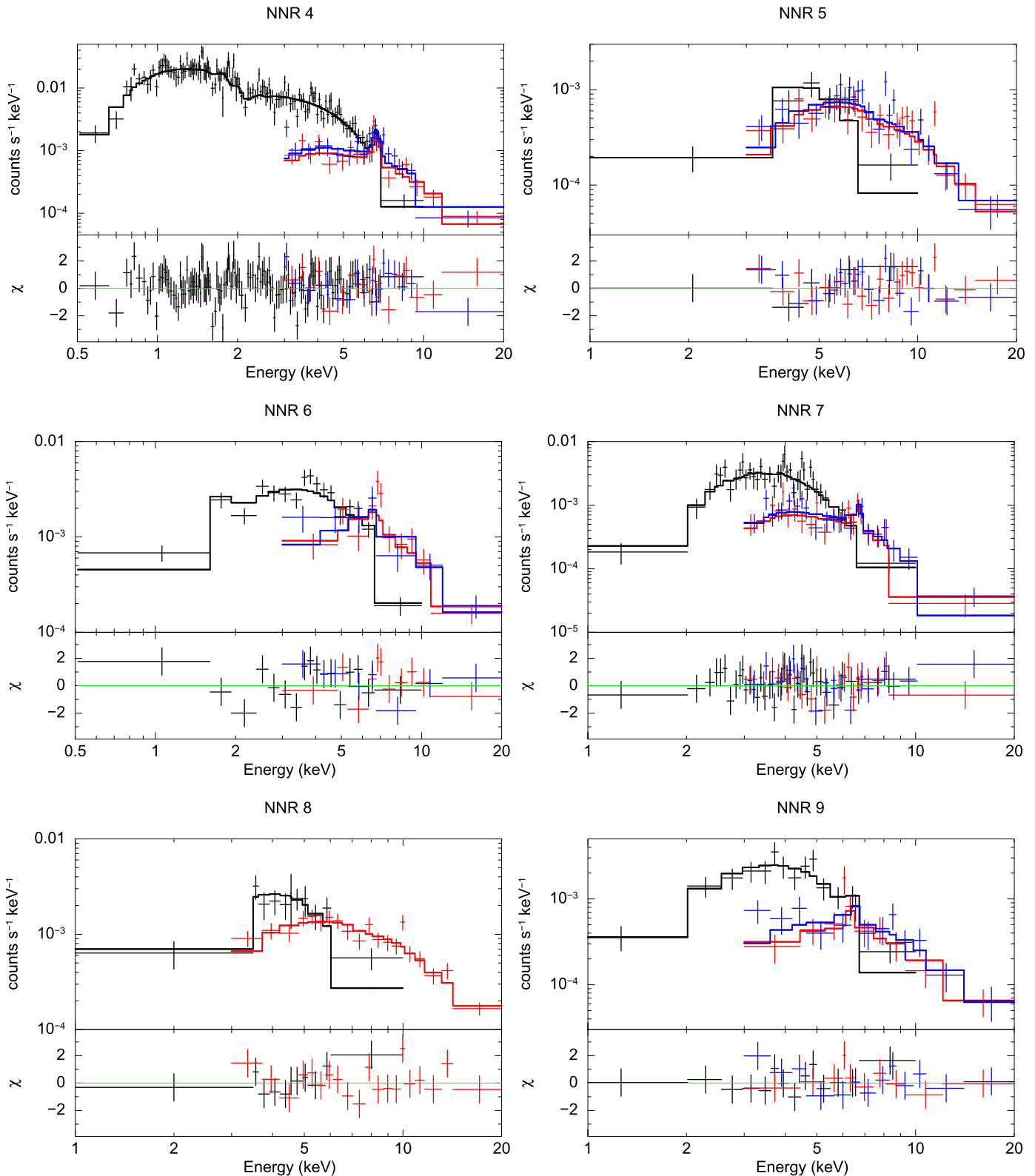
Figure 8. Example *Chandra* and *NuSTAR* spectra with residuals of the best-fitting models. *Chandra* data is shown in black, *NuSTAR* FPMA data are shown in red, and FPMB data are shown in blue. Additional spectra are shown in the Appendix. Spectral analysis results can be found in Table 9.

studied and classified: 4U 1630–472 (NNR 1) is a BH LMXB (e.g., Barret et al. 1996; Klein-Wolt et al. 2004), IGR J16393–4643 (NNR 2) is an NS HMXB (Bodaghee et al. 2006; B16), and HESS J1640–465 (NNR 3) is a

pulsar and associated pulsar wind nebula (PWN; G14; Archibald et al. 2016). Here we present the most likely classifications of the fainter *NuSTAR* sources and their hard X-ray properties.

Table 10
Spectrally Derived Fluxes

Src No. (1)	Ph. Flux (10^{-6} cm^{-2} s^{-1})			Abs. Flux (10^{-14} erg cm^{-2} s^{-1})			Ph. flux to unabs. flux (10^{-9} erg ph^{-1})		
	Chandra 2–10 keV (2)	NuSTAR 3–10 keV (3)	NuSTAR 10–20 keV (4)	Chandra 2–10 keV (5)	NuSTAR 3–10 keV (6)	NuSTAR 10–20 keV (7)	Chandra 2–10 keV (8)	NuSTAR 3–10 keV (9)	NuSTAR 10–20 keV (10)
1	···	614000 ± 300	19950^{+30}_{-50}	···	490300^{+200}_{-300}	39590^{+60}_{-100}	···	12.2	20.9
2	2200^{+200}_{-500}	1500^{+100}_{-300}	1700^{+500}_{-700}	2500^{+300}_{-600}	1700^{+200}_{-300}	4000^{+1000}_{-2000}	27.0	24.7	26.3
3	$19^{+0.2}_{-0.3}$	$56.0^{+0.3}_{-1.9}$	$22.8^{+0.1}_{-0.8}$	16 ± 2	$52.1^{+0.2}_{-1.8}$	$51.3^{+0.3}_{-1.9}$	14.4	12.6	23.4
4	101^{+3}_{-7}	43^{+1}_{-4}	$7.0^{+0.4}_{-0.7}$	71^{+2}_{-6}	36^{+1}_{-3}	$15.3^{+0.8}_{-1.6}$	9.3	9.7	22.3
5	16^{+2}_{-4}	$21.8^{+0.4}_{-3.6}$	$7.1^{+0.2}_{-1.4}$	15^{+1}_{-4}	$20.6^{+0.3}_{-3.4}$	$15.7^{+0.3}_{-3.0}$	26.5	19.0	24.1
6	82^{+3}_{-7}	68^{+4}_{-9}	21^{+2}_{-5}	68^{+3}_{-7}	63^{+3}_{-8}	47^{+4}_{-11}	9.9	10.2	22.7
7	42^{+1}_{-3}	36^{+1}_{-3}	$1.7^{+0.2}_{-0.4}$	32^{+1}_{-3}	$29.1^{+0.9}_{-2.5}$	$3.3^{+0.4}_{-0.8}$	14.3	11.7	20.7
8	43^{+3}_{-7}	$40.3^{+0.6}_{-6.4}$	$16.6^{+0.3}_{-2.6}$	39^{+3}_{-6}	$37.8^{+0.5}_{-5.8}$	$37.5^{+0.8}_{-6.0}$	15.7	13.4	23.5
9	43 ± 3	33^{+2}_{-3}	$12.5^{+0.9}_{-3}$	37 ± 3	31 ± 2	28 ± 2	11.2	10.9	22.9
10	···	55^{+3}_{-24}	$3.6^{+0.3}_{-2.1}$	···	44^{+2}_{-19}	$7.5^{+0.7}_{-4.4}$	···	23.2	23.0
11	$2.6^{+0.6}_{-1.1}$	$10.3^{+0.2}_{-4.1}$	$2.15^{+0.03}_{-0.98}$	$2.0^{+0.6}_{-0.9}$	$9.0^{+0.2}_{-3.5}$	$4.65^{+0.06}_{-2.13}$	9.8	10.0	22.0
12	$10.4^{+0.8}_{-3.9}$	$10.4^{+0.2}_{-3.1}$	$2.35^{+0.03}_{-0.8}$	9^{+2}_{-3}	$9.7^{+0.1}_{-2.8}$	$5.18^{+0.06}_{-1.70}$	20.7	15.6	23.5
13	$6.4^{+0.9}_{-2.8}$	$8.4^{+0.2}_{-3.4}$	$5.8^{+0.1}_{-2.4}$	6^{+1}_{-3}	$8.27^{+0.09}_{-3.38}$	$13.5^{+0.2}_{-5.5}$	12.5	11.9	23.7
14	$28.3^{+0.9}_{-4.1}$	20^{+1}_{-4}	$1.1^{+0.2}_{-0.4}$	$23.5^{+0.9}_{-3.7}$	$16.9^{+0.9}_{-3.4}$	$2.4^{+0.4}_{-0.8}$	48.5	22.5	23.1
15	25 ± 4	30^{+3}_{-5}	$3.6^{+0.5}_{-0.9}$	14^{+3}_{-2}	23^{+3}_{-4}	8^{+1}_{-2}	5.9	7.8	21.7
16	41^{+2}_{-7}	69^{+4}_{-13}	$9.1^{+0.9}_{-2.2}$	34^{+3}_{-6}	60^{+3}_{-11}	19^{+2}_{-5}	16.0	13.1	21.8
17	8^{+2}_{-3}	$9.5^{+0.5}_{-2.8}$	$3.6^{+0.2}_{-1.1}$	7^{+2}_{-3}	$9.0^{+0.4}_{-2.6}$	$8.2^{+0.5}_{-2.6}$	20.3	15.9	23.8
18	26^{+1}_{-11}	31^{+3}_{-12}	$5.1^{+0.6}_{-2.5}$	22^{+1}_{-10}	28^{+2}_{-11}	11^{+1}_{-5}	17.0	13.9	22.2
19	15^{+3}_{-4}	$10.1^{+0.4}_{-1.8}$	$1.9^{+0.3}_{-0.9}$	11^{+2}_{-3}	$8.8^{+0.4}_{-1.7}$	$4.2^{+0.7}_{-2.0}$	7.8	9.0	21.8
20	$7.3^{+0.2}_{-5.5}$	$7.3^{+0.1}_{-5.2}$	$4.4^{+0.2}_{-2.5}$	$7.8^{+0.2}_{-5.8}$	$7.79^{+0.09}_{-5.52}$	$9.7^{+0.6}_{-5.6}$	80.5	52.4	28.3
21	49^{+1}_{-15}	$43.4^{+0.9}_{-12.2}$	$11.5^{+0.4}_{-4.2}$	$43.9^{+0.8}_{-14.1}$	$40.0^{+0.6}_{-11.3}$	25^{+1}_{-9}	27.9	19.1	23.9
22	$8.4^{+0.5}_{-4.9}$	$13.4^{+0.1}_{-9.2}$	$1.7^{+0.3}_{1.6}$	$7.1^{+0.4}_{-4.6}$	$12.0^{+0.1}_{-8.3}$	$3.6^{+0.8}_{-3.3}$	14.9	12.7	21.8
23	6^{+1}_{-4}	$7.9^{+0.1}_{-4.9}$	$1.9^{+0.2}_{-1.8}$	5^{+1}_{-3}	$7.1^{+0.1}_{-4.7}$	$4.3^{+0.6}_{-4.0}$	11.1	10.7	22.3
24	$9.8^{+0.2}_{-3.0}$	$6.3^{+0.7}_{-2.4}$	$0.16^{+0.03}_{-0.09}$	$6.9^{+0.2}_{-2.3}$	$4.7^{+0.5}_{-1.8}$	$0.32^{+0.06}_{-0.18}$	78.9	25.8	22.5
25	8^{+1}_{-5}	$7.6^{+0.1}_{-3.7}$	$1.8^{+0.2}_{-1.6}$	6^{+1}_{-4}	$6.7^{+0.2}_{-3.3}$	$4.0^{+0.6}_{-3.5}$	8.4	9.4	22.1
26	$6.1^{+0.7}_{-3.0}$	$7.8^{+0.2}_{-4.2}$	$5.4^{+0.1}_{-4.2}$	$6.3^{+0.8}_{-3.1}$	$8.0^{+0.1}_{-4.2}$	$12.4^{+0.2}_{-7.1}$	23.9	19.7	25.0
27	$3.0^{+0.2}_{-2.0}$	$10.1^{+0.6}_{-5.7}$	$6.2^{+0.3}_{-5.7}$	$2.4^{+0.2}_{-1.6}$	$9.5^{+0.4}_{-5.7}$	$14.3^{+0.7}_{-9.6}$	8.1	9.4	23.2
28[a]	2.1 ± 0.7	$24.9^{+0.1}_{-4.6}$	$8.79^{+0.06}_{-2.07}$	1.8 ± 0.6	$22.6^{+0.1}_{-4.1}$	$19.8^{+0.1}_{-4.7}$	13.1	11.8	23.2

Note. These fluxes and conversion factors are determined from spectral fitting. The *NuSTAR* fluxes represent the average of the FPMA and FPMB fluxes. Errors provided are 1σ confidence intervals.

[a] Due to the poor photon statistics of NNR 28, it was not possible to perform spectral fitting in the same way as for the other sources. Adopting an absorbed power-law model for this source with $\Gamma = 1.8$ and $N_H = 10^{23}$ cm^{-2}, we determined the *Chandra* and *NuSTAR* fluxes using the C-statistic (see Section 5.7 for more details).

6.1.1. Colliding Wind Binaries

Two of the *NuSTAR* sources in the Norma region are likely CWBs: NNR 7 and 14.

NNR 7 actually consists of two *Chandra* sources blended together due to *NuSTAR*'s PSF. In *Chandra* ObsID 11008, where these two sources are resolved, they exhibit very similar spectral properties (N_H and kT values are consistent at the $<1\sigma$ level), but the 0.5–10 keV flux of NARCS 1279 is 2 times higher than the flux of NARCS 1278. These sources are blended in *Chandra* ObsIDs 12508 and 12509 because they are far off-axis, and the combined flux of the two sources is a factor of 3 higher in these later observations. Spectroscopic follow-up of the near-IR counterparts of both of these *Chandra* sources revealed that they are Wolf–Rayet stars of spectral type WN8 (Rahoui et al. 2014). These stars belong to the young massive cluster Mercer 81 (Mercer et al. 2005), located at a distance of 11 ± 2 kpc (Davies et al. 2012). The *Chandra* spectra of these sources were better fit by thermal plasma models than power-law models, suggesting that these sources were more likely to be CWBs than HMXBs with

compact objects accreting from the powerful Wolf–Rayet stellar winds.

The *NuSTAR* data provide even stronger support for the CWB hypothesis for NNR 7. Joint fitting of the *Chandra* (from NARCS) and *NuSTAR* spectra of these blended sources reveals that they fall off steeply above 1 keV and show prominent Fe line emission, primarily due to Fe XXV based on its 6.76 ± 0.1 keV line energy (House 1969). The spectra are best fit by an apec thermal model with $kT = 3.2^{+0.8}_{-0.5}$ keV and a metal abundance of 0.5 ± 0.3 solar, or a steep power-law model with $\Gamma = 3.4^{+0.4}_{-0.3}$ and Fe line emission with 650 ± 20 eV equivalent width. These spectral properties rule out the possibility that NNR 7 could be an accreting HMXB, since accreting HMXBs have harder power-law spectra and Fe I Kα emission at 6.4 keV, typically with equivalent widths <100 eV (Torrejón et al. 2010). Elshamouty et al. (2016) found that, in quiescence, one neutron star HMXB, V0332 +53, exhibits a soft spectrum ($\Gamma \approx 4$ or $kT_{BB} \approx 0.4$ keV) without prominent Fe lines. If this spectrum is typical of quiescent HMXBs, then we can also rule out the possibility
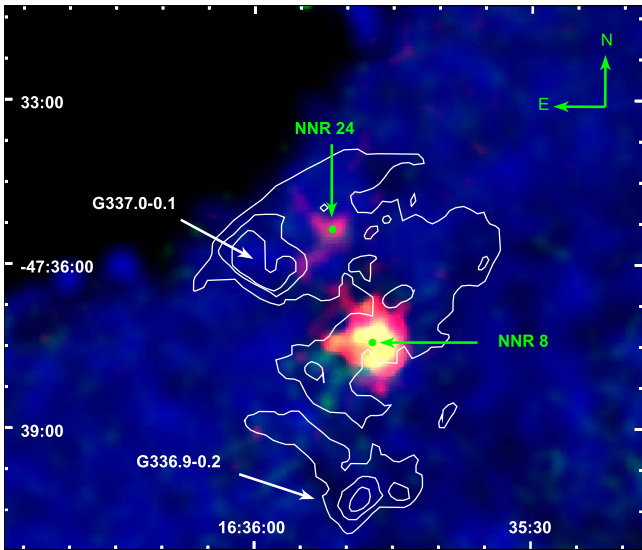
Figure 9. *NuSTAR* image of the region around NNR 8. The 3–10 keV band is shown in red, 10–20 keV in green, and 20–40 keV in blue. White contours show the radio continuum emission of the CTB 33 complex from Sarma et al. (1997). Green points denote the positions of *NuSTAR* sources. G337.0–0.1 is a confirmed SNR, while G336.9–0.2 is an H II region. It has been suggested that the magnetar, NNR 24, is associated with this SNR (Brogan et al. 2000). However, the extended emission of NNR 8 is clearly not coincident with G337.0–0.1, and its origin may be an unassociated PWN.

that NNR 7 is a quiescent HMXB, given its hard spectrum and prominent Fe emission. The unabsorbed 0.5–10 keV flux of NNR 7 based on the combined NARCS and *NuSTAR* spectrum[26] is $1.20^{+0.04}_{-0.12} \times 10^{-12}$ erg cm^{-2} s^{-1}. Adopting the 0.5–10 keV flux ratio for NARCS 1278 and 1279 and the bolometric luminosities of their Wolf–Rayet counterparts calculated by Rahoui et al. (2014), we find that their respective X-ray luminosities are 5×10^{33} and 1.2×10^{34} erg s^{-1}, and they have $L_X/L_{bol} = 1.3 \times 10^{-6}$ and 8×10^{-7}, respectively.

Isolated high-mass stars are known to be X-ray emitters, but their spectra typically have $kT \sim 0.5$ keV, and their 0.5–10 keV luminosities follow the scaling relation $L_X/L_{bol} \approx 10^{-7}$ (e.g., Berghoefer et al. 1997; Sana et al. 2006). The harder X-ray emission and higher L_X/L_{bol} exhibited by NNR 7 have been observed from the wind-wind shocks in CWBs (Zhekov & Skinner 2000; Portegies Zwart et al. 2002) and the magnetically channeled shocks of high-mass stars with $\sim$kG fields (Gagné et al. 2005; Petit et al. 2013). For NNR 7, a CWB nature is more likely given the strength of the Fe line at 6.7 keV; magnetic high-mass stars tend to exhibit weak Fe XXV line emission (Schulz et al. 2000; Schulz et al. 2003), while the Fe XXV lines in CWB spectra can have equivalent widths as large as $\sim$1–2 keV (Viotti et al. 2004; Mikles et al. 2006). The X-ray spectrum of NNR 7 exhibits substantial absorption corresponding to $N_H = 1.1 \pm 0.2 \times 10^{23}$ cm^{-2}, which is in excess of the integrated interstellar absorption along the line of sight ($N_{HI+H_2} = 7.8 \times 10^{22}$ cm^{-2}). The excess absorption measured in the X-ray spectrum of NNR 7 could be due to either inhomogeneities in the interstellar medium (ISM) or local absorption, which is observed in some CWBs, such as η Carinae (Hamaguchi

---

[26] The unabsorbed 0.5–10 keV flux reported here for NARCS 1278 and 1279 combined is higher than that reported in Rahoui et al. (2014) because we account for the absorption due to the X-ray derived N_H, while in Rahoui et al. (2014), only absorption attributed to the ISM is removed.

et al. 2007). Finally, X-ray variability is more common in CWBs than in isolated high-mass stars (Corcoran 1996). The X-ray flux variations displayed by CWBs are primarily associated with the orbital period of the binary and can be as large as a factor of ≈ 20 (Pittard et al. 1998; Corcoran 2005). Thus, the X-ray variability exhibited by NNR 7 provides further evidence of its CWB origin.

NNR 14 shares many similarities with NNR 7 and is also likely to be a CWB. The near-IR spectrum of the counterpart of NNR 14 shows emission lines typical of a Wolf–Rayet star of spectral type WN7 in the *K*-band, but the *H*-band spectrum lacks the emission lines expected for this spectral type. Overall, the near-IR spectrum may be consistent with an O3I star (J. Corral-Santana et al. 2017, in preparation). Its X-ray spectrum is well fit by an apec thermal model with $kT = 2.1^{+0.9}_{-0.5}$ keV or a power law with $\Gamma = 4.1^{+1.2}_{-0.9}$ and Fe line emission centered at $6.59^{+0.08}_{-0.06}$ keV (consistent with Fe XXV 6.7 keV emission) with a very high equivalent width of 1.8 ± 0.5 keV, making it very similar to the CWB candidate CXO J174536.1–285638 (Mikles et al. 2006). Furthermore, NNR 14 exhibits a very high X-ray absorbing column ($N_H = 2.9^{+0.9}_{-0.7} \times 10^{23}$ cm^{-2}) that is well in excess of the integrated interstellar column density along the line of sight ($N_{HI+H_2} = 8 \times 10^{22}$ cm^{-2}); this amount of absorption local to the X-ray source is larger than that for NNR 7 but still within the range observed in CWBs (Hamaguchi et al. 2007). NNR 14 is coincident with G338.0–0.1, an H II region most likely located at a distance of 14.1 kpc (Wilson et al. 1970; Kuchar & Clark 1997; Jones & Dickey 2012). It would not be surprising for NNR 14 and G338.0–0.1 to be physically associated, since H II regions are photoionized by high-mass stars, and the extreme N_H along the line of sight to NNR 14 indicates that it is likely located in the far Norma arm or beyond. Thus, adopting a distance of 14 kpc for NNR 14, its unabsorbed 3–10 keV luminosity is 10^{34} erg s^{-1}, which is within the typical range for CWBs.

6.1.2. Supernova Remnants and Pulsar Wind Nebulae

In addition to HESS J1640–465, there are three other extended sources in the *NuSTAR* Norma survey: NNR 5, 8, and 21.

Jakobsen et al. (2014) identified the *Chandra* counterpart of NNR 5 as a PWN candidate due to its bow shock, cometary morphology, and hard power-law spectrum. Although an AGN or LMXB origin cannot be ruled out, these possibilities were disfavored due to the lack of significant X-ray variability, both on short-term timescales during the *NuSTAR* observation and on long-term timescales between the *Chandra* and *NuSTAR* observations, separated by 3 yr. Our search for pulsations in the *NuSTAR* data did not yield a detection that would have secured a PWN origin, but our search was only sensitive to high pulsed fractions >45%. A joint spectral fit to the *NuSTAR* and *Chandra* data, covering the point source and extended emission in both data sets, yielded a higher N_H value and steeper photon index than that measured by Jakobsen et al. (2014). Our best-fit photon index of $\Gamma = 2.3 \pm 0.3$ for a power-law model is possible for a pulsar/PWN ($\Gamma \sim 1$–2; Kargaltsev & Pavlov 2008), which is consistent with the earlier results, derived using *Chandra* and *XMM-Newton* data. However, the N_H value we measure ($2.7^{+1.0}_{-0.8} \times 10^{23}$ cm^{-2}) is higher than the integrated interstellar absorption along the line of sight ($N_H = 8 \times 10^{22}$ cm^{-2}), indicating that NNR 5 is likely on the far side of the Galaxy and may be associated with the star-forming complexes located at $\sim$10 kpc. This source may be subject to additional local absorption or lie within or behind molecular clouds.

The source NNR 8 is a region of extended emission with a centrally peaked morphology coincident with the CTB 33 supernova remnant (SNR) and H II complex located at a distance of ~11 kpc and visible at radio wavelengths (Sarma et al. 1997). While NNR 8 may be associated with this complex, it notably does not overlap nearby SNR G337.0–0.1, as shown in Figure 9. This hard X-ray diffuse emission was discovered in an *XMM-Newton* field containing the soft gamma-ray repeater (SGR) 1627–41 (NNR 24) and is attributed by Esposito et al. (2009) to either a galaxy cluster or a PWN. The joint *Chandra* and *NuSTAR* spectrum of NNR 8 is well fit by an absorbed power-law model with a typical pulsar/PWN index of $\Gamma = 1.8 \pm 0.2$. In contrast, an absorbed bremsstrahlung model yields a temperature of $kT = 25^{+22}_{-9}$ keV in the 0.5–20 keV band, which is higher than expected for most galaxy clusters (Maughan et al. 2012). No pulsations were detected from NNR 8, but our search was only sensitive to periodic signals with very high pulsed fractions (>48%), leaving open the possibility of a pulsar embedded in diffuse PWN emission.

Assuming NNR 8 is a PWN, we can estimate the spin-down energy loss of the pulsar from correlations based on the PWN X-ray luminosity and photon index. Since the high $N_{\rm H}$ ($1.4^{+0.7}_{-0.5} \times 10^{23}$ cm^{-2}) measured from the X-ray spectrum of NNR 8 indicates that it lies on the far side of the Galaxy, and it is reasonable to expect a PWN to be in the vicinity of star-forming regions, we adopt the 11 kpc distance of the far Norma arm and CTB 33 for NNR 8 and calculate its unabsorbed 2–10 keV luminosity to be 1.0×10^{34} erg s^{-1}. Using the correlation between 2–10 keV luminosity and spin-down energy loss from Possenti et al. (2002), we estimate the pulsar $\dot{E} \approx 7 \times 10^{36}$ erg s^{-1}. The pulsar spin-down luminosity can also be estimated from the PWN photon index using correlations derived by Gotthelf (2003). The photon index of NNR 8 yields $\dot{E} \approx 1.4 \times 10^{37}$ erg s^{-1}, which is consistent with the value determined from the correlation of L_X and $\dot{E}$ given the statistical uncertainties of the X-ray luminosity and photon index of NNR 8. The fact that these estimates of $\dot{E}$ are consistent provides additional support in favor of a PWN origin for this source.

The extended emission of NNR 21 is associated with SNR G337.2+0.1, located at a distance of ~14 kpc. Using *Chandra* observations, Jakobsen (2013) found that the radial profile of the SNR exhibits a central compact source, suggesting a pulsar powering a PWN, as well as excess emission at a radius of ≈1.8, attributable to the SNR shell. The dearth of *NuSTAR* photons from the central point source does not allow for a significant detection of a pulsar signal, so we cannot confirm the PWN origin of NNR 21. *XMM-Newton* observations of this SNR revealed that it has a nonthermal spectrum that steepens further from the central core (Combi et al. 2006, hereafter C06), as is seen in many plerionic SNRs (e.g., IC 443, 3C 58, and G21.5–0.9; Bocchino & Bykov 2001 and references therein). Spectral fitting of the *NuSTAR* and *Chandra* data results in a higher column density ($N_{\rm H} = 2.6^{+0.9}_{-0.7} \times 10^{23}$ cm^{-2}) and steeper photon index ($\Gamma = 2.6^{+0.5}_{-0.4}$) than that measured by C06 for the pulsar/PWN (central source and extended emission combined). The *Chandra/NuSTAR*-derived photon index, while consistent at the 90% confidence level with the *XMM* measured value ($\Gamma = 1.82 \pm 0.45$), is steeper than expected for a pulsar/PWN. We find that the unabsorbed 2–10 keV luminosity of NNR 21 is 3×10^{34} erg s^{-1}, and thus the L_X–$\dot{E}$ correlation from Possenti et al. (2002) yields a spin-down luminosity estimate of $\dot{E} \approx 1.5 \times 10^{37}$ erg s^{-1}. The spin-down luminosity that is

estimated using the Γ–$\dot{E}$ correlation from Gotthelf (2003) is in good agreement if it is based on the *XMM*-derived $\Gamma = 1.8$ ($\dot{E} \approx 1.4 \times 10^{37}$ erg s^{-1}), but it is at odds if the *Chandra/NuSTAR*-derived Γ is adopted ($\dot{E} > 1.7 \times 10^{38}$ erg s^{-1}).[27]

Comparing our power-law fits of NNR 21 with the results of C06, the *Chandra/NuSTAR*-derived $N_{\rm H}$ is statistically higher than the $N_{\rm H} = 1.15 \pm 0.27 \times 10^{23}$ cm^{-2} measured by C06 for the whole PWN, but it is consistent at better than 90% confidence with the value C06 measured for the outer region of the PWN ($N_{\rm H} = 1.62 \pm 0.56 \times 10^{23}$ cm^{-2}), which excludes the central $12''$ radius region. This central region has a much lower column density of $5.9 \pm 1.5 \times 10^{22}$ cm^{-2}. Even if we compare the results of our apec model fits with C06, the *Chandra/NuSTAR*-derived $N_{\rm H}$ is more consistent with the $N_{\rm H}$ value that C06 measured for the outer region than for the whole PWN. One possible explanation for these spatial and temporal $N_{\rm H}$ variations is that the outer region of the PWN is interacting with a molecular cloud. This scenario would naturally explain the higher $N_{\rm H}$ measured in the outer region of the PWN compared to the central region by C06, and the increase in the average $N_{\rm H}$ measured for the whole PWN between the 2004 *XMM* observation and the 2011 *Chandra* observation could be attributed to a larger fraction of the PWN interacting with the dense interstellar medium as the PWN expands. Additional X-ray observations to obtain spatially resolved spectroscopy of NNR 21 are required to better understand the origin of the spectral variations exhibited by this SNR.

6.1.3. Magnetars

A known magnetar and a magnetar candidate are present in the *NuSTAR* Norma survey. NNR 24 is a known soft gamma-ray repeater, SGR 1627–41, which was discovered by the Burst and Transient Source Experiment (BATSE) when the source went into outburst in 1998 June (Woods et al. 1999). It has been suggested that this SGR is associated with the young SNR G337.0–0.1 in the CTB 33 complex (Hurley et al. 1999), shown in Figure 9. SGR 1627–41 last went into outburst in 2008 (Esposito et al. 2008), and it was found to have returned to quiescence by 2011 in NARCS observations (An et al. 2012). The cross-normalization constant from fitting the *NuSTAR* and *Chandra* spectra is consistent with 1.0 at 90% confidence, indicating that the magnetar persists in quiescence and has not significantly decreased in flux since 2011. We measure a photon index of $5.0^{+2.2}_{-1.4}$, which is steeper but still consistent with that measured by An et al. (2012) at 90% confidence. Assuming a distance of 11 kpc based on the association with the CTB 33 complex, we find that NNR 24 has unabsorbed luminosities of 2.3×10^{33} erg s^{-1} in the 3–10 keV band and 5.2×10^{31} erg s^{-1} in the 10–20 keV band.

NNR 10, a transient source, may also be a magnetar. The long-term variability and spectral analysis of this source is described in detail in T14, and our spectral analysis yields consistent results. The flux of NNR 10 varies by more than a factor of 20 over a 3 week period, with the peak of activity lasting between 11 hr and 1.5 days and having a soft spectrum with $\Gamma = 4.1^{+0.9}_{-0.8}$ or $kT = 3^{+2}_{-1}$ keV for a bremsstrahlung model. The high $N_{\rm H}$ measured from the X-ray spectrum of NNR 10 suggests that this source is located at $\gtrsim 10$ kpc and thus has a peak $L_X \gtrsim 10^{34}$ erg s^{-1} in the 2–10 keV band. As argued by T14, NNR 10 is most likely either a shorter-than-average

---

[27] The Γ–$\dot{E}$ correlation is only valid for $\Gamma < 2.36$, so we can only provide a lower bound on $\dot{E}$ for the *Chandra/NuSTAR*-derived $\Gamma = 2.6^{+0.5}_{-0.4}$.

outburst from a magnetar or an unusually bright flare from a chromospherically active binary.

6.1.4. Black Hole Binary Candidate

Among the remaining *NuSTAR* Norma sources not discussed in Sections 6.1.1–6.1.3, NNR 15 stands out as the only source showing clear short-timescale variability in the *NuSTAR* band and also having the lowest median energy. As can be seen in Figure 5, NNR 15 displays flaring behavior in the 3–20 keV band; during one flare lasting about 15 ks, the source flux increases by a factor of >6, and, during a smaller flare lasting about 7 ks, the flux increases by a factor of >2. This source also shows variability on year-long timescales, since the 3–10 keV flux measured in 2013 *NuSTAR* observations is a factor of 2 higher than the *Chandra* flux measured from 2011 observations. The *NuSTAR* and *Chandra* spectra are well fit by an absorbed power-law model with very low N_H, indicating that the source must reside within a few kpc, and $\Gamma = 2.6 \pm 0.4$ (or $kT = 2.9^{+1.0}_{-0.7}$ keV for a bremsstrahlung model). No Fe line is visible in the spectrum, but, due to the limited photon statistics, we can only constrain the equivalent width of a potential Fe line feature to be <1.7 keV, a loose constraint that does not help to distinguish between different types of X-ray sources. Assuming a distance of 2 kpc, NNR 15 has an average unabsorbed 3–20 keV luminosity of 1.5×10^{32} erg s^{-1}. Its optical/infrared counterpart has been identified as a mid-GIII star (Rahoui et al. 2014).

Based on these properties, we identify NNR 15 as a BH LMXB candidate in quiescence, although an active binary (AB) or CV origin cannot be entirely ruled out. In quiescence, ABs typically have $L_X = 10^{29-31.5}$ erg s^{-1} and $kT < 2$ keV (Dempsey et al. 1993), but they can exhibit flares with peak luminosities of $\sim 10^{32}$ erg s^{-1} and $kT \approx 10$ keV (Franciosini et al. 2001). However, AB flares tend to have very short rise times and long decay times (Pandey & Singh 2012), whereas the flares seen in NNR 15 appear to have more symmetric profiles. CVs have $L_X = 10^{29-33}$ erg s^{-1} and $kT = 1 - 25$ keV (e.g., Eracleous et al. 1991; Muno et al. 2004), with magnetic CVs being more luminous and spectrally harder than nonmagnetic CVs (Barlow et al. 2006; Landi et al. 2009), so their properties are consistent with those of NNR 15. However, the flaring exhibited by NNR 15 is not typically seen in CVs. Nonmagnetic CVs have outbursts that last several days and recurrence times of weeks to months; intermediate polars (IPs) have outbursts of similar duration but that are very rare (Hellier et al. 1997; Szkody et al. 2002). Polars exhibit flares with $\sim$hour-long durations, but they tend to be very soft ($kT < 1$ keV; Choi et al. 1999; Still & Mukai 2001; Traulsen et al. 2010). The properties of NNR 15 are reminiscent of the quiescent state of V404 Cyg, a well-known LMXB hosting a BH (Makino et al. 1989; Casares et al. 1992; Shahbaz et al. 1996). Recent *NuSTAR* observations of V404 Cyg in quiescence show that, in the 3–25 keV band, its power-law spectrum has $\Gamma = 2.35 \pm 0.2$ and it exhibits flux variations of up to a factor of 10 over periods of a few hours (Rana et al. 2016). Given the similarities between the X-ray spectra and light curves of NNR 15 and V404 Cyg, NNR 15 is most likely a BH LMXB, although it may be a CV or an AB. To order-of-magnitude accuracy, it is estimated that $\sim$1000 quiescent BH LMXBs reside in the Galaxy (Tanaka 1996); the primary source of uncertainty in this estimate is our limited knowledge of the typical recurrence timescale of BH transients. Making the simplifying assumption that quiescent BH binaries trace the stellar mass distribution of the

Galaxy, and using the estimate of the stellar mass enclosed in the Norma survey area by F14, we would expect $\sim$4 BH LMXBs to reside in the survey area. Thus, it is at least plausible that one BH binary would be detected in the *NuSTAR* Norma survey.

6.1.5. Cataclysmic Variables and Active Galactic Nuclei

Based on the NARCS results, we expect that the majority of the *NuSTAR* Norma sources should be a mixture of CVs and AGNs. CVs typically have thermal spectra with $kT \approx 1–30$ keV, although IPs can display even higher temperatures ($kT \approx 30–50$ keV; Landi et al. 2009), while AGNs exhibit power-law spectra with $\Gamma \approx 1.5–2$ (Tozzi et al. 2006; Sazonov et al. 2008). The remaining 17 tier 1 sources (NNR 4, 6, 9, 11–13, 16–20, 22, 23, and 25–28) have bremsstrahlung temperatures and photon indices consistent with being either CVs or AGNs. With the *NuSTAR*, *Chandra*, and infrared data available for these sources, there are three primary ways to distinguish CVs and AGNs:

i. If the absorbing column density inferred from X-ray spectral fitting or *Chandra* quantiles is significantly lower than the integrated interstellar N_H along the line of sight to the source, it is a Galactic source.

ii. If the source does not have a point-like infrared counterpart with $>98\%$ reliability in the VVV survey, it may be an AGN or a Galactic source with a K or M main-sequence companion, which would fall below the VVV sensitivity limits ($Ks < 18$ mag) if located at $\gtrsim 2$ kpc. Since the energy bands used by the *Wide-Field Infrared Survey Explorer* (*WISE*; Wright et al. 2010) can be more useful than the *J*, *H*, or *K* bands for identifying AGNs (Mateos et al. 2012; Stern et al. 2012), we also searched for counterparts to the *NuSTAR* sources in the AllWISE catalog (Cutri et al. 2013). The BH binary candidate NNR 15 and four tier 2 sources (NNR 29, 30, 31, and 38) have *WISE* matches located within the 95% positional uncertainty of their *Chandra* counterparts. The counterparts of NNR 15, 29, and 30 have been identified as low-mass stars through spectroscopic follow-up (Rahoui et al. 2014), and the other *WISE* counterparts have $W1 - W2 < 0.1$, far below the typical value of $W1 - W2 \geqslant 0.8$ for X-ray luminous AGNs (Stern et al. 2012). Furthermore, the near-IR spectra of the counterparts of NNR 31 and 38 indicate that they are Galactic sources (J. Corral-Santana et al. 2017, in preparation). Thus, none of the NNR sources with *WISE* counterparts are AGNs, but we cannot rule out the possibility that some AGNs are undetected by *WISE*. For instance, in the *NuSTAR* serendipitous survey, which has sensitivity limits comparable to those of the *NuSTAR* Norma survey, about 25% of the *NuSTAR* sources at Galactic latitudes $|b| > 10°$, which are likely to be AGNs, do not have a *WISE* counterpart (Lansbury et al., submitted).

iii. If the source exhibits strong unshifted Fe emission, it is more likely to be a CV than an AGN. Both magnetic and nonmagnetic CVs often exhibit Fe emission; in some sources, individual Fe lines at 6.4, 6.7, and 6.97 keV with equivalent widths of 100–200 eV can be seen, while in others, a broad component centered around 6.7 keV with an equivalent width of up to a few keV is seen, likely resulting from the blending of multiple Fe lines due to low energy resolution (e.g., Mukai & Shiokawa 1993; Ezuka & Ishida 1999; Baskill et al. 2005; Bernardini

et al. 2012; Xu et al. 2016). Both type I and type II AGNs often exhibit redshifted Fe emission, with the neutral Fe line typically being strongest, except in some highly ionized AGNs where the He-like and H-like Fe lines can rival the neutral Fe line in strength. Fe line emission from AGNs typically has equivalent widths <100 eV, but they can be higher in Compton-thick AGNs (Page et al. 2004; Iwasawa et al. 2012; Ricci et al. 2014). The Fe lines in X-ray binaries also tend to have equivalent widths $\lesssim100$ eV, so the strength of Fe line emission can also help discriminate between CVs and LMXBs (Hirano et al. 1987; Nagase 1989).

Seven of the tier 1 sources (NNR 4, 6, 9, 12, 18, 19, and 25) fulfill at least one of the three criteria listed above and are most likely CVs. NNR 4 meets all three criteria, and there is strong evidence that it is an IP, a CV in which the WD magnetic field is strong enough ($B \approx 10^{6-7}$ G) to truncate the accretion disk and channel the accreting material onto the magnetic poles. The X-ray spectrum of NNR 4 shows low absorption ($N_{\rm H} < 4 \times 10^{21}$ cm^{-2}), indicating that it is a Galactic source residing at a distance of $\lesssim2$ kpc. The joint fitting of the *Chandra* and *NuSTAR* spectra provides evidence for partial-covering absorption, which is frequently observed in IPs as some of the X-rays produced in the accretion column pass through the accretion curtain on their way to the observer (de Martino et al. 2004; Bernardini et al. 2012). The near-IR counterpart of NNR 4 is variable and displays emission lines often produced in the accretion streams of IPs (Rahoui et al. 2014). Furthermore, this source also exhibits Fe line emission centered at $6.65^{+0.10}_{-0.06}$ keV with a high equivalent width ($0.9^{+0.2}_{-0.1}$ keV) and a 7150 s period detected by *Chandra*, both of which are typical for IPs (Scaringi et al. 2010). NNR 4 exhibits flux variations on month–year timescales, which is more typical for nonmagnetic CVs and polars than IPs (Ramsay et al. 2004). But the flux only varies by a factor of <2, so the case for this source being an IP remains strong. Assuming a distance of 2 kpc, the unabsorbed 3–10 keV luminosity of NNR 4 is $2-4 \times 10^{32}$ erg s^{-1}, which is within the luminosity range of IPs (Muno et al. 2004 and references therein).

Sources NNR 6, 9, and 12 all have strong Fe emission centered between 6.4 and 6.8 keV and equivalent widths of 1.3 ± 0.4, 0.4 ± 0.2, and 1.2 ± 0.4 keV, respectively. This strongly indicates that these sources are CVs, since both AGNs and X-ray binaries tend to have much weaker Fe emission, and the Fe emission from AGNs is likely to be redshifted. These large equivalent widths are likely due to multiple Fe lines being blended because of *NuSTAR*'s low energy resolution. NNR 6 and 9 are best fit by thermal models with high plasma temperatures ($kT > 15$ keV), which are more typical of magnetic than nonmagnetic CVs (Landi et al. 2009; Xu et al. 2016). The lack of flux variations for NNR 6 and 9 suggests that they are most likely IPs. In addition, NNR 6 has a low-mass (late GIII) stellar counterpart (Rahoui et al. 2014), lending further support to a CV origin for this source. The nature of NNR 12 is less certain, because its softer spectrum ($kT = 6^{+3}_{-1}$ keV for an apec model) is typical for both nonmagnetic and magnetic CVs. NNR 12 is likely located at a distance >10 kpc given its high $N_{\rm H}$, so its 3–10 keV luminosity is likely $\gtrsim2 \times 10^{33}$ erg s^{-1}; this high luminosity, coupled with the lack of flux variability, suggests that this source is also probably an IP.

Another likely IP candidate is NNR 13. This source displays one of the hardest spectra of all of the *NuSTAR* Norma sources, with $kT > 21$ keV or $\Gamma = 1.0 \pm 0.5$. Its very hard spectrum and constant flux over long timescales is typical of IPs.

The nature of NNR 18 is discussed in B14; our spectral analysis yields consistent results, finding a high $N_{\rm H}$ of $1.9^{+0.9}_{-0.6} \times 10^{23}$ cm^{-2} and $\Gamma = 2.6^{+1.0}_{-0.8}$. Assuming a distance of >10 kpc based on the high $N_{\rm H}$ value, NNR 18 has an unabsorbed 3–10 keV luminosity $\gtrsim5 \times 10^{33}$ erg s^{-1}. NNR 18 has an early MIII counterpart and exhibits mild X-ray variability on short timescales in *Chandra* observations. As discussed by B14, these properties are consistent with those of an IP or LMXB. Another possibility is that this source is a hard-spectrum symbiotic binary (SB) hosting a WD or a symbiotic X-ray binary (SyXB) hosting a NS (Luna et al. 2013). The compact objects in SBs and SyXBs accrete material from the wind of a red giant companion, which is typically of spectral type M or K (Morihana et al. 2016). Hard-spectrum SBs and SyXBs display X-ray luminosities between 10^{32} and 10^{34} erg s^{-1} (Masetti et al. 2002; Smith et al. 2008; Nespoli et al. 2010) and variability on short and long timescales (Luna & Sokoloski 2007; Corbet et al. 2008). An IP origin is favored for NNR 18 based on its low levels of variability, while its estimated luminosity and the M giant spectral type of its counterpart favor an SB or SyXB origin.

NNR 19 and 25 show low absorption in their X-ray spectra, indicating that they are Galactic sources and probably located at a distance of a few kpc. Both sources are transients that were not detected in NARCS, but they were detected in follow-up *Chandra* observations taken 3 and 34 days after the *NuSTAR* observations, respectively. The flux of NNR 25 increased by a factor of $\geqslant4$ in the couple of years between the NARCS and *NuSTAR* observations and remained high for at least 34 days. NNR 19 was detected at a consistent flux level in multiple *NuSTAR* observations that spanned ≈100 days. About 250 days before it was first detected by *NuSTAR*, the 90% confidence upper limit for its 3–10 keV photon flux was 2×10^{-6} cm^{-2} s^{-1} (a factor of 4 below its peak flux), and about 40 days after it was detected by *NuSTAR*, its flux fell below 4×10^{-6} cm^{-2} s^{-1}. Thus, we find that the flux of NNR 19 increased by a factor of $\geqslant4$ and remained high for a period between 100 and 400 days. In addition, NNR 19 was detected in the archival *Chandra* ObsID 7591, demonstrating that this transient experienced an outburst in 2007 during which its flux was a factor of $\geqslant7$ higher than the upper limit measured by NARCS in 2011. The spectra of NNR 19 and 25 have $kT = 11^{+18}_{-4}$ keV ($\Gamma = 1.7^{+0.3}_{-0.4}$) and $kT > 6$ keV ($\Gamma = 1.8 \pm 0.7$), respectively. The temporal and spectral properties of NNR 19 and 25 most closely resemble those of polars, CVs with magnetic fields so strong ($B > 10^7$ G) that the WD magnetosphere inhibits the formation of an accretion disk. Thus, compared to other CVs, polar X-ray emission is very sensitive to changes in the mass transfer rate, and polars exhibit flux variations of factors $\geqslant4$ as they transition between low and high accretion states on $\sim$month–year timescales (Ramsay et al. 2004; Worpel et al. 2016), very similar to the behavior of NNR 19 and 25. No IR counterparts in the VVV survey are found for NNR 19 or 25 within the 90% positional uncertainty determined from *Chandra*. While the variability and spectra of NNR 19 and 25 would also be consistent with hard-spectrum SBs or SyXBs, the lack of a counterpart with $Ks < 18$ mag rules out the possibility that these sources have red giant companions, which should be visible out to $\gtrsim10$ kpc. In contrast, it is possible for main-sequence K- or M-type stars located at distances of a few kpc to fall below the VVV survey sensitivity.

The nine remaining tier 1 sources (NNR 11, 16, 17, 20, 22, 23, 26, 27, and 28) are well fit either by thermal models with $kT = 4$–30 keV or power-law models with $\Gamma \approx 2$, consistent with the spectra of CVs, SBs, SyXBs, LMXBs, or AGNs. The uncertainties in the spectral parameters for many of these sources are quite large, since they are among the faintest in our survey. All of these sources have high absorption that is equal to or in excess of the ISM column density through the Galaxy, and they lack IR counterparts, so it is difficult to determine whether they are Galactic or extragalactic. The lack of counterparts does rule out the possibility that these sources are SBs or SyXBs, since their red giant companions should be visible through most of the galaxy given the sensitivity of the VVV survey ($Ks < 18$ mag). Based on the $\log N$–$\log S$ distribution of AGNs measured in the COSMOS survey (Cappelluti et al. 2009) and accounting for Galactic absorption, conversion from the 2–10 keV to the 3–10 keV band, and the sensitivity curve of the *NuSTAR* Norma survey (see Section 6.2), we estimate that about five AGNs are present in this survey. Therefore, roughly half of the remaining tier 1 sources may be AGNs. The other half are probably CVs, since quiescent LMXBs are expected to be relatively rare (Tanaka 1996). Additional *NuSTAR* or *XMM* observations are required to distinguish between the possible CV or AGN origin of these nine sources by measuring the strength of Fe line emission and better constraining their spectral hardness. The 3–10 keV fluxes of NNR 11, 20, and 28 vary by factors of >5 between the NARCS and *NuSTAR* observations. Such long-term variability is common for AGNs, polars, and nonmagnetic CVs (Orio et al. 2001; Markowitz & Edelson 2004; Ramsay et al. 2004; Baskill et al. 2005), so it does not help us discriminate between Galactic and extragalactic sources; however, it at least excludes an IP origin for these three sources.

The 10 tier 2 sources included in our catalog do not have enough *NuSTAR* counts to meaningfully constrain their spectral properties, but their distribution in the *Chandra* quantile diagram is very similar to the distribution of the 17 tier 1 sources described in this subsection: two are foreground sources, while the rest are heavily absorbed and have $\Gamma < 2$. Seven of these tier 2 sources (NNR 29, 30, 31, 34, 35, 36, and 38) have reliable IR counterparts, three of which (NNR 29, 30, and 36) have been spectrally identified as low-mass stars (Rahoui et al. 2014). These seven sources are likely to be a mixture of CVs, SBs, and SyXBs like the majority of identified tier 1 sources. NNR 29 and 36 display such low absorption that they are likely located within a few kpc and thus have 3–10 keV luminosities $\lesssim 3 \times 10^{31}$ erg s^{-1}, so they could also be active binaries given their low luminosity (Strassmeier et al. 1993). An AGN origin cannot be ruled out for NNR 34 and 35, which have VVV counterparts but are not detected by *WISE*. NNR 32, 33, and 37 lack IR counterparts, are heavily absorbed, and could be AGNs or Galactic sources. Based on the $\log N$–$\log S$ derived for AGNs and CVs in the Norma region by F14, a 1:2 ratio of AGNs to CVs/ABs is expected in the 2–10 keV flux range of these tier 2 sources ($4 \times 10^{-14} < f_X < 1 \times 10^{-13}$ erg cm^{-2} s^{-1}). Such a ratio is plausible among tier 2 sources given the current constraints we can place on their physical nature. However, it is odd that none of the sources that may be AGNs are detected by *WISE* with $W1 - W2 \geqslant 0.8$, since the majority of AGNs discovered in the *NuSTAR* serendipitous survey have these properties (Lansbury et al. 2017). The fact that our AGN candidates either lack IR

counterparts or have only VVV but not *WISE* counterparts indicates that, if they truly are AGNs, they are likely to have low luminosities ($L_X \lesssim 10^{43}$ erg s^{-1}).

6.1.6. On the Search for Low-luminosity HMXBs

As discussed in Section 1, one of reasons the Norma arm was targeted by *Chandra* and *NuSTAR* was to search for low-luminosity HMXBs with fluxes below the sensitivity limits of previous surveys. A key criterion for identifying an HMXB candidate is to find a source with a high-mass stellar counterpart, which should be visible in the infrared through the whole Galaxy in the VVV survey. Of the Norma sources detected by *NuSTAR*, only two, NNR 7 and 14, have high-mass stellar counterparts, and their broadband X-ray spectra indicate that they are CWBs (see Section 6.1.1). However, there are three *Chandra* sources, NARCS 239, 1168, and 1326, with high-mass stellar counterparts (Rahoui et al. 2014) that were not detected by the *NuSTAR* Norma survey. The 2–10 keV *Chandra* fluxes of these sources ($f_X \approx 7$–8×10^{-14} erg cm^{-2} s^{-1}; F14) are comparable to the sensitivity limit of the *NuSTAR* survey (see Section 6.2), and thus it is not surprising that they are not detected. In the *Chandra* band, these three sources have harder spectra than NNR 7 and 14 and reside in a region of quantile space consistent with $\Gamma \approx 2$ power-law spectra (F14), which are typical of accreting HMXBs.

Future spectroscopic observations of the infrared counterparts of these *Chandra* sources will confirm whether these systems are HMXBs and help to estimate better distances to these sources. Once we determine how many of these HMXB candidates, if any, are truly HMXBs, the constraints provided by the Norma survey on the faint end of the HMXB luminosity function will be presented in a future paper. By extrapolating the measured slope of the HMXB luminosity function above 10^{34} erg s^{-1} to lower luminosities, F14 predicted that at least a few HMXBs would be detected in the Norma region with $f_X > 7 \times 10^{-14}$ erg cm^{-2} s^{-1}. Thus, if the three HMXB candidates are confirmed, the number of HMXBs in the Norma region would be consistent with a continuation of the HMXB luminosity function slope to lower luminosities, but if none of these sources prove to be HMXBs, it would imply that the HMXB luminosity function flattens substantially at $L_X < 10^{34}$ erg s^{-1}.

6.2. Survey Sensitivity

To compute the sky coverage for the *NuSTAR* Norma survey, we used the same method employed for NARCS, which is taken from Georgakakis et al. (2008). For a given detection probability threshold, $P_{\rm thresh}$, we determined the minimum number of total counts required for a detection ($C_{\rm lim}$) at each position in the image, such that $P(\geqslant C_{\rm lim}) = P_{\rm thresh}$. To this end, we made background maps in the 3–10 keV and 10–20 keV bands by removing the counts within 60″ (90″) radius circular regions centered on the point (extended) source positions listed in Table 5 and then filling in these regions by randomly distributing the expected background counts determined from the local background. Using these background maps, we calculated the mean expected background counts ($\langle C_{\rm bkg} \rangle$) in circular regions centered on each pixel with radii equal to the 15%, 22%, and 30% PSF enclosures, which are the cell sizes we used for source detection (see Section 4). The probability that the observed counts will exceed $C_{\rm lim}$ within a
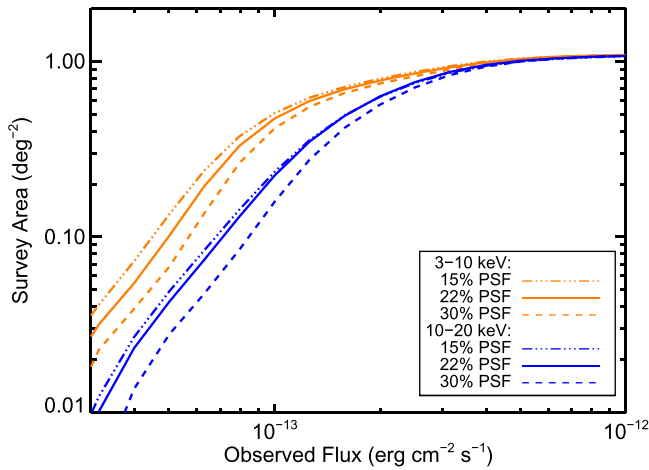
Figure 10. Sky coverage of the *NuSTAR* Norma region survey for different energy bands and PSF enclosure fractions. The curves in this plot use a photon flux to energy flux conversion factor based the spectral modeling of tier 1 sources.

particular region is

$$P(\geqslant C_{\mathrm{lim}}) = \gamma(C_{\mathrm{lim}}, \langle C_{\mathrm{bkg}} \rangle), \qquad (2)$$

where $\gamma(a, x)$ is the lower incomplete γ function, defined as

$$\gamma(a, x) = \frac{1}{\Gamma(a)} \int_0^x e^{-t} t^{a-1} dt. \qquad (3)$$

Calculating C_{lim} requires setting $P(\geqslant C_{\mathrm{lim}}) = P_{\mathrm{thresh}}$ and inverting Equation (2) numerically.

Then, we computed the probability of detecting a source of a given flux f_X at each pixel, given by

$$P_{f_X}(\geqslant C_{\mathrm{lim}}) = \gamma(C_{\mathrm{lim}}, C_{\mathrm{src}}) \qquad (4)$$

and $C_{\mathrm{src}} = f_X t_{\mathrm{exp}} A_{\mathrm{src}} \epsilon + \langle C_{\mathrm{bkg}} \rangle$, where t_{exp}, A_{src}, and ϵ are the exposure time, mean effective area, and unabsorbed energy flux to observed photon flux conversion factor, respectively. For ϵ, we used the mean ratio of photon flux to energy flux measured for tier 1 sources in a given energy band. To estimate the effective area at each pixel location, we made vignetting-corrected exposure maps. By comparing the ratio of the vignetting-corrected exposure over the uncorrected exposures to the effective areas of tier 1 sources, we derived a linear relation to convert the exposure ratio at a given location to the effective area for the average source spectrum. These relations were derived using vignetting corrections evaluated at 8 keV for the 3–10 keV band and at 10 keV for the 10–20 keV band; they were also calibrated for the three different cell sizes.

There are a few possible sources of systematic error in our calculation of the sky coverage curves. Different ϵ values and effective area to exposure ratio relations were derived based on nonparametric and modeling-derived fluxes to account for systematic errors associated with flux calculation methods; the sky coverage curves derived using these different fluxes vary by about 0.1 dex. Another potential source of systematic error arises from our use of the average source spectrum as representative of the *NuSTAR* Norma sources. Based on the spread of spectral properties they exhibit, a systematic error of roughly 0.1 dex on the sky coverage could result from the choice of a representative source spectrum. Finally, the calculated sky coverage includes all the observations shown

in Figures 1 and 2, but, as can be seen, a significant wedge of stray light and some residual ghost rays are present, especially in the 3–10 keV band. This contamination effectively reduces our sky coverage, because even though there were about 20 clusters of pixels in these regions that exceeded our detection threshold, we ascribed most of them to artifacts associated with stray light and ghost rays rather than true sources. The only exceptions we included in our final source list (NNR 2, 6, 10, 16, and 18) were either very bright sources, had bright ($\gtrsim 10^{-5}$ photons cm^{-2} s^{-1}) *Chandra* counterparts, or had a clear point-like morphology. Since the contaminated areas only make up about 2% of the total survey area, their inclusion in our sky coverage does not significantly impact our log$N$–log$S$ results.

The sky coverage was calculated as the sum of probabilities in Equation (4) over all pixels multiplied by the solid angle per pixel. We repeated this calculation for a range of fluxes to produce a sensitivity curve for each of the three detection cell sizes in both the 3–10 keV and the 10–20 keV bands. Figure 10 shows the sky coverage for different energy bands and cell sizes. We used the sensitivity curves for the 22% PSF enclosures to calculate the log$N$–log$S$ distribution and sensitivity limits of our survey in the 3–10 keV and 10–20 keV bands, because all but one of the 26 (17) tier 1 sources that were detected in the 3–10 keV (10–20 keV) band were detected in the 22% PSF trial maps, and the 22% PSF sky coverage represents a rough average of the different PSF fraction curves. The deep field of the *NuSTAR* Norma survey has an area of about 0.04 deg^2 and sensitivity limits of 4×10^{-14} erg cm^{-2} s^{-1} (5×10^{-14} erg cm^{-2} s^{-1}) in the observed (unabsorbed) 3–10 keV band and 4×10^{-14} erg cm^{-2} s^{-1} in the 10–20 keV band. The shallow survey has an area of ~ 1 deg^2 with sensitivity limits of 1×10^{-13} erg cm^{-2} s^{-1} (1.5×10^{-13} erg cm^{-2} s^{-1}) in the observed (unabsorbed) 3–10 keV band and 1.5×10^{-13} erg cm^{-2} s^{-1} in the 10–20 keV band.

6.3. The logN–logS Distribution

Since many of the *NuSTAR* Norma sources have fluxes approaching our sensitivity limits, when calculating the number-count distribution for our survey, it is important to consider the effect of Poisson fluctuations of the source and background counts on the measured source flux. Thus, rather than assigning a single flux value to each source, we determine its flux probability distribution by computing the source count distribution from Equation (A21) in Weisskopf et al. (2007) and converting counts to energy fluxes. The number count distribution is then equal to the sum of the flux probability distributions of individual sources divided by the sensitivity curve calculated in Section 6.2.

We computed log$N$–log$S$ distributions in the 3–10 keV and 10–20 keV bands for both observed and unabsorbed fluxes. In order to check for systematic errors, we performed these calculations using both the modeling-derived and nonparametric fluxes. When constructing the distribution in a given energy band, we only included the sources that exceed the detection threshold in that particular energy band. In addition, in order to compare the *NuSTAR* number-count distribution with that derived from NARCS, we excluded extended sources. For the sources that are blended in the *NuSTAR* observations but resolved with *Chandra*, we estimated the *NuSTAR* fluxes of the individual sources by assuming that the ratio of the fluxes (see comments in Table 9) of the two sources is the same in *NuSTAR* as it is in the *Chandra*
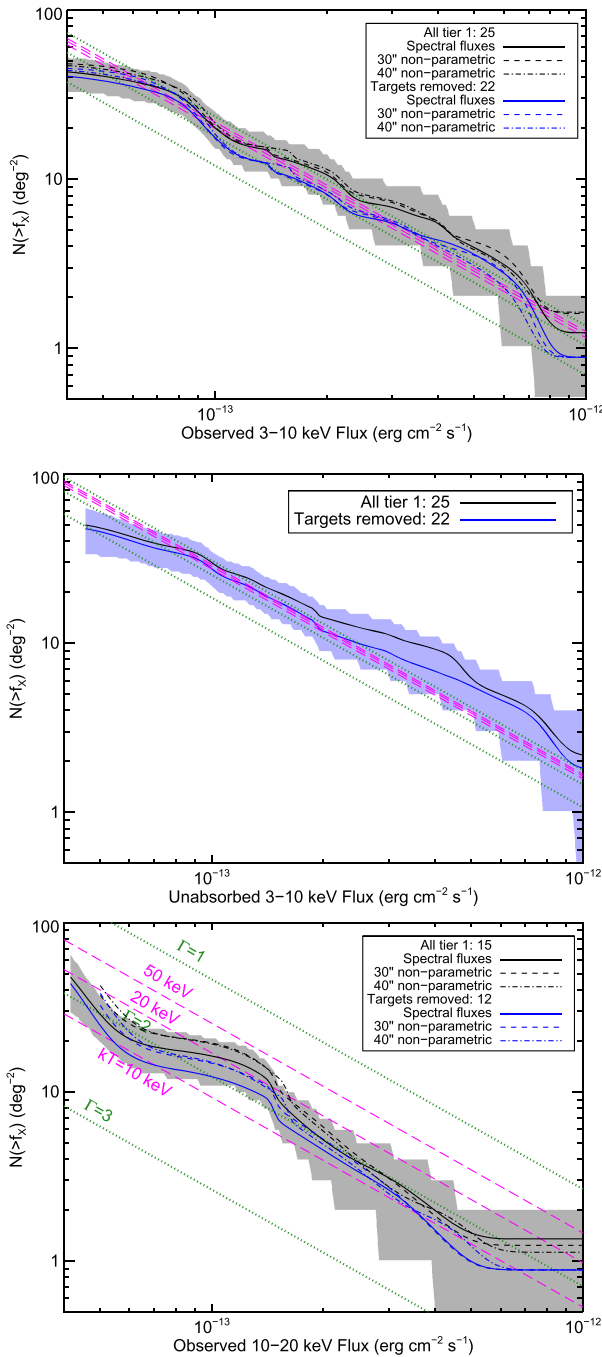
Figure 11. The log$N$–log$S$ distributions shown in black include all tier 1 sources exceeding the detection threshold in a given energy band. The gray band shows the 1σ errors on the log$N$–log$S$ distribution. The log$N$–log$S$ distributions shown in blue exclude NNR 2, 4, and 5, which were specifically targeted by *NuSTAR*. The green dotted (magenta dashed) lines show the NARCS log$N$–log$S$ converted from unabsorbed 2–10 keV into the given bands assuming power-law spectral models with $\Gamma = 3$, 2, and 1 (thermal models with $kT = 10$, 20, and 50 keV). When converting the NARCS distribution into the observed 3–10 or 10–20 keV bands, a column density of $N_H = 10^{23}$ cm^{-2} is used, the mean of measured N_H values for the *NuSTAR* sources; varying N_H between 0.7 and 2.0×10^{23} cm^{-2} does not significantly change the conversion factor. Top: the log$N$–log$S$ distribution in the 3–10 keV band, calculated using observed fluxes derived from spectral fitting, as well as nonparametric fluxes calculated from aperture photometry using 30″ and 40″ radius regions. Middle: the log$N$–log$S$ distribution in the 3–10 keV band, calculated using unabsorbed fluxes derived from spectral fitting. The blue band shows the 1σ errors on the distribution shown in blue. Bottom: same as top, except the log$N$–log$S$ distributions are shown as a function of observed 10–20 keV flux.

2–10 keV band. Thus, NNR 8 is excluded from the sample of sources used in the number-count distribution; the fluxes of the point sources at the center of the extended sources, NNR 3 and 21, are estimated to be 30% and 20% of the total, respectively; and the fraction of NNR 7's flux attributed to NARCS 1278 and 1279 is 30% and 70%, respectively.

We calculated the statistical errors of the log$N$–log$S$ distribution using the bootstrapping method. We accounted for the errors associated with our sample size, as well as the distribution of fluxes within that sample, by generating new samples of sources from our original list used to calculate the log$N$–log$S$ distribution. For each new sample, we drew the sample size (N_{sample}) from a Poisson distribution with a mean equal to the original sample size and then randomly selected N_{sample} sources from the original list. We generated 10,000 new samples and calculated the resulting log$N$–log$S$ distribution for each of them. Then, we used the simulated distributions to determine the 1σ upper and lower confidence bounds of the measured log$N$–log$S$ distribution. The 1σ statistical errors are comparable in size to the systematic errors associated with the sensitivity curves, which are discussed in Section 6.2.

In addition to the possible sources of systematic error already discussed, there is a simplification in our log$N$–log$S$ calculation that could bias our measurements. As described in Section 4.2, we require that a source exceed the detection threshold in two or three trial maps in order to be included in our source list, but our log$N$–log$S$ calculation does not explicitly account for this criterion. This criterion helps to screen out spurious detections that may occur in a given trial map but are unlikely to correlate across different energy bands or aperture sizes. However, it is an easy criterion for a real source to pass, since it is very likely for a real source exceeding the threshold in one trial map to exceed it in at least another trial map with the same energy band but a different PSF enclosure fraction. Thus, we do not expect our detection criterion to substantially alter the sensitivity curves or, in turn, the log$N$–log$S$ distribution. To gauge the magnitude of the possible bias due to our choice of sensitivity curve, we produced different versions of the log$N$–log$S$ distribution in the 3–10 keV and 10–20 keV bands. We adopted sensitivity curves for different PSF enclosures and tested the effect of limiting the source subsample to tier 1 sources exceeding the threshold in the trial map with the same energy band and PSF enclosure as the sensitivity curve, rather than just the same energy band. The resulting variations in our log$N$–log$S$ results are smaller than the statistical uncertainties.

Figure 11 shows the resulting log$N$–log$S$ distributions for the *NuSTAR* Norma region. Magenta and green lines show the log$N$–log$S$ distribution measured by NARCS converted from the unabsorbed 2–10 keV band to the *NuSTAR* bands assuming different spectral models: thermal models with $kT = 10$, 20, and 50 keV and power-law models with $\Gamma = 1$, 2, and 3. When converting to observed energy fluxes, a typical N_H value of 10^{23} cm^{-2} is used. The log$N$–log$S$ distributions shown in black include all tier 1 sources that exceed the detection threshold in a given energy band, while the blue distributions exclude the sources that were specifically targeted by *NuSTAR* and detected (NNR 2, 4, and 5), which could unnaturally inflate the log$N$–log$S$ distribution. As shown in the top panel, there is little difference between the NARCS distributions converted using different spectral models into the observed 3–10 keV band, which is not surprising given its large amount of overlap with the *Chandra* 2–10 keV band. Regardless of how the source energy fluxes are calculated, the *NuSTAR* distribution is consistent with the NARCS distribution at 1σ confidence, exhibiting a similar slope of

$\alpha \approx -1.24$. The *NuSTAR* distribution only deviates significantly from the NARCS distribution at low fluxes. This discrepancy may be due to the Eddington bias or variance in the spatial density of sources, given that the sources with the lowest fluxes are only detected in the deep HESS field, which is only 100 arcmin^2 in size.

The middle panel of Figure 11 shows the log$N$–log$S$ distribution calculated using the unabsorbed 3–10 keV fluxes from spectral fitting. Although this distribution is still largely consistent with the NARCS distribution at 1σ confidence when the sources specifically targeted by *NuSTAR* are removed (shown in blue), the *NuSTAR* distribution is slightly higher than the *Chandra* distribution above $>3 \times 10^{-13}$ erg cm^{-2} s^{-1}. The fact that this excess is seen using the unabsorbed 3–10 keV fluxes but not the observed 3–10 keV fluxes suggests that, for some sources, we measure N_H values that are too high and thus overcorrect for absorption.

The bottom panel of Figure 11 shows the log$N$–log$S$ distributions calculated using modeling-derived and nonparametric fluxes in the observed 10–20 keV band. Since there is very little difference between the observed and unabsorbed 10–20 keV fluxes, the log$N$–log$S$ distribution in the unabsorbed 10–20 keV band is not shown. Although the 10–20 keV *NuSTAR* distributions deviate from a simple power law due to the small number of sources (16) detected in this hard X-ray band, overall the slope is still consistent with the NARCS slope. The normalizations of the different NARCS distributions extrapolated into the 10–20 keV band are distinct depending on the spectral model assumed; for the *NuSTAR* and NARCS normalizations to be consistent, the average spectrum of the Norma sources must either have $kT = 10$–20 keV or $\Gamma = 2$. This average spectrum is indeed consistent with the individual spectral fits of most of the *NuSTAR* sources and their locations in the *NuSTAR* quantile space.

6.4. Comparison to the GC NuSTAR Population

Comparing the log$N$–log$S$ distributions of sources in the Norma region and the $1° \times 0°.6$ GC region surveyed by *NuSTAR*, the number density of the *NuSTAR* sources is ≈ 2 times higher in the GC (Hong et al. 2016). This is to be expected, since the stellar density in the vicinity of the GC is higher than the stellar density along the line of sight of the Norma region. The power-law slope of the number-count distribution is also steeper in the GC ($\alpha \approx -1.4$; Hong et al. 2016), which is consistent with the trend that is seen for *Chandra* sources in the GC and the field in the 0.5–8 keV band (Muno et al. 2009). In order for the normalizations of the GC *NuSTAR* and *Chandra* number-count distributions to be consistent, the typical spectrum of the GC sources must either have $kT = 20$–50 keV or $\Gamma \approx 1.5$, which is harder than the typical spectrum of Norma sources.

Hong et al. (2016) argue that 40%–60% of the *NuSTAR* GC sources are magnetic CVs, primarily IPs, given their very hard X-ray spectra ($\Gamma \lesssim 1.5$) and the presence of strong Fe emission. All but two of the Norma CV candidates have softer spectra ($\Gamma > 1.5$, $kT \lesssim 20$ eV). The spectral differences between the *NuSTAR* populations in the Norma and GC regions are mirrored in the differences between the Galactic ridge X-ray emission (GRXE; Revnivtsev et al. 2006a, 2006b, 2009) and the central hard X-ray emission (CHXE) discovered by *NuSTAR* in the GC (Perez et al. 2015). The lower temperatures of the Norma CV candidates are consistent with the thermal spectra of the GRXE, whose hot component has a temperature of $kT \approx 15$ keV (Türler et al. 2010; Yuasa et al. 2012), while the high temperatures of the GC CVs

resemble the $kT > 25$ keV emission observed in the inner few pc of the Galaxy (Perez et al. 2015; Hong et al. 2016).

However, it is unclear why the X-ray populations in the GC and the disk are different. Under the assumption that most of the sources contributing to the CHXE and GRXE are IPs, the differences in their typical X-ray temperatures have been attributed to differences in their WD masses, with WDs in the GC CVs having masses $\gtrsim 0.8$ $M_\odot$ (Perez et al. 2015; Hong et al. 2016) and those in the disk CVs having masses ≈ 0.6 $M_\odot$ (Krivonos et al. 2007; Türler et al. 2010; Yuasa et al. 2012). However, the mean WD mass among all CVs has been measured to be 0.83 ± 0.23 $M_\odot$ (Zorotovic et al. 2011), and the X-ray inferred masses of the confirmed field IPs are consistent with this higher value of ≈ 0.8 $M_\odot$ (Hailey et al. 2016). The discrepancy between the measured WD masses for the field CVs and the lower masses inferred from the temperature of the GRXE suggests that it may be incorrect to assume that the GRXE is dominated by IPs (Hailey et al. 2016). Thus, it may be similarly incorrect to attribute the temperature differences between the *NuSTAR* CV candidates in the GC and Norma regions to differences in their WD masses.

In fact, as discussed in Section 6.1.5, a significant fraction of the Norma CV candidates may not be IPs but rather a mixture of polars, nonmagnetic CVs, hard-spectrum SBs, and SyXBs. These types of sources have softer spectra than IPs, and thus the difference in the average temperatures of Norma and GC sources may be explained by variations in the relative fractions of different types of CVs and SBs. It is unclear what physical processes would drive variations in the relative fractions of different types of compact object binaries in these two Galactic regions, but investigating these issues further will first require confirming the true nature of the CV candidates.

The clearest ways of distinguishing different types of CVs and SBs is by measuring the relative flux ratios of their Fe emission lines (Xu et al. 2016) or measuring both their spin and orbital periods (Scaringi et al. 2010), but since most of the Norma CV candidates are quite faint, it will be difficult to obtain X-ray spectra or light curves with enough photons to make such measurements with current telescopes. Monitoring the long-term X-ray and infrared variability of the CV candidates and determining the spectral types of their counterparts more accurately in order to estimate distances and luminosities will help to identify the nature of these sources.

7. Conclusions

1. We have detected 28 hard X-ray sources in a square-degree region in the direction of the Norma spiral arm surveyed by *NuSTAR* that are designated as tier 1 sources. Twenty-three of these sources were previously detected in NARCS observations; one was a well-studied BH transient (4U 1630–472), and four were newly discovered transients that we followed up and localized with *Chandra*. Out of 28 sources, 16 are detected above 10 keV. In addition, we found 10 NARCS sources with 2–10 keV fluxes $>6 \times 10^{-6}$ cm^{-2} s^{-1} that did not exceed our formal detection threshold for *NuSTAR* but displayed significant X-ray emission (S/N $>$ 3) in at least one of three energy bands; these are designated as tier 2 sources. We have provided photometric information for these sources in our catalog but do not include them in our calculation of the log$N$–log$S$ distribution, since they do not meet our detection thresholds.

Table 11
Classification of NNR Sources

Source No.	Classification
	Tier 1—Confirmed
1	BH LMXB
2	NS HMXB
3	pulsar/PWN
	Tier 1—Candidate
4	CV (IP)
5	bow shock PWN
6	CV (IP)
7	CWB
8	young PWN
9	CV (IP)
10	magnetar or AB
11	CV (polar or nonmagnetic) or AGN
12	CV (IP)
13	CV (IP)
14	CWB
15	BH LMXB
16	CV or AGN
17	CV or AGN
18	CV (IP), SB, SyXB
19	CV (polar)
20	CV (polar or nonmagnetic) or AGN
21	PWN/SNR
22	CV or AGN
23	CV or AGN
25	CV (polar)
26	CV or AGN
27	CV or AGN
28	CV (polar or nonmagnetic) or AGN
	Tier 2—Tentative
29	Galactic
30	Galactic
31	Galactic
32	Galactic or AGN
33	Galactic or AGN
34	Galactic or AGN
35	Galactic or AGN
36	Galactic
37	Galactic or AGN
38	Galactic

Notes. Classifications of NNR sources are discussed in Section 6.1. The classifications of NNR 1, 2, and 3 are robust, while all other classifications of tier 1 sources should be considered candidate identifications (see Section 6.1 for details). For candidate CVs, we provide in parentheses the most likely CV type when possible. For tier 2 sources, we provide only tentative classifications of the sources as Galactic or extragalactic AGNs.

2. The log$N$–log$S$ distribution of the *NuSTAR* sources in the 3–10 keV band is consistent with the distribution of the 2–10 keV *Chandra* sources in the Norma region.

3. The *NuSTAR* log$N$–log$S$ distribution in the 10–20 keV band is consistent with the 2–10 keV *Chandra* distribution if the average spectrum of the *NuSTAR* sources can be described by a power-law model with $\Gamma = 2$ or a single-temperature `apec` model with a plasma temperature between 10 and 20 keV. The broadband (3–40 keV) energy quantiles of the *NuSTAR* sources show that the majority of sources have photon indices of $\Gamma = 2$–3 for a power-law model or $kT = 5$–30 keV for a bremsstrahlung model, which are consistent with the spectral parameters required for good agreement between the 10–20 keV and 2–10 keV log$N$–log$S$ distributions.

4. We fit the joint *Chandra* and *NuSTAR* spectra of all sources with >100 counts in the 3–40 keV band but find that >300 *NuSTAR* counts are required to provide meaningful constraints on the spectral model parameters. We find good agreement between the spectral parameters from our fits and the location of the sources in the quantile diagrams.

5. Four of the sources detected in the *NuSTAR* Norma arm region survey are previously well-studied sources: NNR 1 is the BH LMXB 4U 1630–472, NNR 2 is the supergiant HMXB IGR J16393–4643, NNR 3 is the PWN and luminous TeV source HESS J1640–465, and NNR 24 is the magnetar SGR J1627–41. Based on the X-ray variability, spectral fits, and infrared counterpart information for each source, we determine the most likely nature of the fainter sources in our survey, which are summarized in Table 11. NNR 5, 8, and 21 are PWN candidates, NNR 7 and 14 are likely CWBs, NNR 10 is a possible magnetar, and NNR 15 is a quiescent BH LMXB candidate. The other sources are primarily CV candidates, a mixture of IPs, polars, nonmagnetic CVs, and SBs. We estimate that five background AGNs are present among the tier 1 *NuSTAR* sources.

6. Compared to the *NuSTAR* sources that are detected in the GC region, the sources in the Norma region have softer spectra on average. Even if we restrict the comparison to the CV candidates in these two regions, the Norma CVs exhibit lower plasma temperatures than those in the GC. The $kT \approx 15$ keV temperatures of the Norma CV candidates resemble the hot component of the GRXE spectrum.

7. If most of the Norma CV candidates are IPs, then their plasma temperatures indicate that the WDs in these systems have masses of $\approx 0.6\,M_\odot$, which are lower than the WD masses of $\gtrsim 0.8\,M_\odot$ estimated for the GC IPs. However, we argue that it is more likely that the fraction of IPs relative to polars, nonmagnetic CVs, and SBs is lower among the Norma CV candidates than in the GC region. Since IPs have the hardest X-ray spectra of all of these types of sources, a lower fraction of IPs in the Norma region would result in lower plasma temperatures for the average source.

8. In order to understand the nature of the hard X-ray sources in the Norma region and why they differ from the hard X-ray sources in the GC region, it is necessary to continue monitoring the X-ray variability of the Norma CV candidates, better characterize the variability and spectral types of their infrared counterparts, and obtain higher quality spectra, especially at Fe line energies, for the brighter sources. Follow-up multiwavelength observations of the candidate PWNs, CWBs, and quiescent BH binary would be useful in furthering our understanding of compact stellar remnants and the evolution of massive stars.
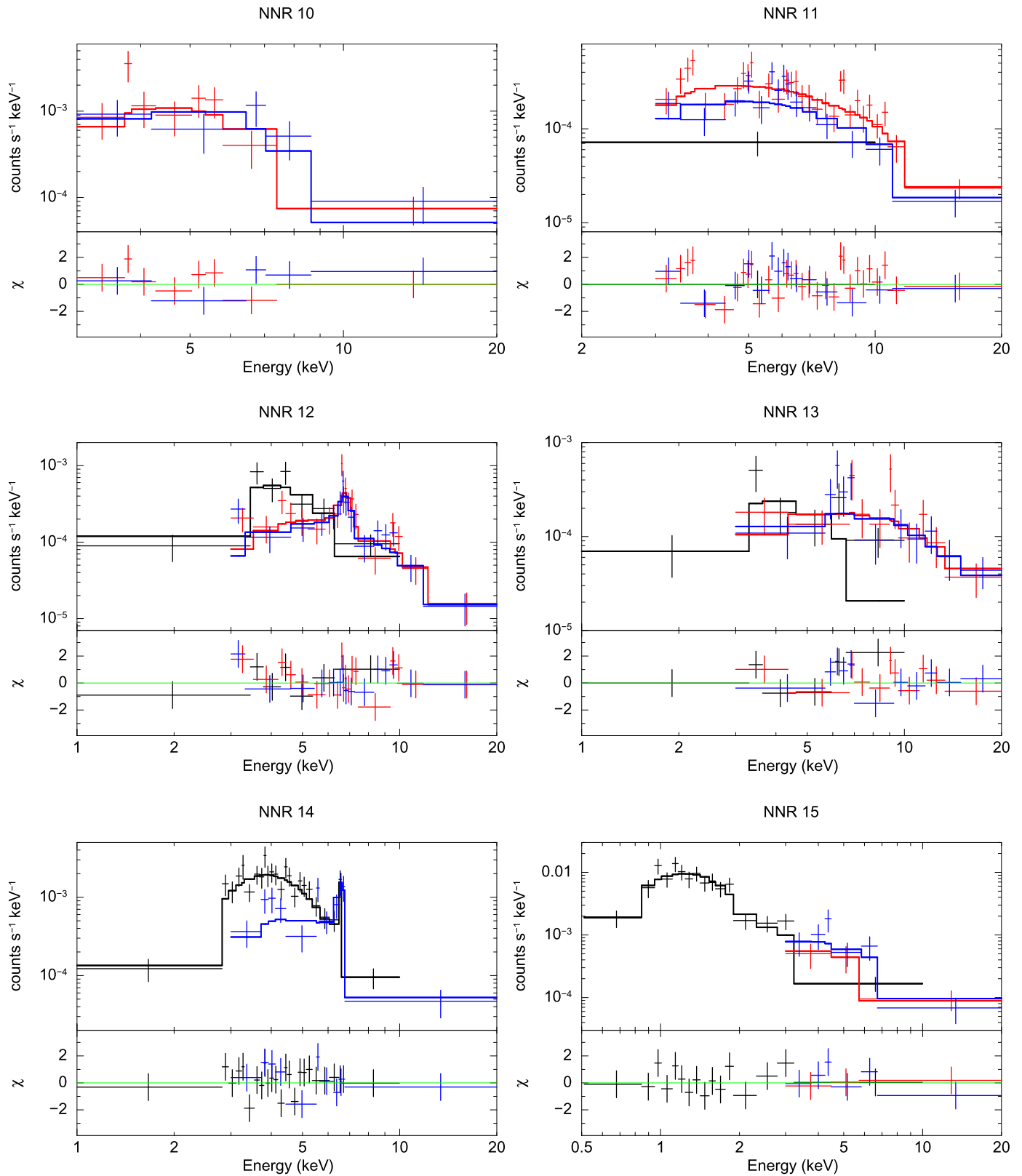
Figure 12. *Chandra* and *NuSTAR* spectra with residuals of the best-fitting models for sources NNR 10–27. See the Appendix for more details.

Figure 12. (Continued.)

36

Figure 12. (Continued.)

Appendix

In this appendix, we present the *Chandra* and *NuSTAR* spectra of sources NNR 10–27 and residuals for the best-fitting spectral models listed in Table 9. Our spectral analysis is

described in Section 5.7. The spectra of NNR 1, 2, and 3 are shown in King et al. (2014), B16, and G14, respectively, while the spectra of sources NNR 4–9 are shown in Figure 8. In Figure 12, *Chandra* data is shown in black, *NuSTAR* FPMA data is shown in red, and FPMB data is shown in blue. For NNR 19, black points show the *Chandra* spectrum from ObsID 7591, while orange points show the *Chandra* spectrum from ObsID 16170. For NNR 21, black points denote the *Chandra* spectrum for the point source and extended emission combined, while orange points display the point source contribution alone.

References

An, H., Kaspi, V. M., Tomsick, J. A., et al. 2012, ApJ, 757, 68
Archibald, R. F., Gotthelf, E. V., Ferdman, R. D., et al. 2016, ApJL, 819, L16
Arnaud, K. A. 1996, in ASP Conf. Ser. 101, Astronomical Data Analysis Software and Systems V, ed. G. H. Jacoby & J. Barnes (San Francisco, CA: ASP), 17
Barlow, E. J., Knigge, C., Bird, A. J., et al. 2006, MNRAS, 372, 224
Barret, D., McClintock, J. E., & Grindlay, J. E. 1996, ApJ, 473, 963
Baskill, D. S., Wheatley, P. J., & Osborne, J. P. 2005, MNRAS, 357, 626
Berghoefer, T. W., Schmitt, J. H. M. M., Danner, R., & Cassinelli, J. P. 1997, A&A, 322, 167
Bernardini, F., de Martino, D., Falanga, M., et al. 2012, A&A, 542, A22
Bhalerao, V. 2012, PhD thesis, Caltech
Bocchino, F., & Bykov, A. M. 2001, A&A, 376, 248
Bodaghee, A., Tomsick, J. A., Fornasini, F. M., et al. 2016, ApJ, 823, 146
Bodaghee, A., Tomsick, J. A., Krivonos, R., et al. 2014, ApJ, 791, 68
Bodaghee, A., Tomsick, J. A., Rodriguez, J., & James, J. B. 2012, ApJ, 744, 108
Bodaghee, A., Walter, R., Zurita Heras, J. A., et al. 2006, A&A, 447, 1027
Brogan, C. L., Frail, D. A., Goss, W. M., & Troland, T. H. 2000, ApJ, 537, 875
Bronfman, L., Alvarez, H., Cohen, R. S., & Thaddeus, P. 1989, ApJS, 71, 481
Buccheri, R., Bennett, K., Bignami, G. F., et al. 1983, A&A, 128, 245
Cappelluti, N., Brusa, M., Hasinger, G., et al. 2009, A&A, 497, 635
Casares, J., Charles, P. A., & Naylor, T. 1992, Natur, 355, 614
Cash, W. 1979, ApJ, 228, 939
Choi, C.-S., Dotani, T., & Agrawal, P. C. 1999, ApJ, 525, 399
Civano, F., Hickox, R. C., Puccetti, S., et al. 2015, ApJ, 808, 185
Combi, J. A., Albacete Colombo, J. F., Romero, G. E., & Benaglia, P. 2006, ApJL, 653, L41
Corbet, R. H. D., Sokoloski, J. L., Mukai, K., Markwardt, C. B., & Tueller, J. 2008, ApJ, 675, 1424
Corcoran, M. F. 1996, RMxAC, 5, 54
Corcoran, M. F. 2005, AJ, 129, 2018
Cutri, R. M., Wright, E. L., Conrow, T., et al. 2013, yCat, 2328
Dame, T. M., Hartmann, D., & Thaddeus, P. 2001, ApJ, 547, 792
Davies, B., de La Fuente, D., Najarro, F., et al. 2012, MNRAS, 419, 1860
de Martino, D., Matt, G., Belloni, T., et al. 2004, NuPhS, 132, 693
Dempsey, R. C., Linsky, J. L., Fleming, T. A., & Schmitt, J. H. M. M. 1993, ApJS, 86, 599
Dieters, S. W., Belloni, T., Kuulkers, E., et al. 2000, ApJ, 538, 307
Elshamouty, K., Heinke, C., & Chouinard, R. 2016, MNRAS, 463, 78
Eracleous, M., Halpern, J., & Patterson, J. 1991, ApJ, 382, 290
Esposito, P., Israel, G. L., Zane, S., et al. 2008, MNRAS, 390, L34
Esposito, P., Tiengo, A., Mereghetti, S., et al. 2009, ApJL, 690, L105
Ezuka, H., & Ishida, M. 1999, ApJS, 120, 277
Fornasini, F. M., Tomsick, J. A., Bodaghee, A., et al. 2014, ApJ, 796, 105
Franciosini, E., Pallavicini, R., & Tagliaferri, G. 2001, A&A, 375, 196
Freeman, P. E., Kashyap, V., Rosner, R., & Lamb, D. Q. 2002, ApJS, 138, 185
Gagné, M., Oksala, M. E., Cohen, D. H., et al. 2005, ApJ, 628, 986
Gehrels, N. 1986, ApJ, 303, 336
Georgakakis, A., Nandra, K., Laird, E. S., Aird, J., & Trichas, M. 2008, MNRAS, 388, 1205
Gotthelf, E. V. 2003, ApJ, 591, 361
Gotthelf, E. V., Tomsick, J. A., Halpern, J. P., et al. 2014, ApJ, 788, 155
Hailey, C. J., Mori, K., Perez, K., et al. 2016, ApJ, 826, 160
Hamaguchi, K., Corcoran, M. F., Gull, T., et al. 2007, ApJ, 663, 522
Harrison, F. A., Craig, W. W., Christensen, F. E., et al. 2013, ApJ, 770, 103
Hellier, C., Mukai, K., & Beardmore, A. P. 1997, MNRAS, 292, 397
Hirano, T., Hayakawa, S., Nagase, F., Masai, K., & Mitsuda, K. 1987, PASJ, 39, 619

Hong, J., Mori, K., Hailey, C. J., et al. 2016, ApJ, 825, 132
Hong, J., Schlegel, E. M., & Grindlay, J. E. 2004, ApJ, 614, 508
Hong, J., van den Berg, M., Schlegel, E. M., et al. 2005, ApJ, 635, 907
House, L. L. 1969, ApJS, 18, 21
Hurley, K., Kouveliotou, C., Woods, P., et al. 1999, ApJL, 519, L143
Iwasawa, K., Mainieri, V., Brusa, M., et al. 2012, A&A, 537, A86
Jakobsen, S. J. 2013, Master's thesis, Copenhagen Univ., Niels Bohr Institute
Jakobsen, S. J., Tomsick, J. A., Watson, D., Gotthelf, E. V., & Kaspi, V. M. 2014, ApJ, 787, 129
Jones, C., & Dickey, J. M. 2012, ApJ, 753, 62
Kalberla, P. M. W., Burton, W. B., Hartmann, D., et al. 2005, A&A, 440, 775
Kargaltsev, O., & Pavlov, G. G. 2008, in AIP Conf. Ser. 983, 40 Years of Pulsars: Millisecond Pulsars, Magnetars and More, ed. C. Bassa et al. (Melville, NY: AIP), 171
King, A. L., Walton, D. J., Miller, J. M., et al. 2014, ApJL, 784, L2
Klein-Wolt, M., Homan, J., & van der Klis, M. 2004, NuPhS, 132, 381
Koglin, J. E., An, H., Barrière, N., et al. 2011, Proc. SPIE, 8147, 81470J
Krivonos, R., Revnivtsev, M., Churazov, E., et al. 2007, A&A, 463, 957
Kuchar, T. A., & Clark, F. O. 1997, ApJ, 488, 224
Kuulkers, E., Parmar, A. N., Kitamoto, S., Cominsky, L. R., & Sood, R. K. 1997, MNRAS, 291, 81
Landi, R., Bassani, L., Dean, A. J., et al. 2009, MNRAS, 392, 630
Lansbury, G. B., Stern, D., Aird, J., et al. 2017, ApJ, 836, 99
Lemiere, A., Slane, P., Gaensler, B. M., & Murray, S. 2009, ApJ, 706, 1269
Luna, G. J. M., & Sokoloski, J. L. 2007, ApJ, 671, 741
Luna, G. J. M., Sokoloski, J. L., Mukai, K., & Nelson, T. 2013, A&A, 559, A6
Madsen, K. K., Harrison, F. A., Markwardt, C. B., et al. 2015, ApJS, 220, 8
Makino, F., Wagner, R. M., Starrfield, S., et al. 1989, IAUC, 4786
Markowitz, A., & Edelson, R. 2004, ApJ, 617, 939
Masetti, N., Dal Fiume, D., Cusumano, G., et al. 2002, A&A, 382, 104
Mateos, S., Alonso-Herrero, A., Carrera, F. J., et al. 2012, MNRAS, 426, 3271
Maughan, B. J., Giles, P. A., Randall, S. W., Jones, C., & Forman, W. R. 2012, MNRAS, 421, 1583
Mercer, E. P., Clemens, D. P., Meade, M. R., et al. 2005, ApJ, 635, 560
Mikles, V. J., Eikenberry, S. S., Muno, M. P., Bandyopadhyay, R. M., & Patel, S. 2006, ApJ, 651, 408
Minniti, D., Lucas, P. W., Emerson, J. P., et al. 2010, New Astronomy, 15, 433
Mori, K., Gotthelf, E. V., Dufour, F., et al. 2014, ApJ, 793, 88
Mori, K., Hailey, C. J., Krivonos, R., et al. 2015, ApJ, 814, 94
Morihana, K., Tsujimoto, M., Dubath, P., et al. 2016, PASJ, 68, 57
Mukai, K., & Shiokawa, K. 1993, ApJ, 418, 863
Muno, M. P., Arabadjis, J. S., Baganoff, F. K., et al. 2004, ApJ, 613, 1179
Muno, M. P., Bauer, F. E., Baganoff, F. K., et al. 2009, ApJS, 181, 110
Nagase, F. 1989, PASJ, 41, 1
Nespoli, E., Fabregat, J., & Mennickent, R. E. 2010, A&A, 516, A94
Orio, M., Covington, J., & Ögelman, H. 2001, A&A, 373, 542
Page, K. L., O'Brien, P. T., Reeves, J. N., & Turner, M. J. L. 2004, MNRAS, 347, 316
Pandey, J. C., & Singh, K. P. 2012, MNRAS, 419, 1219
Perez, K., Hailey, C. J., Bauer, F. E., et al. 2015, Natur, 520, 646
Petit, V., Owocki, S. P., Wade, G. A., et al. 2013, MNRAS, 429, 398
Pittard, J. M., Stevens, I. R., Corcoran, M. F., & Ishibashi, K. 1998, MNRAS, 299, L5
Portegies Zwart, S. F., Pooley, D., & Lewin, W. H. G. 2002, ApJ, 574, 762
Possenti, A., Cerutti, R., Colpi, M., & Mereghetti, S. 2002, A&A, 387, 993
Rahoui, F., Tomsick, J. A., Fornasini, F. M., Bodaghee, A., & Bauer, F. E. 2014, A&A, 568, A54
Ramsay, G., Cropper, M., Wu, K., et al. 2004, MNRAS, 350, 1373
Rana, V., Loh, A., Corbel, S., et al. 2016, ApJ, 821, 103
Revnivtsev, M., Molkov, S., & Sazonov, S. 2006a, MNRAS, 373, L11
Revnivtsev, M., Sazonov, S., Churazov, E., et al. 2009, Natur, 458, 1142
Revnivtsev, M., Sazonov, S., Gilfanov, M., Churazov, E., & Sunyaev, R. 2006b, A&A, 452, 169
Ricci, C., Ueda, Y., Paltani, S., et al. 2014, MNRAS, 441, 3622
Sana, H., Rauw, G., Nazé, Y., Gosset, E., & Vreux, J.-M. 2006, MNRAS, 372, 661
Sarma, A. P., Goss, W. M., Green, A. J., & Frail, D. A. 1997, ApJ, 483, 335
Sazonov, S., Krivonos, R., Revnivtsev, M., Churazov, E., & Sunyaev, R. 2008, A&A, 482, 517
Scaringi, S., Bird, A. J., Norton, A. J., et al. 2010, MNRAS, 401, 2207
Schulz, N. S., Canizares, C., Huenemoerder, D., & Tibbets, K. 2003, ApJ, 595, 365
Schulz, N. S., Canizares, C. R., Huenemoerder, D., & Lee, J. C. 2000, ApJL, 545, L135
Seifina, E., Titarchuk, L., & Shaposhnikov, N. 2014, ApJ, 789, 57

Shahbaz, T., Bandyopadhyay, R., Charles, P. A., & Naylor, T. 1996, MNRAS, 282, 977

Smith, R. K., Mushotzky, R., Mukai, K., et al. 2008, PASJ, 60, S43

Stern, D., Assef, R. J., Benford, D. J., et al. 2012, ApJ, 753, 30

Still, M., & Mukai, K. 2001, ApJL, 562, L71

Strassmeier, K. G., Hall, D. S., Fekel, F. C., & Scheck, M. 1993, A&AS, 100, 173

Szkody, P., Nishikida, K., Erb, D., et al. 2002, AJ, 123, 413

Tanaka, Y. 1996, in Röntgenstrahlung from the Universe, ed. H. U. Zimmermann, J. Trümper, & H. Yorke (Munich: MPE), 85

Tomsick, J. A., Gotthelf, E. V., Rahoui, F., et al. 2014, ApJ, 785, 4

Tomsick, J. A., & Kaaret, P. 2000, ApJ, 537, 448

Torrejón, J. M., Schulz, N. S., Nowak, M. A., & Kallman, T. R. 2010, ApJ, 715, 947

Townsley, L. K., Broos, P. S., Corcoran, M. F., et al. 2011, ApJS, 194, 1

Tozzi, P., Gilli, R., Mainieri, V., et al. 2006, A&A, 451, 457

Traulsen, I., Reinsch, K., Schwarz, R., et al. 2010, A&A, 516, A76

Türler, M., Chernyakova, M., Courvoisier, T. J.-L., et al. 2010, A&A, 512, A49

Vallée, J. P. 2008, ApJ, 681, 303

van der Klis, M. 1989, in NATO ASI Series C, Vol. 262, Timing Neutron Stars, ed. H. Ögelman & E. P. J. van den Heuvel (New York: Kluwer Academic/Plenum Publishers), 27

Verner, D. A., Ferland, G. J., Korista, K. T., & Yakovlev, D. G. 1996, ApJ, 465, 487

Viotti, R. F., Antonelli, L. A., Rossi, C., & Rebecchi, S. 2004, A&A, 420, 527

Weisskopf, M. C., Wu, K., Trimble, V., et al. 2007, ApJ, 657, 1026

Wik, D. R., Hornstrup, A., Molendi, S., et al. 2014, ApJ, 792, 48

Wilms, J., Allen, A., & McCray, R. 2000, ApJ, 542, 914

Wilson, T. L., Mezger, P. G., Gardner, F. F., & Milne, D. K. 1970, A&A, 6, 364

Woods, P. M., Kouveliotou, C., van Paradijs, J., et al. 1999, ApJL, 519, L139

Worpel, H., Schwope, A. D., Granzer, T., et al. 2016, A&A, 592, A114

Wright, E. L., Eisenhardt, P. R. M., Mainzer, A. K., et al. 2010, AJ, 140, 1868

Xu, X.-j., Wang, Q. D., & Li, X.-D. 2016, ApJ, 818, 136

Yuasa, T., Makishima, K., & Nakazawa, K. 2012, ApJ, 753, 129

Zhekov, S. A., & Skinner, S. L. 2000, ApJ, 538, 808

Zorotovic, M., Schreiber, M. R., & Gänsicke, B. T. 2011, A&A, 536, A42